# INFORMATION TO USERS

This manuscript has been reproduced from the microfilm master. UMI films the text directly from the original or copy submitted. Thus, some thesis and dissertation copies are in typewriter face, while others may be from any type of computer printer.

**The quality of this reproduction is dependent upon the quality of the copy submitted.** Broken or indistinct print, colored or poor quality illustrations and photographs, print bleedthrough, substandard margins, and improper alignment can adversely affect reproduction.

In the unlikely event that the author did not send UMI a complete manuscript and there are missing pages, these will be noted. Also, if unauthorized copyright material had to be removed, a note will indicate the deletion.

Oversize materials (e.g., maps, drawings, charts) are reproduced by sectioning the original, beginning at the upper left-hand corner and continuing from left to right in equal sections with small overlaps. Each original is also photographed in one exposure and is included in reduced form at the back of the book.

Photographs included in the original manuscript have been reproduced xerographically in this copy. Higher quality 6" x 9" black and white photographic prints are available for any photographs or illustrations appearing in this copy for an additional charge. Contact UMI directly to order.

**UMI**

A Bell & Howell Information Company
300 North Zeeb Road, Ann Arbor MI 48106-1346 USA
313/761-4700 800/521-0600

# Curvature and Acoustic Instabilities in Rotating Fluid Disks

by

Montenegro ED
Luis Enrique Montenegro ED

A dissertation submitted to the Graduate Faculty in Physics in partial fulfillment of the requirements for the degree of Doctor of Philosophy, The City University of New York

1998

This manuscript has been read and accepted for the Graduate Faculty in Physics in satisfaction of the dissertation requirement for the degree of Doctor of Philosophy.

August 13, 1998 — Chi Yuan

Date — Chair of Examining Committee

Prof. Chi Yuan

9/18/98 — [signature]

Date — Executive Officer

Professor Timothy Boyer

Dr. Bruce G. Elmegreen

Prof. Jacqueline van Gorkom

THE CITY UNIVERSITY OF NEW YORK

Abstract

# CURVATURE AND ACOUSTIC INSTABILITIES IN ROTATING FLUID DISKS

by

Luis Enrique Montenegro

Adviser: Professor Chi Yuan

The stability of a rotating fluid disk to the formation of spiral arms is studied in an improved version of the tightwinding approximation in the linear regime. Commonly ignored terms such as the radial variation of basic disk properties and multiple spiral arms change significantly the stability of the disk especially at small galactrocentric radii, and are included in this study. Two dimensionless parameters are found to be important: the ratio of disk mass to total mass (disk + halo), and the ratio of epicyclic radius to disk radius. Disks that may be stable to axisymmetric perturbations are generally unstable to spirals. For such disks, perturbations grow at a rate proportional to a linear combination of these two parameters. Three types of new instabilities are identified: *gravitational-curvature* instabilities, *acoustic-curvature* instabilities, and *acoustic* instabilities. The acoustic instabilities arise from the asymmetric nature of the spirals and from the differential rotation present in the disk.

Unstable growth rates are determined for these instabilities in several representative cases with varying types of differential rotation and self-gravity. The most important applications appear to be as a source of spiral structure in

non-self-gravitating disks with short orbital times.

Observations with the Hubble Space Telescope reveal an irregular network of dust spiral arms in the nuclear region of the interacting disk galaxy NGC 2207. Properties of the gas imply that none of the usual spiral-generating mechanisms are present. Instead, the spirals may result from acoustic instabilities that amplify at small galactic radii.

Multiple armed stellar spirals are evident in computer enhanced images of disk spiral galaxies. The images reveal clear superpositions of simple two- and three-arm structures. The radial extents of both spiral structures are consistent with the modal theory that most two-arm spirals are self-sustaining wave modes, the three-arm spirals are driven by asymmetries in the two-arm wave modes, and are a likely source of energy loss from the two-arm mode. The three arm spirals may take several revolutions to build up once an asymmetric two arm spiral appears, thus the morphology of the galaxy will slowly change with time.

## Acknowledgments

It is a pleasure to acknowledge my appreciation to the following people: Prof. Chi Yuan, for his valuable guidance and patience as my thesis advisor; Dr. Bruce Elmegreen for his valuable guidance and enthusiastic support through my long effort; Prof. Timothy Boyer and Prof. Jacqueline van Gorkom for their participation in the thesis defense committee; the Physics department at the City College, the Graduate Center/CUNY, and T. J. Watson Research Center, International Business Machines for their financial support of my education and research and for the use of their computing facilities; finally I am grateful to my parents, wife and several close relatives and friends for their support and encouragement.

## Dedication

To my parents, and to my wife, Artemisa Pichardo.

# Synopsis

This thesis consists of three parts. Each part is a report on investigations undertaken by the author and various collaborators on properties of spiral waves in galactic and other fluid disks. The following descriptions of the reports are in logical order.

Part I is a report of a study of the conditions of stability of waves propagating in galactic or other fluid disks. Terms that are usually ignored in previous studies are included here. From Parts II and III we understand that multiple arms can be present in the disk (m > 2) so the analysis allows for multiple arms. Other effects of the same order as that of multiple arms are included as well for completeness. These effects arise from radial gradients of the basic properties of the disk and curvature terms from the cylindrical geometry. Instabilities of arising from self-gravity are explicitly presented through a parameter $\epsilon = 2\pi G\sigma_0/(\kappa^2 r)$ where $\sigma_0$ is the surface density, $\kappa$ is the epicyclic frequency, and $r$ is the radius. The parameter $\epsilon$ is proportional to the ratio of the disk mass to the total mass (disk and halo). Acoustic instabilities are present through a combination of terms $(a/\kappa r)$, where $a$ is the sound speed. When self-gravity is turned off, acoustic instabilities remain.

Part II is a report of dust spiral arms discovered in the nuclear region of the interacting disk galaxy NGC2207. Radiative transfer calculations determine that the disk is not self-gravitating so the usual mechanisms of gravitational instability

cannot explain the presence of the spirals. It is suggested that acoustic instabilities are present. These instabilities grow with a characteristic time roughly equal to the orbital time so are more easily observed in regions where the disk is rapidly rotating.

Part III is a report of symmetries discovered in spiral patterns in galactic disks. A method is devised to extract m-fold (m=2,3,...) symmetric images from deprojected sky images of a sample of 18 spiral galaxies. A large fraction of galaxies that have two main galactic arms also have three-arm structures. The radial extent of the m-arm structure fits between the inner and the outer m:1 resonance radii if a single value of the pattern speed is assumed for the different m-armed spirals. The two-arm spirals are interpreted to be self-sustaining wave modes reflecting from bars inside corotation or evanescent regions where the non-barred spirals wind into a circle. Three-arm spirals are interpreted to be driven waves by m=1 asymmetries in the m=2 spiral waves; with time the higher m waves extract energy from the m=2 spiral wave mode and may serve as an indicator of time elapsed since tidal events triggered the m=2 wave modes.

# Contents

# List of Tables

# List of Figures

# Chapter 1

# Introduction

Spiral galaxies are characterized by bright 'arms' spiraling out from a region near the center. Differential rotation will shear and wind these arms quickly if they are material features, so Lindblad (1958) and Lin & Shu (1964) developed a theory of density waves with a pattern that rotated in a fixed manner to overcome this winding dilemma (Quasi-Stationary Spiral Structure or QSSS hypothesis). Where the angular speed of the pattern, $\Omega_p$, is commensurate with the natural frequencies of the disk (angular frequency $\Omega$ and radial frequency $\kappa$) resonance occurs. The most important resonances are the corotation resonance where $\Omega_p = \Omega$, the Outer Lindblad resonance (OLB), where $\Omega_p = \Omega + \kappa/2$, and the Inner Lindblad Resonance (ILB), where $\Omega_p = \Omega - \kappa/2$. Lin (1966) and Lin & Shu (1964,1966) considered tightly wrapped waves in infinitely thin stellar disks so that the azimuthal variations of some quantities could be ignored (called the tight-winding approximation). They also obtained (Lin 1966; Lin, Yuan & Shu 1969) the dispersion relation for these waves away from resonances, which is the relation between frequency and wavenumber. The effect of finite thickness was studied by Lin & Shu (1968) and

Vandervoort (1970). An important discriminant in this dispersion relation is the stability parameter $Q$ for axisymmetric disturbances (Toomre 1964); when $Q > 1$, the disk is stable against ring-like disturbances.

Toomre (1969) showed that the density waves propagate radially in a few $10^8$ years and Mark (1971, 1974b) showed that the waves are absorbed at the inner Lindblad resonance. For spiral structure to survive, a source of waves is needed to replenish the waves absorbed at the resonances. Different mechanisms have been considered. Some mechanisms that have been proposed are external forcing by companions (Toomre 1969, 1974, 1981; Toomre & Toomre 1972; Athanassoula 1978a, 1978b; Goldreich & Tremaine 1978, 1979), bars (Lindblad 1960; Feldman & Lin 1973; Lin & Lau 1975; Goldreich & Tremaine 1979; Athanassoula 1980; Prendergast 1983; Yuan 1984; Yuan & Cheng 1991; Yuan & Kuo 1997), asymmetries (Athanassoula 1984; Kato & Tosa 1994), and feedback mechanisms discussed below. The transport of angular momentum was recognized as the central role played by spiral waves (Lynden-Bell & Kalnajs 1972; Goldreich & Tremaine 1979).

Lau & Bertin (1978) included additional terms in the QSSS analysis that treated tangential forces for fluid spiral waves in a uniform disk, finding an additional destabilizing term they called $J$. This term describes the rate of shear that the disk experiences. They ignored curvature terms, which scale inversely with galactocentric radius. Other researchers (Goldreich & Lynden-Bell 1965; Zang 1976; Julian & Toomre 1966; Toomre 1981) also studied azimuthal forces, by considering the temporal response of shearing wavelets. Toomre (1981) termed the mechanism responsible for the spectacular growth of shearing waves a "swing amplifier". He found that spiral waves can grow for a short time even when $Q > 1$, as long as $Q$ is not too large. Thus a theory that constantly forming and decaying shearing

disturbances provide the observed spiral structure in galactic disks was put forward.

A mechanism for feedback cycles in the maintainance of waves has been proposed in the context of the QSSS hypothesis. The WASER (Wave Amplification via Stimulated Emission of Radiation) was proposed by Mark (1974a, 1976a, 1976b, 1976c, 1977). In this mechanism three waves interact at the corotation region: an outgoing long trailing wave stimulates the emission of two short trailing waves; one propagates outward and is dissipated at the OLR while the other propagates inward and is reflected near the center (again outside the ILB) as a long trailing wave which then repeats the cycle at corotation. This process is now called WASER I to distinguish it from a version developed later using a different set of wave interactions through the swing amplifier. In the WASER II mechanism, a leading wave propagates outward to corotation while it unwinds. As it turns from leading to trailing it is heavily amplified and two trailing waves are formed, one travels inward from corotation, and the other travels outward where it dissipates at the OLB. The inward propagating wave then is reflected near the center (outside the ILB) as an outgoing leading wave which travels to corotation to complete the cycle.

It has long been recognized that gas in galactic disks contributes to the growth of waves in the stellar component (Lin & Shu 1966; Jog & Solomon 1984a, b). On the other hand, cold gas can be shocked, dissipate energy, and damp the excitation of spiral waves (Roberts 1969; Roberts & Shu 1972). Thus the presence of gas regulates the spiral instabilities in the disk. Bertin, Lin and collaborators have developed a linear theory of global spiral modes in fluid systems (Lin, Yuan & Shu 1969; Bertin & Romeo 1988; Bertin et al. 1989a, b) that includes the role of gas and relaxes the restriction of tightly wound waves. In this theory there are several standing wave modes that contribute to the spiral structure.

Here we derive several new dispersion relations for gaseous disks in the QSSS hypothesis in a modified version of the tight-winding approximation considering the curvature terms and other terms that were ignored in these previous studies. We also include radial variations of the basic properties of the disk (such as surface density $\sigma_0$, sound speed $a$, wavenumber $k$, etc). Our additional terms depend on two dimensionless parameters,

$$\epsilon \equiv 2\pi G\sigma_0/\tau\kappa^2 \tag{1.1}$$

and $a/(\kappa r)$, for radius $r$ and epicyclic frequency $\kappa$. Typically $\epsilon \sim 0.1$, which is small, so our new results are not important modifications to previous studies that considered only small $Q$. In regions where $Q$ is large, the additional terms lead to residual instabilities that can be very important in some situations.

Numerical and analytical solutions to the modified dispersion relations are found here for typical regions in galactic and other disks. These include the main disks of spiral galaxies, where the rotation curves are approximately flat (Rubin et al. 1985); the inner disks of galaxies, where the rotation curves are approximately solid body; inner solid-body gaseous disks that are not self-gravitating (e.g., NGC 2207; Elmegreen et al. 1998), and non-self-gravitating Keplerian disks, as might be appropriate for proto-planetary disks or galactic nuclear regions surrounding black holes (Nakai et al. 1993). It is found that for solid body rotation the dispersion relation is a cubic polynomial in the dimensionless frequency $\nu = (\omega - m\Omega)/\kappa$, for wave frequency $\omega$. For disks with flat and Keplerian rotation curves, the dispersion relation is a fifth order polynomial in $\nu$.

## REFERENCES

Athanassoula, E. 1978a, in: Structure and Properties of Nearby Galaxies, eds. Berkhuijsen, E. M. & Wielebinski, R. (Reidel Pub.), 163

Athanassoula, E. 1978b, AA 69, 395

Athanassoula, E. 1980, AA, 88, 184

Athanassoula, E. 1984, Physics Reports, 114, Nos. 5 & 6, 319

Bertin, G. & Romeo, A. B., 1988, A. A., 195, 105

Bertin, G., Lin, C.C., Lowe, S.A. & Thurstan, R.P. 1989, ApJ, 33 8, 78

Bertin, G., Lin, C.C., Lowe, S.A. & Thurstan, R.P. 1989, ApJ, 33 8, 104

Elmegreen, B.G., Elmegreen, D.M., Brinks, E., Yuan, C., Kaufman, M., Klarić, M., Montenegro, L., Struck, C. & Thomasson, M. 1998, ApJL, in press

Goldreich, P. & Lynden-Bell, D. 1965, MNRAS, 130, 125

Goldreich, P. & Tremaine, S. 1978, Icarus, 34, 240.

Goldreich, P. & Tremaine, S. 1979,ApJ, 233. 857.

Julian, W. H., Toomre, A. 1966, ApJ, 14€

Lau, Y. Y. & Bertin, G. 1978, ApJ, 226, 508

Lin. C. C. 1966, *SIAM J Appl.. Math.*, 14, 876

Lin, C. C. & Shu, F. H. 1964, ApJ, 140, 646

Lin, C.C. & Shu, F. H. 1966, Proc. Nat. Acad. Sci., 55, 229

Lin, C.C. & Shu, F. H. 1971, in: Astrophysics and General Relativity, Vol. 2, eds. Chretien, M., Derer. S., and Goldstein, J. (Gordon and Breach Science Pub.) 239.

Lin, C. C., Yuan, C. & Shu, F. H. 1969, ApJ, 155, 721

Lindblad, B. 1958. Stock. Obs. Ann., 20, No. 6

Lynden-Bell, D. & Kalnajs, A. J. 1972, MNRAS, 157,1

Mark, J. W-K. 1971, Proc. Natl. Acad. Sc. USA, 68, 2095

Mark, J. W-K. 1974, in: The Formation and Dynamics of Galaxies, ed. Shakeshaft, J. (Reidel Pub.), 417

Mark, J. W-K. 1974, ApJ, 193, 539

Mark, J. W-K. 1976, ApJ, 203, 81

Mark, J. W-K. 1976, ApJ, 205, 363

Mark, J. W-K. 1976, ApJ, 206, 418

Mark, J. W-K. 1977, ApJ, 212, 645

Nakai, N., Inoue, M. & Miyoshi, M. 1993, Nature, 361, 45

Prendergast, K. H. 1983, in: Internal Kinematics and Dynamics of Galaxies, ed. Athanassoula, E. (Reidel Pub.), 215

Roberts, W.W. 1969, ApJ, 158, 123

Roberts, W.W., Shu, F. 1972, ApJ, 12, 49

Rubin, V.C., Burstein, D., Ford, W.K. & Thonnard, A. 1985, ApJ, 289, 81

Toomre A. 1964, ApJ, 139, 1217

Toomre, A. 1969, ApJ, 158, 899

Toomre, A. 1981, in The Structure and Evolution of Normal Galaxies, Cambridge: Cambridge Univ. Press, 111

Toomre, A. & Toomre J. 1972, ApJ, 178, 623

Vandervoort, P. O. 1970, ApJ, 161, 67

Yuan, C. 1984, ApJ, 281, 600

Yuan, C. & Cheng, Y. 1991, ApJ, 376, 104

Yuan, C. & Kuo, C-L. 1997, ApJ, 484, 750

Zang, T.A., 1976, Ph.D. thesis, M.I.T.

---

This manuscript was prepared with the AAS LaTeX macros v4.0.

# Chapter 2

# Curvature and Acoustic Instabilities in Rotating Fluid Disks

# Curvature and Acoustic Instabilities in Rotating Fluid Disks

L.E. Montenegro

Department of Physics, City College of New York, New York NY 10031

C. Yuan

Institute of Astronomy & Astrophysics, Academia Sinica,

P.O. Box 1-87, Nanking, Taipei, Taiwan 115, ROC

and

B.G. Elmegreen

IBM Research Division, T. J. Watson Research Center,

P.O. Box 218, Yorktown Heights, NY 10598

Received _____; accepted _____

## ABSTRACT

The stability of a rotating fluid disk to the formation of spiral arms is studied in the tightwinding approximation in the linear regime. Terms that are commonly ignored are taken into account through an algebraic reformulation, including the radial dependence of basic parameters and terms of order $1/kr$, for wavenumber $k$ and radius $r$. These terms change significantly the stability of the disk. We identify two important dimensionless physical parameters: $\epsilon = 2\pi G\sigma_0/(r\kappa^2)$, which is essentially the ratio of disk mass to total mass (disk and halo), and $a/(\kappa r)$, which is the ratio of epicyclic radius to disk radius ($\sigma_0$ is the mass column density, $\kappa$ is the epicyclic frequency, and $a$ is the sound speed). The small term $\zeta = (k^2r^2 + m^2)^{-1/2}$ is an additional parameter that is purely geometrical for number of arms $m$. In general, a disk is unstable for large values of Toomre's parameter $Q$, which was previously thought to be a stable regime. Density waves at high $Q$ grow at a rate that is roughly proportional to a linear combination of terms that depend on $\epsilon$ and $a/(\kappa r)$. Instabilities that arise from $\epsilon$ are termed *gravitational-curvature* instabilities. Instabilities that arise from $a/(\kappa r)$ are termed *acoustic-curvature* instabilities. Another term, $J$, that depends on differential rotation and has been previously considered in the self- gravitating case by Bertin, Lin, and others, is given a new interpretation in the case of negligible self-gravity. It is found that a new combination of parameters, $J/(m\epsilon)$, depends only on the amount of shear, and gives rise to a third new instability which is termed an *acoustic* instability.

Unstable growth rates are determined for these instabilities in four

cases: a self-gravitating disk with a flat rotation curve, a self-gravitating disk with solid body rotation, a non-self-gravitating disk with solid body rotation, and a non-self-gravitating disk with Keplerian rotation. The most important applications appear to be as a source of spiral structure, possibly leading to accretion in non-self-gravitating disks, such as some galactic nuclear disks, disks around black holes, and proto-planetary disks. All of these examples have short orbital times so the unstable growth time can be small, even when only terms of order $\epsilon$ contribute.

## 1. Introduction

Spiral galaxies are characterized by bright "arms" spiraling out from a region near the center. Differential rotation will shear and wind these arms quickly if they are material features, so Lindblad (1958) and Lin & Shu (1964) developed a theory of density waves to overcome this winding dilemma. Lin & Shu (1964,1966) also obtained the dispersion relation for these waves, which is the relation between frequency and wavenumber. An important discriminant in this dispersion relation is the stability parameter $Q$ for axisymmetric disturbances (Toomre 1964); when $Q > 1$, the disk is stable against ring-like disturbances.

Lau & Bertin (1978) included additional terms that treated tangential forces for gaseous spiral waves in a uniform disk, finding an additional destabilizing term they called $J$. They used a WKB approximation and ignored curvature terms, which scale inversely with galactocentric radius. Goldreich & Lynden-Bell (1965), Zang (1976), and Toomre (1981) also studied azimuthal forces, by considering the temporal response of shearing wavelets. Toomre (1981) termed the mechanism responsible for the spectacular growth of shearing waves a "swing amplifier". He found that spiral

waves can grow for a short time even when $Q > 1$, as long as $Q$ is not too large.

Here we derive several new dispersion relations for gaseous disks considering the curvature terms and other terms that were ignored in these previous studies. We also include radial variations of the basic properties of the disk. Our additional terms depend on two dimensionless parameters,

$$\epsilon \equiv 2\pi G\sigma_0/r\kappa^2, \tag{2.1}$$

and $a/(\kappa r)$, for mass column density $\sigma_0$, radius $r$, epicyclic frequency $\kappa$, and sound speed $a$. Typically $\epsilon \sim 0.1$, which is small, so our new results are not important modifications to previous studies that considered only small $Q$. In regions where $Q$ is large, the additional terms lead to residual instabilities that can be very important in some situations.

Numerical and analytical solutions to the modified dispersion relation are found here for typical regions in galactic and other disks. These include the main disks of spiral galaxies, where the rotation curves are approximately flat (Rubin et al. 1985); the inner disks of galaxies, where the rotation curves are approximately solid body; inner solid-body gaseous disks that are not self-gravitating (e.g., NGC 2207; Elmegreen et al. 1998), and non-self-gravitating Keplerian disks, as might be appropriate for proto-planetary disks or galactic nuclear regions surrounding black holes (Nakai et al. 1993).

## 2. The Dispersion Relation

The dynamical response of an infinitely thin fluid disk to perturbation density waves will be studied here, considering various degrees of approximations using algebraic expansions in terms of small parameters. The disk response to spiral

waves is considered to be weak enough for the linearized equations of motion to be valid. The effects of self-gravity, pressure, and differential rotation are included. The pressure is assumed to depend only on the density; in the formulation, enthalpy is used. In the analysis, perturbation variables are assumed to be of the form $g_1(r,\theta,t) = G(r)e^{i\int k(r)dr}e^{i(\omega t - m\theta)}$, where $r$ is the radius, $\theta$ is the azimuthal angle, $\omega$ is the frequency of oscillation if it is real, and the growth or decay rate if it is imaginary, $m$ is the number of arms, $k(r)$ is the radial wavenumber, and $G(r)$ is the slowly varying amplitude. The spiral waves have an interarm spacing that is much shorter than the radius, that is $\zeta \equiv 1/|\hat{k}r| \ll 1$ for total wavenumber $\hat{k} = \sqrt{k^2 + m^2/r^2}$. This condition is satisfied either for very short waves or for open spirals with many arms, and it allows asymptotic solutions to the density response. The same condition is used to express the density as a linear function of the gravitational potential (Bertin & Mark 1979).

The linearized equations of motion are combined with the continuity equation to relate the perturbation enthalpy $h_1$ to the perturbation gravitational potential $\phi_1$ (Goldreich & Tremaine 1979, Lin & Lau 1979):

$$\mathcal{L}(h_1 + \phi_1) = -Ch_1, \tag{2.2}$$

where $\mathcal{L} = d^2/dr^2 + A\, d/dr + B$ and the coefficients are $A = -(1/r)\, d\ln \mathcal{A}/d\ln r$ , $B = -m^2/r^2 + (2m\Omega/r^2\kappa\nu)\, d\ln(\kappa^2(1-\nu^2)/\sigma_0\Omega)/d\ln r$, and $C = -\kappa^2(1-\nu^2)/a^2$; also $\mathcal{A} = \kappa^2(1-\nu^2)/(\sigma_0 r)$, where $\nu$ is the dimensionless frequency, $\nu = (\omega - m\Omega)/\kappa$, $m$ is the number of arms in the spiral pattern, $\kappa$ is the epicyclic frequency, $\sigma_0$ is the surface density of the disk, $\Omega(r)$ is the angular frequency, and $a$ is the sound speed in the disk. The perturbation gravitational potential can be expressed in the form $\phi_1(r) = \Phi(r)e^{i\int k(r)dr}$; then Poisson's equation is (Bertin & Mark 1979):

$$\sigma_1 = -\frac{\sigma_0}{a^2} f(r)\, \phi_1, \tag{2.3}$$

with the definition

$$f(r) \equiv \frac{1}{2\pi G r K(\alpha,m)} \left[1 + i\hat{A}(\alpha)\, r\, \frac{d\alpha}{dr} + \hat{B}(\alpha) r^2 \frac{d^2\alpha}{dr^2} + \hat{C}(\alpha)(r\frac{d\alpha}{dr})^2\right], \qquad (2.4)$$

and the approximation

$$\begin{aligned} K(\alpha,m) &= \tau(1 + \frac{m+1/2}{2}\tau^2), \\ \tau &= (\alpha^2 + (m+1/2)^2)^{-1/2}, \\ \alpha &= kr - ir\Phi'/\Phi - i/2. \end{aligned}$$

This expansion for $f(r)$ is correct to third order in $\alpha$. The terms $\hat{A}$, $\hat{B}$, and $\hat{C}$ are defined in Bertin & Mark (1979); they are:

$$\begin{aligned} \hat{A}(\alpha) &= K_2 - {K_1}^2 \\ \hat{B}(\alpha) &= {K_1}^3 + K_3 - 2K_1K_2 \\ \hat{C}(\alpha) &= 9{K_1}^2K_2 - 6K_1K_3 + 3K_4 - 3{K_1}^4 - 3{K_2}^2, \end{aligned}$$

where

$$K_n = \frac{1}{n!\, K(\alpha,m)} \frac{\partial^n K(\alpha,m)}{\partial \alpha^n}.$$

The enthalpy, $h_1 = a^2\sigma_1/\sigma_0$, can be expressed in terms of the potential $\phi_1$ using equation (3) to obtain

$$h_1 = -f(r)\,\phi_1. \qquad (2.5)$$

The expression for $f$, equation (4), can be expanded in the small parameter $\zeta$ to get $f(r) = (\hat{k}/k_J)[1 + i f_1 \zeta + f_2\zeta^2 + (f_3 + i f_4)\,\zeta^3 + ...]$. Here, $k_J \equiv 2\pi G\sigma_0/a^2$ is the two-dimensional equivalent of the Jeans wavenumber. The terms $f_i$ are real and depend on derivatives of $k$ and $\Phi$. For example,

$f_1 = (k/\hat{k})\left[-1/2 - r\,\Phi'/\Phi - \left(1 + r\,k'/k\right)\left(m^2/2\hat{k}^2\,r^2\right)\right]$. If only the first term is kept in the expansion of $f(r)$ and all radial gradients and the $m$-dependence of $\hat{k}$ is dropped, the Lin & Shu (1966) dispersion relation is obtained:

$$(\omega - m\Omega)^2 = \kappa^2 - 2\pi G\sigma_0|k| + k^2a^2. \tag{2.6}$$

In terms of the dimensionless frequency, $\nu = (\omega - m\Omega)/\kappa$, dimensionless wavelength, $\eta = k_{crit}/|k| \geq 0$, where $k_{crit} = \kappa^2/2\pi G\sigma_0$, and Toomre's stability parameter $Q = \kappa a/\pi G\sigma_0$, the Lin-Shu relation is

$$\nu^2 = 1 - \frac{1}{\eta} + \frac{Q^2}{4\eta^2}. \tag{2.7}$$

### 2.1. The stability parameter $J$ for tangential forces

In the derivation of the Lin-Shu dispersion relation, which is equation (7) above, terms of magnitude $m/kr$ are ignored. Thus the dispersion relation is accurate for radial oscillations only. When the azimuthal wavenumber $m/r$ is included, the gravitational instability is stronger (Lau & Bertin 1978). In the derivation of the corresponding dispersion relation, Lau and Bertin made the assumptions that in Poisson's equation the out of phase (i.e., imaginary) terms can be ignored and the wavenumber $|k| \sim k_J/2$. Defining the total wavelength to be $\lambda_m = 2\pi/\sqrt{k^2 + m^2/r^2}$, Poisson's equation becomes

$$-\phi_1 = G\sigma_1\lambda_m, \tag{2.8}$$

and equation (2) is

$$(\sigma_1/\sigma_0)_{in\ phase} = \frac{h_1 + \phi_1}{\kappa^2 - (\omega - m\Omega)^2}\left[-\frac{4\pi^2}{\lambda_m^2} - \frac{T_1}{(1-\nu^2)}\right], \tag{2.9}$$

where $T_1 = -(2m\Omega/\kappa r)^2(d\ln\Omega/d\ln r)$. Note that the last term in the equation above contains $(1 - \nu^2)$, which was not present in (C15) in Lau & Bertin (1978)

because they were considering solutions near corotation. However, $T_1/(1-\nu^2)$ can be derived from their equations (B6) and (B9), it comes from their second term in equation (B9). Lau & Bertin (1978) also dropped the fifth term in (C14) when they derived (C15) because it is higher order in $1/kr$. We do the same for equation (9) because this section is about the low order terms as well. We include all of these terms in the higher order analysis in the rest of the paper.

The dispersion relation is now

$$Q^2/4 = \hat{\eta} - \frac{(1-\nu^2)}{\hat{\eta}^{-2} + J^2/(1-\nu^2)}, \tag{2.10}$$

where $\hat{\eta} = k_{crit}/\hat{k}$ and $J^2 = T_1/k_{crit}^2$, as defined in Bertin et al. (1989). We call equation (10) the Bertin-Lin-Lowe-Thurstan (BLLT) dispersion relation with dimensionless frequency $\nu_{BLLT}$. It describes the response of a differentially rotating disk to spiral perturbations. Evidently, the response is stronger than for axisymmetric perturbations by a factor that depends on the parameter $J$.

Equation (10) was studied extensively by Lau & Bertin (1978) and Bertin et al. (1989) in the limit when $\nu \approx 0$. In this limit, equation (10) predicts an instability when the frequency is purely imaginary, and this occurs when

$$1 + \left(\frac{Q^2}{4\hat{\eta}^2} - \frac{1}{\hat{\eta}}\right)\left(1 + J^2\hat{\eta}^2\right) < 0. \tag{2.11}$$

For ring-like perturbations ($m = 0$ and $J = 0$), equation (11) is satisfied when $Q < 1$; that is, equation (11) reduces to Toomre's (1964) instability condition, $Q < 1$, for the axisymmetric case.

It is seen from equations (7) and (10) that when the imaginary terms in the equation of motion and Poisson's equation are ignored (Hunter 1983), the dimensionless frequency is pure real or pure imaginary according to the values of $\hat{\eta}$ and $Q$ and for small values of $J^2$. The exclusion of these imaginary terms is

justified in the limits $|kr| >> 1$ and $k_{crit}r >> 1$. This latter quantity is $\epsilon^{-1}$, defined by equation (1). If the complex terms are included in the equation of motion and Poisson's equation, then the frequency solutions are complex functions of $\hat{\eta}$ and $Q$. In that case, the frequency $\nu$ contains a non-vanishing imaginary part in all of the parameter space $(\eta, Q)$. This means there is always some instability present, so $Q$ is not an absolute discriminant of stability for small $J$ when higher order terms in $\epsilon$ are included.

### 2.2. Acoustic Instabilities in Non-Self Gravitating Disks

In addition to the instability condition given by equation (11), the BLLT dispersion relation (Eq. 10) predicts another instability when the frequency $\nu$ is complex and has a real component with an absolute value larger than 1. The condition for this second instability is:

$$\left(\frac{Q^2}{4\hat{\eta}^2} - \frac{1}{\hat{\eta}}\right)\left(\frac{Q^2}{4\hat{\eta}^2} - \frac{1}{\hat{\eta}} - 4J^2\hat{\eta}^2\right) < 0. \tag{2.12}$$

This condition can be written in the form

$$\frac{1}{\hat{\eta}} < \frac{Q^2}{4\hat{\eta}^2} < \frac{1}{\hat{\eta}} + 4J^2\hat{\eta}^2, \tag{2.13}$$

which is the same as

$$\epsilon\hat{k}r < \frac{a^2\hat{k}^2}{\kappa^2} < \epsilon\hat{k}r + \frac{4s^2m^2}{\hat{k}^2r^2} \tag{2.14}$$

if we substitute $Q\epsilon/2 = a/(\kappa r)$ and $\epsilon\hat{\eta} = 1/\hat{k}r$, and define $J^2/\epsilon^2 \equiv s^2m^2$, where $s = 2(-\Omega r\Omega')^{1/2}/\kappa$ and is of order 1. Equation (14) is *a new condition for instability.* When this condition is satisfied, the self-gravitating disk is unstable to the growth of spiral waves. The right hand side of equation (14) contains two terms. The first term depends on the self-gravity of the disk and the second depends on shear. When

gravity is negligible, there is still instability from the second term, coming entirely from pressure, shear, and Coriolis forces. We refer to this as an acoustic instability; it has apparently not been considered previously in the literature (spatial instability also exists when $\Omega' = 0$ or $m = 0$, see section 4).

Figure 1 shows the unstable regions for a five-arm spiral ($m = 5$) in the $(k_{crit}/|k|, Q^2)$ plane from the BLLT dispersion relation, equation (10), considering a self-gravitating disk with a flat rotation curve ($s^2 = 2$); this case is studied in more detail in the next section. The growth rate is represented as a gray scale, and the borders of the regions of instability are represented as lines, obtained from the instability conditions. The most unstable region is in the bottom left corner of the figure, where the bottom line shows the stability limit for the Lin-Shu dispersion relation ($m = 0$), which is obtained from equation (7). For $m$ and $J^2 \neq 0$ the border of this region of instability shifts to the line given by the BLLT condition (Eq. 11). The acoustic instability is bracketed by the two upper lines described by equation (13). The lower line corresponds to $\nu^2 = 1$ . This occurs when the Doppler-shifted frequency of oscillation, $(\omega - m\Omega)$, matches the epicyclic frequency, $\kappa$, and the self-gravity of the disk is balanced by the pressure force (the Jeans condition). The upper line corresponds to $\nu^2 = 1 + 2J^2\hat{\eta}^2$.

We can investigate the instability conditions (11) and (14) further by writing the BLLT dispersion relation without self-gravity. This can be done by multiplying equation (10) by $\epsilon^2$, and then substituting as above. We then let $\epsilon \to 0$ to turn off gravity. The BLLT dispersion relation becomes

$$\nu^4 - \left(2 + a^2\hat{k}^2/\kappa^2\right)\nu^2 + 1 + \frac{a^2\left(\hat{k}^2 + s^2m^2/r^2\right)}{\kappa^2} = 0. \qquad (2.15)$$

We combine the contributions to the dispersion relation from the sound speed and the epicyclic frequency by defining an angle $\gamma = \tan^{-1}(a\hat{k}/\kappa)$. We also define the

pitch angle of the spiral $p = \tan^{-1}(m/kr)$. For $\epsilon = 0$, equation (11) is never satisfied, so the BLLT instability disappears, as recognized by these authors. However, the acoustic instability remains, with an instability criterion given by equation (14) with $\epsilon = 0$; this is

$$\frac{a}{\kappa r} < \frac{2s \sin p}{\hat{k} r} = \frac{2sm}{k^2 r^2 + m^2}. \tag{2.16}$$

Another way to write equation (16) is to remove the explicit radial dependence; then the instability condition becomes

$$\tan\gamma \equiv \frac{a\hat{k}}{\kappa} < 2s \sin p. \tag{2.17}$$

The left hand side of equation (17) is the ratio of the length scale for the epicyclic oscillation to the interarm spacing. This ratio has to be less than order unity for the instability to develop, which means that there has to be room for epicyclic motions within the distance that separates the spiral arms. That is, spiral waves will grow at all wavelengths that have enough room for epicyclic motions at the local sound speed.

When equation (17) is satisfied, *a non-self-gravitating gaseous disk with differential rotation will be unstable to spiral perturbations.* For a disk with solid body rotation, $s = 0$, for a flat rotation curve, $s = \sqrt{2}$, and for a Keplerian disk, $s = \sqrt{6}$, so condition (17) is more easily satisfied, and the growth of instabilities is stronger, with greater shear. From equation (15), the phase velocity, $c_{ph}$, and the group velocity, $c_g$, of the acoustic waves, can be obtained. Define $z = (2s \sin p/\tan\gamma)^2$, and $w_\pm = (1 \pm \sqrt{1-z})/2$; then

$$\begin{aligned} c_{ph} &= m\Omega/k + \frac{\kappa}{k}\sqrt{1 + w_\pm \tan^2\gamma}, \\ c_g &= \pm a \frac{w_\pm \cos p \tan\gamma}{\sqrt{1-z}\sqrt{1 + w_\pm \tan^2\gamma}}. \end{aligned}$$

For vanishing $z$, $w_+$ becomes 1 and $c_g$ equals $a\cos p\sin\gamma$. Note that for trailing waves, which are the only waves considered here, $\cos p < 0$. This instability will be studied further in section 3 for the cases with flat rotation curves and Kepler rotation.

## 2.3. Higher Order Terms

For the general case with self-gravity, it is possible to solve for the complex frequency if we know the basic state of the disk. If the rotation curve, the density distribution, and the sound speed distribution in the disk are known, then the dispersion relation in the tightwinding approximation can be obtained to second order in $\epsilon$.

The dispersion relation for $\nu$ is obtained by turning equation (2) into an algebraic expression. This is done by using the definition of the enthalpy and equation (3) to express the enthalpy as a function of the potential and then using the asymptotic form of the potential, $\phi_1 = \Phi e^{i\int k(r)dr}$. We will consider only trailing spirals ($k < 0$). Note that $\nu' = -(m\Omega'/\kappa + \nu\kappa'/\kappa)$ for radial derivatives denoted by primes. Equation (2) can be written in the form:

$$\left[\frac{r^2\,d^2}{dr^2} + (Ar)\frac{r\,d}{dr} + Br^2\right](h_1 + \phi_1) = \delta^{-1}(1-\nu^2)h_1, \tag{2.18}$$

where $\delta = a^2/(\kappa^2 r^2)$. Multiply equation (18) by $\delta/h_1$ and define $D_0 = \delta(1-\frac{1}{f})$, $D_1 = \delta\frac{r}{h_1}\frac{d}{dr}(\phi_1 + h_1)$, and $D_2 = \delta\frac{1}{h_1}(\frac{r^2\,d^2}{dr^2} - m^2)(\phi_1 + h_1)$. Then

$$D_2 + (Ar)\,D_1 + (Br^2 + m^2)\,D_0 + \nu^2 - 1 = 0. \tag{2.19}$$

The terms $D_i$ are

$$D_0 = \delta\left(1 - \frac{1}{f}\right),$$

$$D_1 = \delta\left[\left(i\,k\,r+\frac{r\Phi'}{\Phi}\right)\left(1-\frac{1}{f}\right)+\frac{rf'}{f}\right]$$

$$D_2 = \delta\left(\left[-\hat{k}^2r^2+ikr\left(\frac{2r\Phi'}{\Phi}+\frac{r\,k'}{k}\right)+\frac{r^2\Phi''}{\Phi}\right]\left(1-\frac{1}{f}\right)+\frac{2rf'}{f}\left(ikr+\frac{r\Phi'}{\Phi}\right)+\frac{r^2f''}{f}\right),$$

These terms are used to find numerically the roots of the dispersion relation. They can be expanded in the small parameter $1/\hat{k}r$ by using the Bertin & Mark expression of Poisson's equation (Eqs. 4 and 5). Their expansion is correct to third order in $1/\hat{k}r$, so our dispersion relation is limited to third order in this quantity as well. In terms of $Q^2$ and $\hat{\eta}$, and to lowest order in $\epsilon$ $D_i$ become:

$$D_0 = \epsilon^2\left(\frac{Q^2}{4}-\hat{\eta}\right)+i\,\epsilon^3\hat{\eta}^2\,f_1+\ldots=\epsilon^2 d_{02}+i\,\epsilon^3 d_{03}+\ldots$$

$$D_1 = i\,\epsilon\cos p\left(\frac{Q^2}{4\hat{\eta}}-1\right)+\epsilon^2\left[\frac{Q^2}{4}\left(\frac{r\,\Phi'}{\Phi}+\frac{r\,\hat{k}'}{\hat{k}}-\frac{r\,k_J{}'}{k_J}\right)+\hat{\eta}\left(f_1\cos p-\frac{r\,\Phi'}{\Phi}\right)\right]+\ldots$$

$$= i\,\epsilon d_{11}+\epsilon^2 d_{12}+\ldots$$

$$D_2 = \frac{1}{\hat{\eta}}-\frac{Q^2}{4\,\hat{\eta}^2}+i\,\epsilon\left[\cos p\left(\frac{Q^2}{4\,\hat{\eta}}-1\right)\left(\frac{2\,r\,\Phi'}{\Phi}+\frac{r\,k'}{k}\right)-f_1+\cos p\,\frac{Q^2}{2\,\hat{\eta}}\left(\frac{r\,\hat{k}'}{\hat{k}}-\frac{r\,k_J{}'}{k_J}\right)\right]$$

$$+\epsilon^2\left(\frac{Q^2}{4}\frac{r\,\Phi''}{\Phi}-\hat{\eta}\left[\frac{r\,\Phi''}{\Phi}+\cos p\,f_1\left(\frac{2\,r\Phi'}{\Phi}+\frac{r\,k'}{k}\right)+{f_1}^2+f_2\right]\right)$$

$$= d_{20}+i\,\epsilon d_{21}+\epsilon^2 d_{22}+\ldots$$

These equations define the terms $d_{ij}$; note that alternate terms are imaginary as is typical for WKB approximation methods. Also note that $r\hat{k}'/\hat{k}=\cos^2 p\,rk'/k-\sin^2 p$, and that $rk_J{}'/k_J=r\sigma_0{}'/\sigma_0-2ra'/a$. We take $k$ to be constant. The terms $(A\,r)$ and $(B\,r^2+m^2)$ contain contributions of order unity divided by $\nu$ and $(\nu^2-1)$. To get a polynomial expression for $\nu$, we calculate the expressions

$$\nu(\nu^2-1)\,Ar = a_1\,\nu+a_2\,\nu^2+a_3\,\nu^3$$

$$\nu(\nu^2-1)(B\,r^2+m^2) = b_0+b_1\,\nu+b_2\,\nu^2$$

with

$$
\begin{aligned}
a_1 &= \frac{2r\kappa'}{\kappa} - 1 - \frac{r\sigma_0'}{\sigma_0} \\
a_2 &= \frac{2m\Omega}{\kappa}\frac{r\Omega'}{\Omega} \\
a_3 &= 1 + \frac{r\sigma_0'}{\sigma_0} \\
b_0 &= \frac{2m\Omega}{\kappa}\left(\frac{r\sigma_0'}{\sigma_0} + \frac{r\Omega'}{\Omega} - \frac{2r\kappa'}{\kappa}\right) \\
b_1 &= -\left(\frac{2m\Omega}{\kappa}\right)^2 \frac{r\Omega'}{\Omega} \equiv J^2/\epsilon^2 = s^2m^2 \\
b_2 &= -\frac{2m\Omega}{\kappa}\left(\frac{r\sigma_0'}{\sigma_0} + \frac{r\Omega'}{\Omega}\right).
\end{aligned}
$$

Equation (19) is now multiplied by $\nu(\nu^2 - 1)$ to obtain a general dispersion relation for fluid disks:

$$\nu^5 + c_3\nu^3 + c_2\nu^2 + c_1\nu + c_0 = 0, \tag{2.20}$$

where

$$
\begin{aligned}
c_3 &= -2 + d_{20} + i\,\epsilon(d_{21} + a_3 d_{11}) + \epsilon^2(d_{22} + a_3 d_{12}) + \ldots \\
&= c_{30} + i\,\epsilon c_{31} + \epsilon^2 c_{32} + \ldots, \\
c_2 &= i\,\epsilon a_2 d_{11} + \epsilon^2(a_2 d_{12} + b_2 d_{02}) + \ldots \\
&= i\,\epsilon c_{21} + \epsilon^2 c_{22} + \ldots, \\
c_1 &= 1 - d_{20} + d_{02}J^2 + i\,\epsilon(-d_{21} + a_1 d_{11} + J^2 d_{03}) + \ldots \\
&= c_{10} + i\,\epsilon c_{11} + \epsilon^2 c_{12} + \ldots, \\
c_0 &= \epsilon^2 b_0 d_{02} + i\,\epsilon^3 b_0 d_{03} + \ldots \\
&= \epsilon^2 c_{02} + i\,\epsilon^3 c_{03} + \ldots.
\end{aligned}
$$

This dispersion relation includes terms that have been neglected in previous studies. The effect of the higher order terms can be followed by the dependence of the coefficients $c_i$ on the small parameter $\epsilon$. In the limit of $\epsilon \rightarrow 0$, but with a finite $\hat{\eta}$ and finite $Q^2/\hat{\eta}^2$, the general dispersion relation (Eq. 20) becomes the BLLT dispersion relation (Eq. 10).

We investigate the effects of the higher order terms by expressing $\nu$ as an expansion in the parameter $\epsilon$, that is, $\nu = \nu_0 + \epsilon\nu_1 + \epsilon^2\nu_2 + ...$, and by solving for the roots of equation (19). Substituting the expansion for $\nu$ into equation (19) and setting coefficients of equal powers of $\epsilon$ to zero, we obtain expressions for the expansion terms $\nu_i$. The zeroth-order root, $\nu_0$, satisfies the equation

$$\nu_0 \left[\nu_0{}^4 - \nu_0{}^2 (2 - d_{20}) + 1 - d_{20} \left(1 + J^2 \hat{\eta}^2\right)\right] = 0. \tag{2.21}$$

The expression in the squared brackets of equation (21) is the BLLT dispersion relation as discussed above. The other solution ($\nu_0 = 0$) has no terms of order $\epsilon$; i.e., it is of the form $\nu = \nu_2 \epsilon^2 + \nu_3 \epsilon^3 + ....$

The first-order term that corresponds to the nonzero solution $\nu_0$ is

$$\nu_1 = -i \frac{\nu_0 (c_{11} + c_{21} \nu_0 + c_{31} \nu_0{}^2)}{c_{10} + 3c_{30} \nu_0{}^2 + 5\nu_0{}^4}; \tag{2.22}$$

for real $\nu_0$, this is purely imaginary; for imaginary $\nu_0$, it is complex.

The coefficients, $c_{i2}$, for the next term in the expansion, $\nu_2$, are pure real and, if $\nu_0$ is real, then this term is real also, and a factor of $\epsilon^2$ smaller. When $\nu_0$ is real, the growth rate to first order in $\epsilon$ is attributed to $\nu_1$. The next contribution to the growth rate will be from $\nu_3$, which is of order $\epsilon^2$ smaller.

In summary, we have found in this analysis a general dispersion relation that includes the effects of radial variations in the basic parameters of the disk and that is

accurate for relatively open multiple arm spirals. Furthermore, the effects included in this analysis change significantly the criterion for stability of the disk as shown explicitly by the models in the next section.

## 3. Models

Several models will be studied to illustrate the effects of the higher order terms in the dispersion relation and to investigate how different assumptions affect the stability of the disk. Four models will be considered: a self-gravitating disk with a flat rotation curve, a self-gravitating disk with solid body rotation, a non-self-gravitating disk with solid body rotation, and a non-self-gravitating disk with Keplerian rotation. The amplitude of the wave is assumed to be slowly varying so $r\,\Phi'/\Phi \ll 1$. This gives an arm/interarm contrast that increases with radius beyond one scale length, in agreement with observations (Schweitzer 1980; Elmegreen & Elmegreen 1984).

All disks considered here are assumed to have an exponential mass column density profile with a scale length $r_d$ and a constant sound speed, $a$. Then $r\,\sigma_0'/\sigma_0 = -r/r_d$ and $r\,a'/a = 0$.

We are considering here solutions to the dispersion relation obtained from a local analysis where there are gradients in the physical quantities of the equilibrium disk. This is relevant when the growth time for the perturbations is shorter than the time needed for the disturbances to travel to the boundaries. That is usually $10^9$ years to the outer boundary and $10^7$ years to the center for a circumnuclear disk. But the center boundary usually serves as a sink, as waves are shocked and energy is dissipated. Therefore we are justified in using a local analysis especially

in central disks. Similar gradients were also discussed in a global analysis by Bertin et al (1989). Gradients like these as well as curvature can lead to spatial variations in the amplitude, including singularities, even in cases where there are no time-dependent instabilities. An example is in Section 4. where curvature alone is shown to lead to Bessel function solutions that have singularities at $r = 0$ with no explicit time-dependent growth. We believe that these solutions give structure in galaxies (Elmegreen et al. 1998) like time-dependent instabilities.

The dispersion relations can be solved by either assuming $k$ real and $\omega$ complex, or $k$ complex and $\omega$ real. The Bessel function solutions are of the latter type. In the remainder of this section we consider $k$ real and constant and look for solutions with imaginary $\omega$. The result will be sinusoidal waves that grow exponentially with time, as in the usual stability analyses.

A third method of analysis would be to consider the initial value problem of time-dependent growth with shearing sinusoidal perturbations as in Goldreich & Lynden-Bell (1965) and Toomre (1981). When gravity is important, this leads to swing amplifier.

In the following subsections we will investigate analytically and numerically the dispersion relation for disks with different rotational properties. The relevant dispersion relation is Eq. (19). The same dispersion relation with explicit expansions in terms of the small parameter $\epsilon$ is Eq. (20) for self-gravitating disks. Another dispersion relation is derived for non-self-gravitating disks in the appropriate subsections.

### 3.1. Exponential self-gravitating disk with constant rotation velocity

We first find the roots of Eq. (19) at two scale lengths for an exponential disk with a constant rotation speed. In this case $r\,\Omega'/\Omega = r\,\kappa'/\kappa = -1$, and $\Omega/\kappa = 1/\sqrt{2}$. The value of $\epsilon = 1/(k_{crit}r)$ depends on the ratio of the disk to total mass (disk and halo) in the spiral region. A value of $\epsilon \sim 0.11$ corresponds to the Solar radius in the Galaxy, using the rotation curve model in Schmidt (1983) and a disk mass surface density of 48 $M_\odot$ $pc^{-2}$ (Kuijken & Gilmore 1989, 1991). We use a value of $\epsilon = 0.1$.

There are five roots of the dispersion relation. The root that corresponds to the greatest growth is always plotted in the figures here; this is the root with most negative imaginary component.

Figure 2 shows the components of the normalized frequencies $\nu$ in the $(k_{crit}/|k| \equiv \eta,\ Q^2)$ plane for two values of the azimuthal wavenumber, $m$ =2, and 5, obtained numerically using the full dispersion relation, equation (19) with coefficients up to third order in the small parameter $\zeta \equiv \epsilon\hat{\eta}$. To be clear, we write $k_{crit}/|k|$ instead of $\eta$ in the figures. The top figures show the negative of the imaginary component of the frequency, i.e., the growth rate normalized to the epicyclic frequency $\kappa$, with contour values $2^{i/4}$ for $i$ = -20 to 10. The bottom figures show the absolute values of the corresponding real frequencies with the same contours. The left figures correspond to $m = 2$ and the right correspond to $m = 5$. The values of the real and imaginary components are tabulated for some values of $Q^2$ and $k_{crit}/|k|$ in table 1; this will facilitate the interpretation of the contours.

The thick lines in the top plots of figure 2 indicate the loci of points where the normalized frequency, $\nu_{LB}$, equals 0 (corotation, lower line), $\pm 1$ (inner and outer Lindblad resonances, middle line) and $\pm\sqrt{1 + 2J^2\hat{\eta}^2}$ (upper line) in the BLLT

dispersion relation, equation (10). The BLLT instability condition, equation (11), is satisfied below the lower thick line. The new acoustic instability condition, equation (14), is satisfied between the middle and the upper thick lines.

The figure and table show that the growth rate decreases but remains finite for $k_{crit}/|k| \rightarrow 0$, and that at $k_{crit}/|k| = 0$, it increases with increasing $Q$. At intermediate values of $k_{crit}/|k|$, say 0.5, the growth rate is largest for $Q < 1$ and decreases to a minimum at $Q^2 \approx 2$, but again increases for increasing $Q^2$. The growth rate decreases for increasing $k_{crit}/|k|$ beyond 0.5 for constant values of $Q^2$. This pattern is observed for both $m$ values. A significant difference between the figures for $m = 2$ and $m = 5$ is that for higher $m$, the growth rate is larger over the plotted ($k_{crit}/|k|$, $Q^2$) plane than for low $m$, and for high $k_{crit}/|k|$, the growth rate remains relatively large for moderate values of $Q^2$ above the line $\nu_{LB} = 0$. This enhanced growth at high $m$ is because the $J$-parameter is proportional to $m$ and is contributing to the higher order terms in the dispersion relation.

Note that there is a kink in the lower right corner ($k_{crit}/|k| \approx 1.6$) of the $m$ =2 contour plot for the real component of the root. This occurs because in adjacent regions to the kink different real components have the most negative imaginary component.

Figure 2 and table 1 also indicate that the greatest growth occurs for small values of $Q^2$, just as predicted using the BLLT dispersion relation (cf. Sect. 2.2). Moreover, they indicate that the disk is unstable to form spirals for a wide range of $Q$ and $m$, although the growth rate is low, of order $\epsilon$, when $Q$ is large. This implies there is still a spiral instability at low gravity. For most bright galaxies, however, the region where the rotation curve is flat is also the region where $Q$ is relatively small, so these high $Q$ solutions are not important. They could be important in early type

galaxies (Caldwell et al. 1992) or low surface brightness galaxies (van der Hulst et al. 1993) where $Q$ is high in the main disk.

### 3.2. Exponential self-gravitating disk with solid body rotation

The inner parts of galaxies and small galaxies typically have rotation curves that are approximately solid body. This is the result of a strong bulge with a nearly uniform central density in some spiral galaxies, and a relatively dense dark matter halo in dwarf galaxies. Inner galaxy disks (Elmegreen et al. 1998) and dwarfs (Hunter et al. 1998) may also be weakly self-gravitating for some time (e.g., between accretion events and starbursts), and so the high-$Q$ cases studied here may have applications there. Furthermore, inner disks and dwarfs have short rotation times, so the actual growth factor of a spiral instability can be large even if the normalized growth rate is small.

For solid body rotation, $r\,\Omega'/\Omega = r\,\kappa'/\kappa = 0$, and $\Omega/\kappa = 1/2$. We assume a value for $\epsilon = 0.1$ as in the previous section. In this case the term $A(r)$ does not depend on $\nu$ and $B(r)$ has a $1/\nu$ dependence. The dispersion relation then becomes cubic in $\nu$:

$$\nu^3 + (-1 + D_2 + a_3\,D_1)\,\nu + b_2\,D_0 = 0, \tag{2.23}$$

where the terms $D_i$, $a_3$, and $b_2$ were defined in the previous section. The roots can be expressed as an expansion in $\epsilon$, writing $\nu = \nu_0 + \nu_1\,\epsilon + \nu_2\,\epsilon^2 + ....$ The zero order term is the Lin-Shu dispersion relation, equation (7), with $\eta$ replaced by $\hat{\eta}$. The first order term is

$$\nu_1\,\epsilon = -i\,\epsilon\,\frac{\cos p}{2\,\nu_0}\left[\frac{Q^2}{4\,\hat{\eta}}\left(1 - \frac{r\sigma_0'}{\sigma_0} - 2\,\sin^2 p\right) - \frac{1}{2} - \frac{r\,\sigma_0'}{\sigma_0} + \frac{\sin^2 p}{2}\right]. \tag{2.24}$$

In the region where $\nu_0$ is real, the growth rate is dominated by the first order term.

In the region where $|\nu_0|$ is of order 1, $\nu_1 \sim -i$ and the growth rate is of order $i\nu_1 \epsilon \approx \epsilon$. For an exponential disk at two scale lengths $\frac{r\sigma_0'}{\sigma_0} = -2$, so

$$\nu_1 \epsilon = -i \epsilon \frac{\cos p}{2\nu_0} \left[ \frac{Q^2}{4\hat{\eta}} \left(3 - 2\sin^2 p\right) + \frac{\sin^2 p + 3}{2} \right]. \tag{2.25}$$

Figure 3 and table 2 show real and imaginary components of the normalized roots of the full dispersion relation (23) for the rising rotation curve model at $r = 2r_d$. Again we display only the root that corresponds to the fastest growth. We can see from the left-hand regions in the $(k_{crit}/|k|, Q^2)$ plot, where the absolute values of the real components are large, that the growth rates become small for small $k_{crit}/|k|$. The opposite occurs for small values of the real component, which are in the lower region of the plot. Where the real component is of order 1, in the center of the plot, the growth rate is of order $\epsilon$.

The detailed behavior of the growth rate in this case can be followed from the approximate analytical solution written above as equation (24). For example, equation (24) gives the same growth rate as the full solution in table 2 for $\eta = k_{crit}/|k| = 0.2$ for both $m = 2$ and 5, because the approximate equation is relatively accurate for low $\hat{\eta}$. Equation (24) gives slightly different rates than table 2 for $\eta = 0.6$; at $m = 2$ and $Q^2 = 2$, 5, and 10, equation (24) has growth rates of 0.232, 0.228 and 0.275 while table 2 has more precise growth rates of 0.227, 0.225 and 0.273. The rates given by equation (24) differ more significantly from those calculated by equation (23) when $\eta > 0.6$.

One can observe from table 2 that the real component corresponding to the greatest growth rate in the $(k_{crit}/|k|, Q^2)$ plane is always negative, i.e., it corresponds to the Lin-Shu and BLLT solutions inside of corotation in the disk.

Figures 2 and 3 show that there is a similarity between the growth rates for the

flat and solid body rotation curve models. Both figures display a saddle shape for the growth rate contours; the greatest growth occurs as $Q^2 < 1$, and for $k_{crit}/|k| \approx 0.5$, the growth rate first decreases and then increases with increasing $Q^2$. The main difference between the two models occurs for large numbers of spiral arms, where the growth rate is smaller at $m = 5$ than $m = 2$ for the solid body case, and larger at $m = 5$ than $m = 2$ in the flat rotation curve case. This is because for solid body rotation, $J = 0$, so the absence of differential rotation reduces the growth rate of waves at any $m \neq 0$. The zero order BLLT instability condition (Eq. (11)) is reduced to the Lin-Shu instability condition (Eq. (7)), and the acoustic instability disappears as the upper unstable region collapses around $\nu^2 \approx 1$. In addition, the contributions of $J^2$ to the higher order terms $\nu_i$ are also absent so the growth rate is less than for $J^2 > 0$.

The solutions shown for all the self-gravitating models indicate that disks are weakly unstable to spiral waves when $\epsilon = 1/(k_{crit}r) > 0$, even in the limit of weak self-gravity. This is the first time spiral disk instabilities have been found at large $Q$ in the absence of magnetic fields. We pursue this result further in the next section, which considers the growth of waves in the absence of self-gravity, that is, when $\epsilon = 0$.

### 3.3. Exponential disk with solid body rotation and no self-gravity

This section and the next consider gaseous disks without self-gravity as an idealization of the high $Q$ cases found to be unstable in the previous sections. To be consistent with the radial dependence of the enthalpy amplitude, $H(r)$, used before, which was defined in terms of a constant potential $\Phi$, we now assume $H(r) \propto -f(r)$, where $f$ was given in the discussion following equation (5).

From equation (24) we can see that the growth rate of the instability depends on both the self-gravity of the disk and the radial derivative of the background surface density. The normalized growth rate is, to first order, $\nu_1\,\epsilon$, from the previous discussion. The first term in equation (24) is proportional to $Q^2\cos p\epsilon/(4\hat{\eta}) = k\,a^2/\kappa^2\,r$, which is independent of the self-gravity of the disk. It depends primarily on the disk curvature, i.e., on the ratio of the square of the semimajor axis of an epicycle caused by random motions ($a/\kappa$), to the product of the wave scale ($k^{-1}$) and the disk radius ($r$). The second term is proportional to $\epsilon \propto mass_d/mass_{total}$, which comes from the self-gravity of the disk. If the disk self-gravity is neglected, $\epsilon = 0$ and the second term is zero, but there is still growth from the first term, depending on orbital curvature. When $\epsilon = 0$, the expansion has to be made in terms of the small parameter $\zeta \equiv 1/\hat{k}r$. Then we get:

$$\begin{aligned} \nu_0 &= \pm\sqrt{1+\left(a\,\hat{k}\right)^2/\kappa^2}, \\ \nu_1\,\zeta &= i\,\frac{k\,a^2}{2\,\kappa^2\,r\,\nu_0}\left(2\,\sin^2 p - \frac{r}{r_d} - 1\right). \end{aligned} \tag{2.26}$$

(2.27)

When the expression inside the parenthesis of equation (26) is zero for some particular pitch angle $p$, there is no growth at that radius, but there is growth at adjacent radii.

The numerical solutions to equation (23) when gravity is neglected are shown for $r = 2\,r_d$ in figure 4 and table 3, using normalized axes $(a/\kappa r)^2$ instead of $Q^2$ and $1/kr$ instead of $k_{crit}/|k|$. To compare the growth rates with the previous models, recall that the value of the vertical axis in figure 4 is obtained by multiplying the value of the vertical axis in our previous figures by $\epsilon^2 = 0.01$, and the value of the horizontal axis in figure 4 is obtained by multiplying the previous value of the horizontal axis by $\epsilon$=0.1. This means that the growth rates in figure 4 are analogous

to those in the lower left corner in figure 3. Figure 4 and table 3 indicate that the growth rate remains finite, proportional to $(a/\kappa r)$, as $|kr| \rightarrow \infty$. We infer from this behavior that the instability is acoustic in nature, similar to that described in section 2.2, but in the absence of self-gravity and shear. It is driven by curvature and pressure gradients in the disk (*cf.* section 4).

### 3.4. Exponential disk with Keplerian rotation and no gravity

Accretion disks around black holes (Nakai et al. 1993) and protostars have negligible self-gravity and may have Keplerian rotation. In this case $r\kappa'/\kappa = r\Omega'/\Omega = -3/2$, and equation (2) becomes a fifth order polynomial in $\nu$, as for a flat rotation curve. As in the previous section, an acoustic instability is still present even in the absence of self-gravity. The dispersion relation for this acoustic instability is now obtained from equation (19) with the modifications

$$\begin{aligned} D_0 &= \delta \\ D_1 &= \delta\left(ikr + \frac{rf'}{f}\right) \\ D_2 &= \delta\left(-\hat{k}^2r^2 + 2ikr\frac{rf'}{f} + \frac{r^2f''}{f}\right). \end{aligned}$$

Because there is no self-gravity, this fifth order dispersion relation has to be expanded to successive orders in $\zeta = 1/\hat{k}r$ instead of $\epsilon$, giving $\nu = \nu_0 + \nu_1\zeta + \nu_2\zeta^2 \ldots$. The zero-order term in this expansion is the modified BLLT dispersion relation, equation (15). Recall that the geometric term for a Keplerian disk is $s = \sqrt{6}$. The zero order term becomes complex when the instability condition, equation (17), is satisfied. When equation (17) is not satisfied, the growth rate is dominated by the first order

term

$$\nu_1\zeta = -i\frac{a^2k}{2\kappa^2 r}\frac{\left(1+r/r_d-2\sin^2 p\right)\left({\nu_0}^2-1\right)-3\left(1+m\nu_0\right)}{\nu_0\left(2{\nu_0}^2-2-a^2\hat{k}^2/\kappa^2\right)}. \qquad (2.28)$$

Figure 5 and table 4 display numerical solutions to the fifth order polynomial, equation (19), for the dispersion relation in this Keplerian model using the modified expressions $D_i$ when self-gravity is neglected. The real and imaginary components of the root with the largest growth rate are plotted using the same axes as in the previous section, $(1/|kr|,\ a^2/\kappa^2r^2)$. The critical curve for stability, equation (16), is plotted in the top figures as a thick line. To the left of the critical curve, equation (16) is not satisfied and the disk is stable against acoustic instabilities. To the right of the critical curve, equation (16) is satisfied and the acoustic instability dominates the growth of perturbations. The growth rate is larger than that in the case of solid body rotation without self-gravity because shear stimulates growth. There are discontinuities in the contours for the real component, with kinks at the same locations in the contours of the imaginary growth rate near the critical curve. To the left of the discontinuity in the plots for $m = 2$ and $m = 5$, the zero order term is pure real. The first order term is then contributing to the growth rate. To the right of the discontinuity, the zero order term is the main contributor to the growth rate. Equation (28) which is the first order approximation to the growth rate matches the full numerical solutions in figure 5 and table 4 to two significant digits for $\hat{k}r > 5$ and $(a^2/\kappa^2r^2) < 0.1$.

## 4. Contribution of Curvature Terms to Growth

We have just shown that differential rotation, curvature, and radial gradients in the basic properties of a fluid disk affect the propagation and growth of spiral disturbances. Differential rotation, through the parameter $s$, affects the stability

of the disk even in the absence of self-gravity. The effect of radial gradients has also been shown to contribute to the growth of perturbations. Now we simplify the problem for greater clarity by considering only the effects of orbital curvature.

The curvature terms can be illustrated by considering an ideal disk with solid-body rotation, constant surface density, and negligible self-gravity. Such disks may be appropriate for the central regions of quiescent galaxies, such as NGC2207 (Elmegreen et al. 1998). The governing equation (2) for such a disk, assuming constant surface density, becomes

$$\frac{d^2h_1}{dr^2} + \frac{1}{r}\frac{dh_1}{dr} + (\frac{\kappa^2}{a^2}(\nu^2 - 1) - \frac{m^2}{r^2})h_1 = 0. \tag{2.29}$$

To find the stability criterion, we can either assume a solution of the form $h_1 \propto e^{ikr}$ and obtain a dispersion relation, as we did before, or we can directly analyze the differential equation. In the first approach, we have

$$\nu^2 = [(\frac{a}{\kappa r})^2(r^2k^2 + m^2) + 1] - irk. \tag{2.30}$$

For $\nu_R >> \nu_I$, we recover the same result as equation (26) in the limit $r_d \to \infty$, assuming constant enthalpy amplitude:

$$\nu_R = \pm[(\frac{a}{\kappa r})^2(r^2k^2 + m^2) + 1]^{1/2}, \quad \nu_I = -\frac{1}{2}(\frac{a}{\kappa r})^2\frac{rk}{\nu_R}.$$

This gives us the growth rate of a wave with azimuthal wavenumber $m$ and radial wavenumber $k$.

The dispersion relation (30) may be also regarded as an equation for $k$, in which $\nu$ is held as a real variable. Then the solution will yield the local growth rate of the wave as it propagates in the radial direction. This in fact gives us a better idea of how the curvature effect works. Normally we can solve for $k$ from the dispersion relation and decide how the wave will propagate or get amplified according to the

roots of $k$. However, equation (29) is the well known Bessel equation. When

$$\frac{\kappa^2}{a^2}(\nu^2 - 1) \equiv {k_B}^2 > 0,$$

it admits Bessel functions $J_m(k_B r)$ and $Y_m(k_B r)$ as its solutions; $k_B$ is the radial wavenumber. It is also well known that when $k_B r$ is large, $J_m$ and $Y_m$ behave like sine and cosine, which may be combined as outgoing or incoming waves with $\exp(i\omega t)$. When $k_B r$ is small, however, these waves grow algebraically with decreasing $r$. The growth arises directly from the curvature terms, namely, the first derivative term and the $m^2/r^2$ term. The latter actually defines a region within which the waves start to grow out of bounds, i.e., when $r < m/k_B$ for $m \neq 0$. Eventually the nonlinear and dissipative effects come into play. We expect the waves will break in the form of shocks shortly after they enter the inner region. This explains for the case of NGC2207 (Elmegreen et al. 1998) why the multiple-arm features are only observed in the outer part of the nuclear disk, while the $m = 1$ and ring-like feature is close to the center.

These waves also propagate in the azimuthal direction with angular speed $\omega/m$ as long as $\nu^2 - 1 > 0$, this implies that waves with different $m$ will interact, forming complex structures. The waves are also dispersive, with dispersion relation

$$\frac{\omega - m\Omega}{\kappa} = \pm(1 + \frac{a^2 {k_B}^2}{\kappa^2})^{1/2}.$$

They form wave packets that propagate with group velocity

$$c_g = \pm a \sin \gamma_B,$$

with $\gamma_B = \tan^{-1} a k_B/\kappa$. Undoubtedly the waves will interact because of these various phase and group speeds. They will also get sheared by differential rotation in reality to form complex spiral structures. When $\nu^2 - 1 < 0$, the entire disk is evanescent; then we should not see any waves.

So far we have ignored the exponential density distribution of the disk. If it is taken into consideration, equation (29) will change to

$$\frac{d^2h_1}{dr^2} + \frac{1}{r}\left(1 - \frac{r}{r_d}\right)\frac{dh_1}{dr} + \left[\frac{\kappa^2}{a^2}\left(\nu^2 - 1\right) - \frac{m^2}{r^2} + \frac{m}{\nu r r_d}\right]h_1 = 0, \qquad (2.31)$$

where $r_d$ is the scale length of the exponential disk. The additional factor in the first derivative term will modify the behavior of the Bessel functions when $r \geq r_d$, and the additional term in the last parenthesis will complicate the wave behavior. But the qualitative nature of the Bessel function solutions does not change.

## 5. Summary

We have obtained dispersion relations for spiral waves with multiple arms. When the effects of out-of-phase terms, curvature, and radial gradients are ignored, differential rotation alone provides a source of instability for sonic waves with small values of the parameter $a/(\kappa r)$ (cf. Eq. 16), even in the absence of self-gravity ($\epsilon = 0$). This is apparently a new instability, not discussed in the literature, which might be called a *zero-order acoustic* instability.

When self-gravity is present, instability at lowest order in the parameter $\epsilon$ (cf. Eq. 1) is driven by both shear and self-gravity. Then there are two independent instability conditions, either of which can cause spiral waves. These are equations (11) and (14). The first of these comes from Bertin et al. (1989), and contains the Toomre (1964) instability condition, $Q < 1$, as a special case for ring-like perturbations ($m = 0$, which gives $J = 0$). This first instability is the spiral instability that is commonly discussed in the literature as a source of multiple arm and grand design spiral structure in galaxy and protoplanetary disks. The second of these conditions is also driven by pressure, shear and self-gravity, but arises from a

different combination of parameters than the first when $Q^2 > 4\hat{\eta}$ (cf. Eq. 13).

We also found additional instabilities coming from higher order terms in an expansion of the dispersion relation, equation (19) around the small parameter $\epsilon$. These additional instabilities are present even when the BLLT and Toomre instability conditions are not satisfied, i.e., when the low order terms give stability. The source of these residual instabilities is a combination of orbital curvature [terms of order $1/(kr)$], self-gravity (terms of order $\epsilon$), and various disk gradients ($r\sigma'/\sigma$, $ra'/a$, etc.), including shear (the $J$ or $s$ terms). Growth rates for these residual instabilities were given to all orders in $\epsilon$ for flat and rising rotation curves by figures 2 and 3 and tables 1 and 2, and they were given to first order in $\epsilon$ by equation (24) for solid body rotation. The residual instability that arises from self-gravity and orbital curvature (through $\epsilon$), discussed in sections 3.1 and 3.2, is termed a *higher order gravitational-curvature* instability. The residual instability that arises from a combination of pressure and orbital curvature [through $a/(\kappa r)$], discussed in sections 3.3 and 3.4, is termed a *higher order acoustic-curvature* instability, because it operates even without self-gravity.

These three new instabilities should be important for gaseous disks with negligible or weak self-gravity, including proto-planetary disks, gaseous disks around black holes, some galactic nuclear disks, low surface brightness galaxy disks, and some dwarf galaxies. In these cases, zero order acoustic and higher order acoustic-curvature and gravitational-curvature instabilities can lead to the growth of spiral or other structures in about an orbital time. They are most important in the region close to the center where the orbital time is small.

Non-linear effects arising from these waves may ultimately lead to visible dust lanes (Elmegreen et al. 1998) and associated gaseous shocks (Roberts 1969)

in even the most weakly self-gravitating disks, with the possibility of heightened self-gravity and star formation in some of the compressed regions (e.g., Elmegreen 1994). Non-linear effects might also promote accretion flows (e.g., Larson 1990). Indeed, the ubiquity of acoustic waves in disks implies that galactic nuclear accretion should occur in a wide variety of environments with or without shear, self-gravity, or magnetic fields.

## REFERENCES

Bertin, G. & Mark, J W-K. 1979, SIAM, J. Appl. Math., 36, 407

Bertin, G., Lin, C.C., Lowe, S.A. & Thurstan, R.P. 1989, ApJ, 338, 104

Caldwell, N., Kennicutt, R., Phillips, A. C. & Schomer, R. A. 1992, ApJ, 370, 526

Elmegreen, B.G. 1994, ApJ, 433, 39

Elmegreen, D.M. & Elmegreen, B.G. 1984, ApJS, 54, 127

Elmegreen, B.G., Elmegreen, D.M., Brinks, E., Yuan, C., Kaufman, M., Klarić, M., Montenegro, L., Struck, C. & Thomasson, M. 1998, ApJL, in press

Goldreich, P. & Lynden-Bell, D. 1965, MNRAS, 130, 125

Goldreich, P. & Tremaine, S. 1979,ApJ, 233, 857.

Hunter, C. 1983, in Lectures in Applied Mathematics, 20, p. 179

Hunter, D. A., Elmegreen, B. G. & Baker, A. L. 1998, ApJ, 493, 595

Kuijken, K. & Gilmore, G. 1989, MNRAS, 239, 605

Kuijken, K. & Gilmore, G. 1991, ApJ367, L9

Larson, R. B. 1990, MNRAS, 243, 588

Lau, Y. Y. & Bertin, G. 1978, ApJ, 226, 508

Lin, C.C. & Lau, Y. Y 1979, Studies in Appl. Math., 60, 97.

Lin, C.C. & Shu, F. H 1966, Proc. Nat. Acad. Sci., 55, 229

Lin, C.C. & Shu, F. H 1964, ApJ, 140, 646

Lindblad, B. 1958. Stock. Obs. Ann., 20, No. 6

Nakai, N., Inoue, M. & Miyoshi, M. 1993, Nature, 361, 45

Roberts, W.W. 1969, ApJ, 158, 123

Rubin, V.C., Burstein, D., Ford, W.K. & Thonnard, A. 1985, ApJ, 289, 81

Schmidt, M. 1985, in IAU Symposium 106, The Milky Way Galaxy, ed. H. van Woerden, Dordrecht: Reidel, 203

Schweizer, F. 1980, ApJS, 31, 313

Toomre, A. 1964, ApJ, 139, 38

Toomre, A. 1981, in The Structure and Evolution of Normal Galaxies, eds. Fall, S. M., & Lynden-Bell, D., Cambridge: Cambridge Univ. Press, 111

van der Hulst, J. M., Skillman, E. D., Smith, P. R., Bothun, G. D., Mc Gaugh, S. S. & de Block, W. J. G. 1993, AJ, 106, 548

Zang, T.A., 1976, Ph.D. thesis, M.I.T.

---

This manuscript was prepared with the AAS LaTeX macros v4.0.

Table 1. Flat rotation curve at $r = 2r_d$

| $Q^2$ | $\frac{k_{crit}}{\|k\|} =$ | 0.2 | 0.6 | 1.0 | 1.4 | 1.8 | 0.2 | 0.6 | 1.0 | 1.4 | 1.8 |
|---|---|---|---|---|---|---|---|---|---|---|---|
| | | | $m = 2$ | growth rate | | | | $m = 2$ | frequency | | |
| 10 | | 0.280 | 0.332 | 0.340 | 0.325 | 0.302 | -7.660 | -2.547 | -1.644 | -1.318 | -1.164 |
| 5 | | 0.218 | 0.272 | 0.264 | 0.236 | 0.214 | -5.229 | -1.709 | -1.156 | -0.973 | -0.892 |
| 2 | | 0.175 | 0.236 | 0.213 | 0.184 | 0.168 | -2.924 | -0.864 | -0.673 | -0.658 | -0.664 |
| 1 | | 0.188 | 0.383 | 0.221 | 0.163 | 0.147 | -1.513 | -0.297 | -0.402 | -0.510 | -0.568 |
| 0.1 | | 1.867 | 0.875 | 0.410 | 0.179 | 0.130 | -0.042 | -0.054 | -0.116 | -0.301 | 0.457 |
| | | | $m = 5$ | growth rate | | | | $m = 5$ | frequency | | |
| 10 | | 0.319 | 0.421 | 0.453 | 0.446 | 0.427 | -7.695 | -2.653 | -1.797 | -1.493 | -1.348 |
| 5 | | 0.258 | 0.364 | 0.358 | 0.309 | 0.262 | -5.255 | -1.787 | -1.256 | -1.058 | -0.942 |
| 2 | | 0.215 | 0.275 | 0.322 | 0.358 | 0.385 | -2.941 | -0.853 | -0.529 | -0.420 | -0.372 |
| 1 | | 0.224 | 0.581 | 0.559 | 0.544 | 0.540 | -1.531 | -0.238 | -0.229 | -0.241 | -0.249 |
| 0.1 | | 1.914 | 1.057 | 0.810 | 0.714 | 0.673 | -0.044 | -0.073 | -0.116 | -0.156 | -0.183 |

## Table 2. Solid body rotation at $r = 2r_d$

| $Q^2$, $\frac{k_{crit}}{\|k\|}$ = | 0.2 | 0.6 | 1.0 | 1.4 | 1.8 | 0.2 | 0.6 | 1.0 | 1.4 | 1.8 |
|---|---|---|---|---|---|---|---|---|---|---|
| | | $m = 2$ | growth rate | | | | $m = 2$ | frequency | | |
| 10 | 0.254 | 0.273 | 0.268 | 0.250 | 0.229 | -7.658 | -2.540 | -1.634 | -1.311 | -1.163 |
| 5 | 0.193 | 0.225 | 0.223 | 0.206 | 0.188 | -5.228 | -1.703 | -1.155 | -0.992 | -0.930 |
| 2 | 0.154 | 0.227 | 0.211 | 0.183 | 0.164 | -2.922 | -0.881 | -0.723 | -0.727 | -0.748 |
| 1 | 0.173 | 0.376 | 0.244 | 0.184 | 0.158 | -1.512 | -0.389 | -0.508 | -0.610 | -0.673 |
| 0.1 | 1.838 | 0.789 | 0.361 | 0.206 | 0.158 | -0.052 | -0.121 | -0.306 | -0.483 | -0.594 |
| | | $m = 5$ | growth rate | | | | $m = 5$ | frequency | | |
| 10 | 0.252 | 0.251 | 0.222 | 0.187 | 0.157 | -7.692 | -2.636 | -1.770 | -1.464 | -1.323 |
| 5 | 0.192 | 0.208 | 0.190 | 0.166 | 0.144 | -5.252 | -1.766 | -1.227 | -1.056 | -0.983 |
| 2 | 0.152 | 0.215 | 0.207 | 0.186 | 0.169 | -2.938 | -0.901 | -0.709 | -0.680 | -0.674 |
| 1 | 0.171 | 0.406 | 0.311 | 0.257 | 0.226 | -1.523 | -0.382 | -0.451 | -0.507 | -0.537 |
| 0.1 | 1.843 | 0.829 | 0.487 | 0.372 | 0.320 | -0.053 | -0.135 | -0.292 | -0.392 | -0.443 |

Table 3. Solid body rotation with no gravity at $r = 2\,r_d$

| $(\frac{a}{\kappa r})^2$, $\frac{1}{\lvert k\,r\rvert}$ = | 0.2 | 0.6 | 1.0 | 1.4 | 1.8 | 0.2 | 0.6 | 1.0 | 1.4 | 1.8 |
|---|---|---|---|---|---|---|---|---|---|---|
| | | $m = 2$ | growth rate | | | | $m = 2$ | frequency | | |
| 1.0 | 1.205 | 0.482 | 0.376 | 0.433 | 0.462 | -5.584 | -2.816 | 0.777 | 0.917 | 0.995 |
| 0.5 | 0.833 | 0.311 | 0.308 | 0.355 | 0.377 | -4.024 | -2.160 | 0.671 | 0.769 | 0.820 |
| 0.2 | 0.499 | 0.168 | 0.139 | 0.137 | 0.131 | -2.673 | -1.608 | 0.493 | 0.559 | 0.598 |
| 0.1 | 0.328 | 0.101 | 0.051 | 0.032 | 0.022 | -2.026 | -1.355 | -1.294 | -1.279 | -1.274 |
| 0.01 | 0.058 | 0.014 | 0.007 | 0.004 | 0.003 | -1.148 | -1.045 | -1.037 | -1.035 | -1.034 |
| | | $m = 5$ | growth rate | | | | $m = 5$ | frequency | | |
| 1.0 | 0.684 | 0.179 | 0.097 | 0.067 | 0.051 | -7.173 | -5.420 | -5.271 | -5.230 | -5.214 |
| 0.5 | 0.474 | 0.122 | 0.066 | 0.045 | 0.035 | -5.147 | -3.941 | -3.840 | -3.812 | -3.801 |
| 0.2 | 0.287 | 0.071 | 0.039 | 0.026 | 0.020 | -3.375 | -2.657 | -2.597 | -2.581 | -2.575 |
| 0.1 | 0.192 | 0.046 | 0.025 | 0.017 | 0.013 | -2.509 | -2.036 | -1.997 | -1.987 | -1.983 |
| 0.01 | 0.039 | 0.008 | 0.004 | 0.003 | 0.002 | -1.252 | -1.162 | -1.156 | -1.154 | -1.153 |

Table 4. Keplerian rotation with no gravity at $r = 2r_d$

| $(\frac{a}{\kappa r})^2$, $\frac{1}{\lvert k r \rvert}$ = | 0.2 | 0.6 | 1.0 | 1.4 | 1.8 | 0.2 | 0.6 | 1.0 | 1.4 | 1.8 |
|---|---|---|---|---|---|---|---|---|---|---|
| | | $m = 2$ | growth rate | | | | $m = 2$ | frequency | | |
| 1.0 | 1.606 | 1.088 | 1.266 | 1.365 | 1.414 | -5.736 | -2.960 | 2.170 | 2.081 | 2.040 |
| 0.5 | 1.220 | 0.914 | 1.076 | 1.139 | 1.171 | -4.161 | 2.010 | 1.818 | 1.748 | 1.715 |
| 0.2 | 0.861 | 0.739 | 0.821 | 0.856 | 0.875 | -2.787 | 1.621 | 1.489 | 1.439 | 1.415 |
| 0.1 | 0.665 | 0.597 | 0.645 | 0.667 | 0.679 | -2.121 | 1.419 | 1.320 | 1.281 | 1.262 |
| 0.01 | 0.249 | 0.236 | 0.242 | 0.246 | 0.248 | -1.197 | 1.102 | 1.068 | 1.055 | 1.048 |
| | | $m = 5$ | growth rate | | | | $m = 5$ | frequency | | |
| 1.0 | 1.413 | 0.961 | 1.097 | 1.140 | 1.160 | -7.262 | 4.327 | 4.007 | 3.885 | 3.821 |
| 0.5 | 1.214 | 1.266 | 1.355 | 1.382 | 1.395 | -5.220 | 3.253 | 3.076 | 3.008 | 2.972 |
| 0.2 | 1.041 | 1.231 | 1.276 | 1.291 | 1.298 | -3.450 | 2.394 | 2.291 | 2.250 | 2.228 |
| 0.1 | 0.932 | 1.089 | 1.117 | 1.126 | 1.130 | -2.607 | 1.960 | 1.888 | 1.859 | 1.843 |
| 0.01 | 0.506 | 0.539 | 0.544 | 0.546 | 0.547 | 1.370 | 1.229 | 1.205 | 1.195 | 1.190 |

Fig. 1.— Regions of instability in a self-gravitating disk with constant rotation for 5 arm spirals ($m = 5$). The lowest (thin) line borders the instability condition obtained from the Lin-Shu dispersion relation (Eq. (7)) for $m$ and $J^2 = 0$. The three upper lines bracket regions of zero-order instabilities obtained in the Lau-Bertin dispersion relation. The border of the Lin-Shu region of instability shifts to the lower thick line for nonzero $J^2$. This line is from Eq. (11) for the usual Lau-Bertin stability condition; the two upper thick lines are the boundaries enclosing the acoustic instability according to Eq. (13). The shading of the unstable regions gives an indication of the growth rate. The most unstable region is in the bottom left corner of the figure.

Fig. 2.— Contours showing the maximum growth rates (top) and corresponding frequencies (bottom) for instabilities to all orders of the small parameter $\epsilon$ in a self-gravitating disk with a constant rotation velocity and an exponential density profile, evaluated at two scale lengths. Solutions for two arm spirals ($m = 2$) are on the left, and for 5 arm spirals ($m = 5$) are on the right. The thick lines are obtained as in Fig. 1., they border the regions of zero-order instability for the Lau-Bertin dispersion relation. The bottom thick line is from Eq. (11) for the usual Lau-Bertin stability condition; the middle and upper lines are the boundaries enclosing the acoustic instability according to Eq. (13).

Fig. 3.— Same as Fig. 2 for a self-gravitating, exponential disk at two scale lengths, but now with solid body rotation. The thick lines on the top figures border the regions of instability for the zero-order Lau-Bertin dispersion relation in the case with no shear ($J = 0$ in Eq. (11)).

Fig. 4.— Same as Fig. 3, but to all orders of the small parameter $1/|kr|$ in the absence of self-gravity. All of the unstable growth exhibited in these solutions is from high order terms.

Fig. 5.— Growth rates and frequencies for a non-self-gravitating disk, as in Fig. 4, but with Keplerian rotation. The thick lines on the top figures border the regions of instability for the zero-order, Lau-Bertin dispersion relation in a Keplerian disk without self-gravity (Eq. 16).

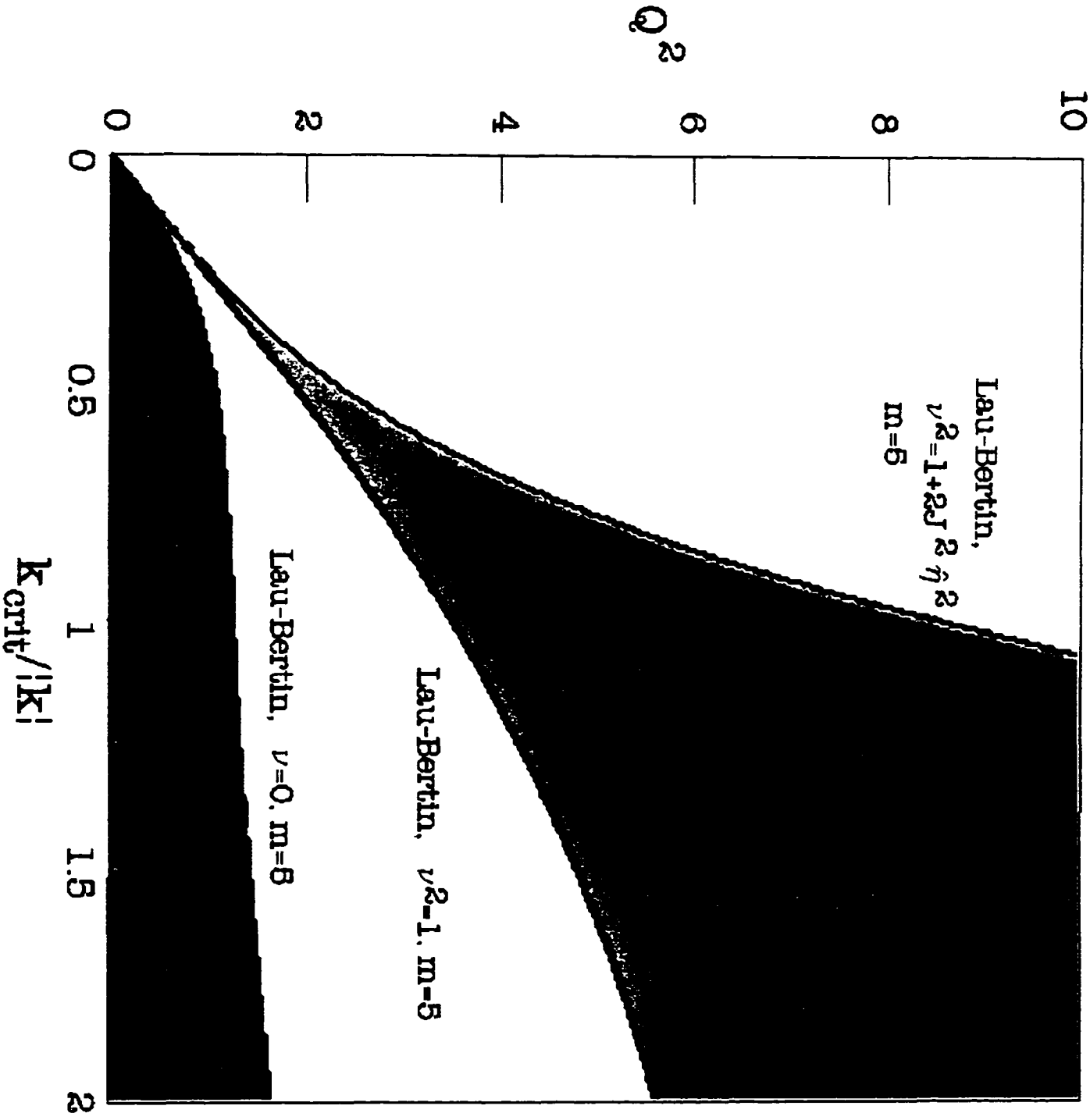


Figure 1.

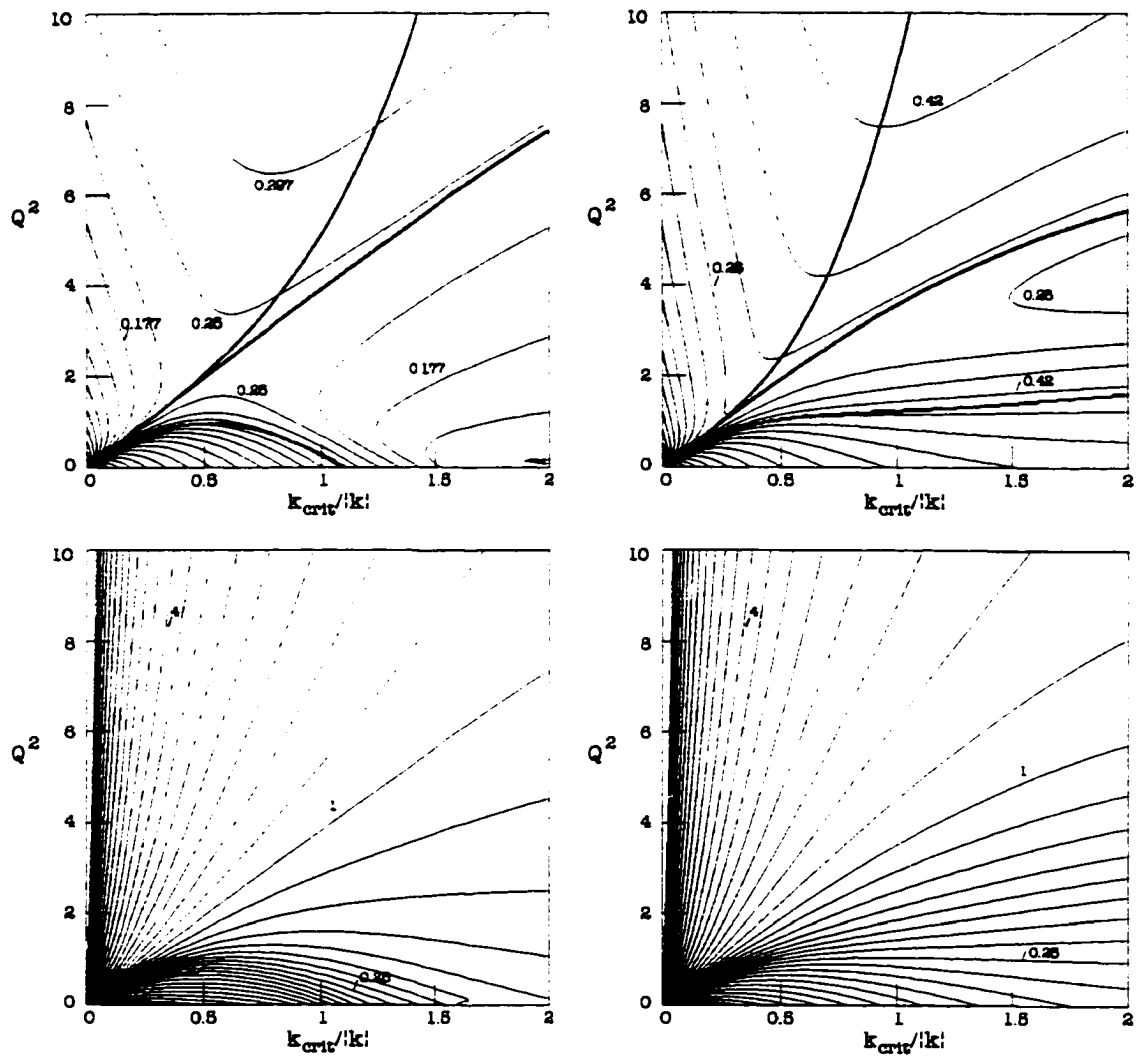


Figure 2.

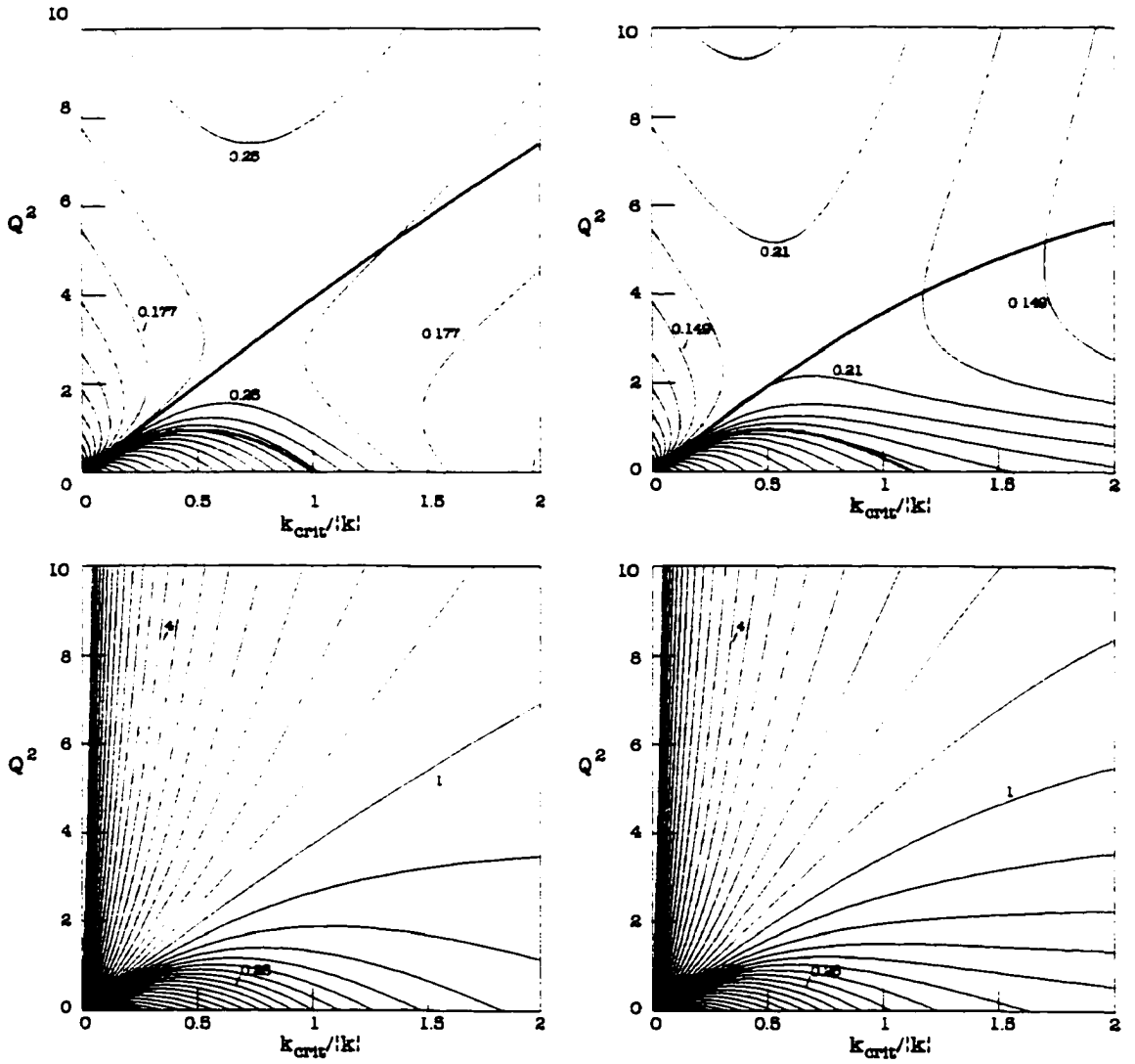


Figure 3.

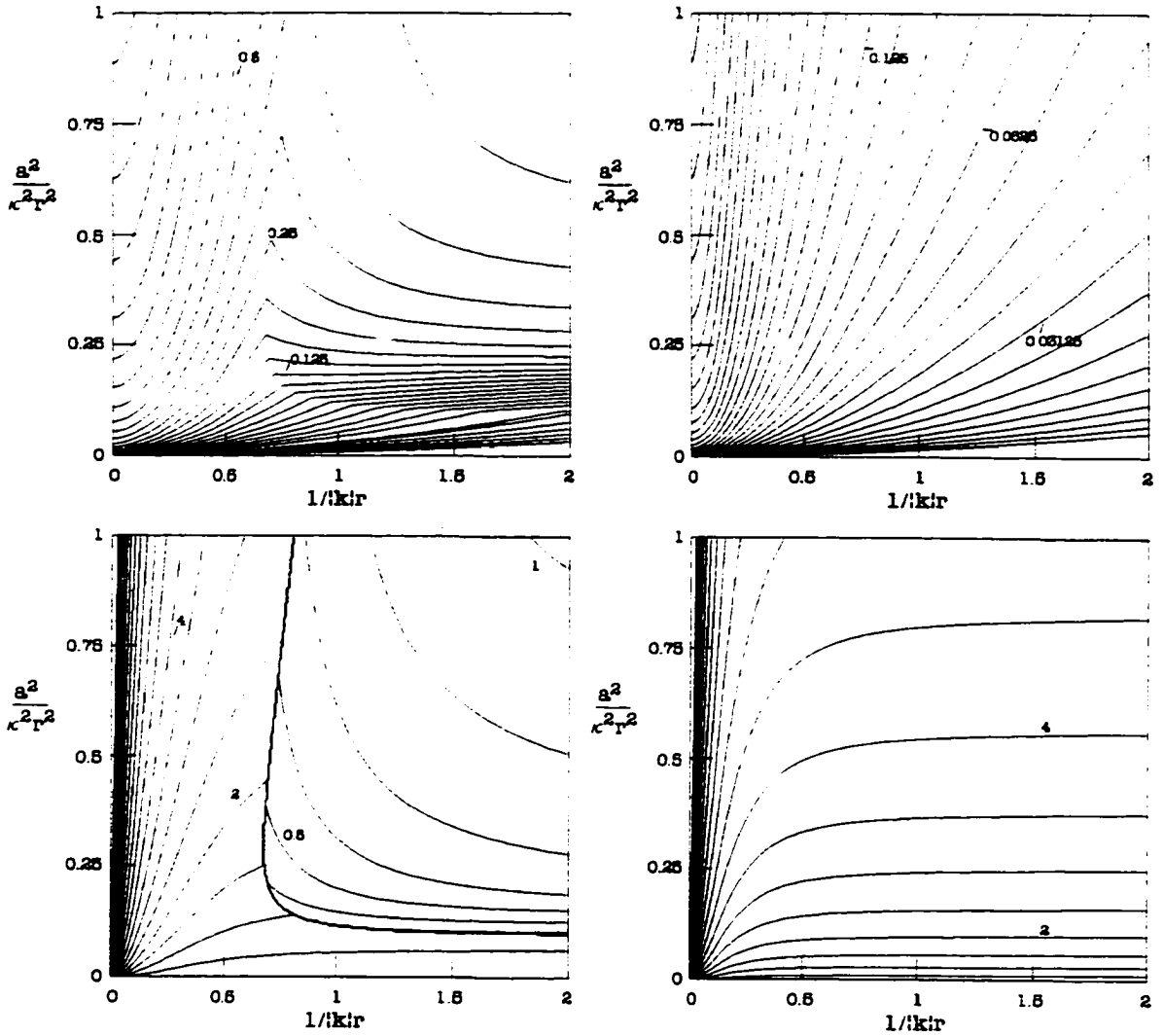


Figure 4.

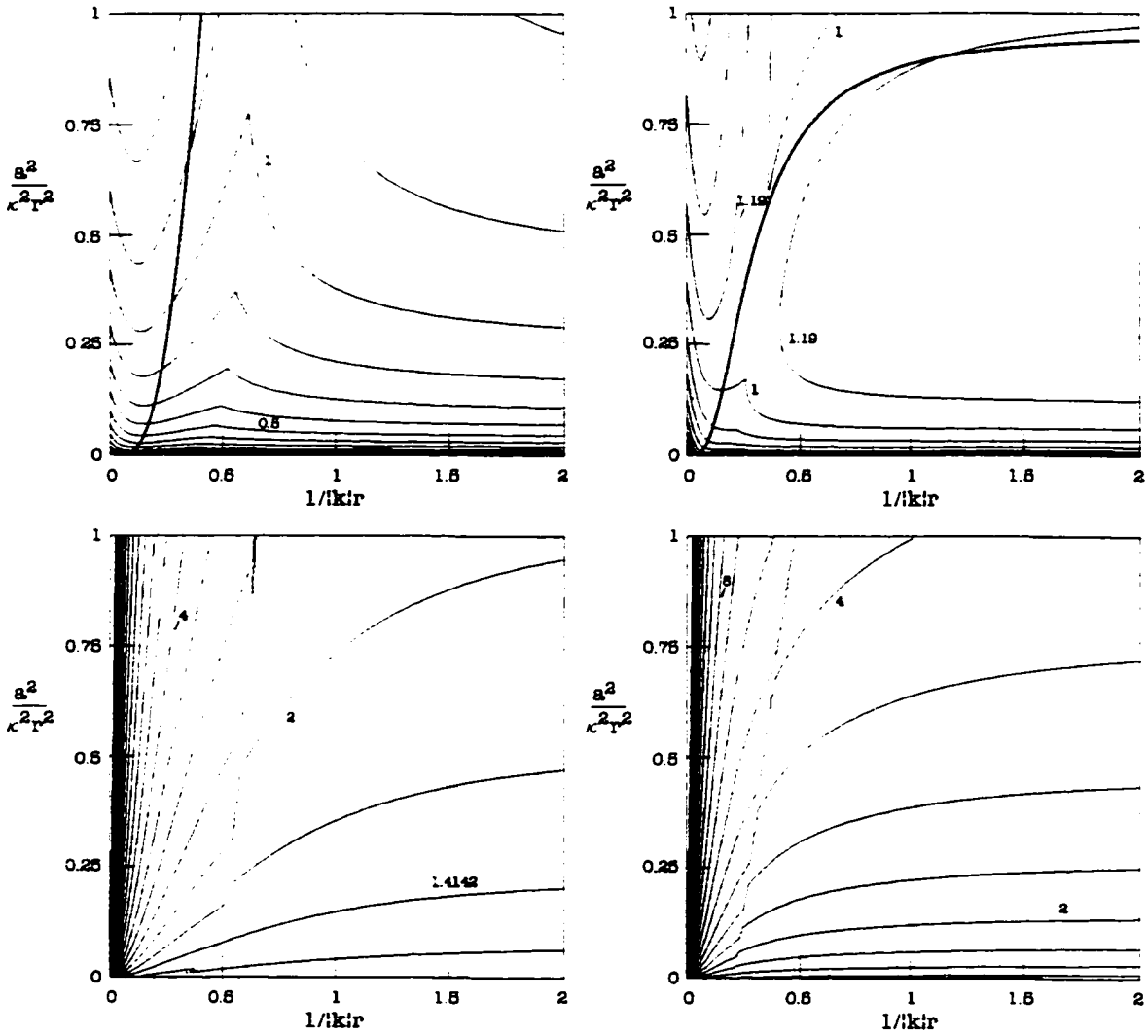


Figure 5.

# Chapter 3

# Dust Spirals and Acoustic Noise in the Nucleus of the Galaxy NGC 2207

# Dust Spirals and Acoustic Noise in the Nucleus of the Galaxy NGC 2207

B. G. Elmegreen[1], D. M. Elmegreen[2], E. Brinks[3], C. Yuan[4,5], M. Kaufman[6], M. Klarić[7], L. Montenegro[5], C. Struck[8], M. Thomasson[9]

Received _____; accepted _____

[1]IBM Research Division, T.J. Watson Research Center, P.O. Box 218, Yorktown Heights, NY 10598, USA, bge@watson.ibm.com

[2]Department of Physics and Astronomy, Vassar College, Poughkeepsie, NY 12604, elmegreen@vaxsar.vassar.edu

[3]Depto. de Astronomía, Universidad de Guanajuato, Apdo. Postal 144, Guanajuato, Gto. 36000, México, ebrinks@ coyotl.astro.ugto.mx

[4]Institute of Astronomy and Astrophysics, Academia Sinica, Nankang, Taipei, Taiwan, ROC, yuan@biaa7.biaa.sinica.edu.tw

[5]City College of New York, 138th St on Convent Ave., New York, NY 10031

[6]Department of Physics and Department of Astronomy, Ohio State University, 174 West 18th Avenue, Columbus OH 43210, rallis@mps.ohio-state.edu

[7]Midlands Technical College, Columbia, SC 29202, klaricm@mtc.mid.tec.sc.us

[8]Department of Physics and Astronomy, Iowa State University, Ames, IA 50010, curt@iastate.edu

[9]Onsala Space Observatory, S-439 92 Onsala, Sweden, magnus@oso.chalmers.se

## ABSTRACT

Observations with the Hubble Space Telescope reveal an irregular network of dust spiral arms in the nuclear region of the interacting disk galaxy NGC 2207. The spirals extend from $\sim$ 50 pc to $\sim$ 300 pc in galactocentric radius, with a projected width of $\sim$ 20 pc. Radiative transfer calculations determine the gas properties of the spirals and the inner disk, and imply a factor of $\sim$ 4 local gas compression in the spirals. The gas is not strongly self-gravitating, nor is there a nuclear bar, so the spirals could not have formed by the usual mechanisms applied to main galaxy disks. Instead, they may result from acoustic instabilities that amplify at small galactic radii. Such instabilities may promote gas accretion into the nucleus.


## 1. Introduction

Recent high resolution observations of the nuclear regions of some spiral galaxies show irregular spiral patterns in dust and gas that are not continuations of the main spiral arms or driven by obvious bars. Examples in the recent literature are NGC 278 (Phillips et al. 1996), M81 (Devereux et al. 1997), M87 (Ford et al. 1994; Dopita et al. 1997), NGC 4414 (Thornley & Mundy 1997), NGC 5188 and NGC 6810 (Carollo, Stiavelli, & Mack 1998).

This *Letter* reports similar spirals within the inner 500 pc of NGC 2207 that were found in the course of a larger program to study this galaxy and its interacting neighbor, IC 2163, with the *Hubble Space Telescope*. NGC 2207 and IC 2163 were previously observed from the ground at optical and radio (21 cm) wavelengths

(Elmegreen et al. 1995a; hereafter Paper I), and modeled by computer simulations to reproduce the peculiar morphologies, internal velocities, and orbital motions of the main galaxy disks (Elmegreen et al. 1995b).

The nuclear spirals in NGC 2207 are too small to observe by any present-day instrument other than HST, so we derive their properties and those of the nuclear disk using only the HST data, combined with radiative transfer techniques. The disk is found to be too weakly self-gravitating for the spirals to be density waves. We investigate other possible origins for the observed structure.

## 2. Observations

In May 1996, we observed the nuclear region of NGC 2207 with the refurbished Planetary Camera of the Hubble Space Telescope at 0.0455 arcsec resolution, using filters at four passbands, U, B, V, and I. A color image made from the V and I bands of a region around the nucleus is shown on the left in figure 1. The inner HI disk (Paper I) is inclined by 35° and has a major axis position angle of $\sim$ 140°; approximately the same inclination applies to the nuclear disk seen here (from the ellipticity of the intensity distribution), but the position angle is $\sim$ 189°. (Note the arrow in the bottom–left of the HST image, which indicates north.) The image on the right in figure 1 is an unsharp-masked version of the V image, which highlights the dust structure. The angular scale of the figure is 160 pixels = 7.28 arcsec on a vertical side, which is 1.24 kpc for a distance of 35 Mpc (Paper I).

Several dark dust streamers are evident in the figure. They are peculiar in several respects: (1) they have no accompanying stellar spiral arms or star formation knots (confirmed by U and B images, which are not shown here because the S/N

is lower than for the V and I images), as do dustlanes in the main disks of spiral galaxies, (2) they have much larger pitch angles ($\sim 50°$) than main-disk spirals (which have pitch angles of $\sim 15°$), (3) there are many of them, particularly in the outer parts, forming a dark pinwheel with some intersections, not just a regular 2-arm spiral as in grand-design galaxy disks, and (4) they are very short, with the shortest only several tens of parsecs long, and the longest several hundred parsecs.

The nucleus has an exponentially varying light profile near the center, as shown on the top of figure 2. The curves are intensity scans across the nucleus in V and I bands, averaged over a scan width of 5 pixels, along a strip parallel to the two arrows shown at the top of the left hand image in figure 1. There is no power-law cusp (even on single pixel-wide scans), and hence no obvious black hole that might be revealed by such a cusp (Lauer et al. 1992). This is consistent with the lack of a nuclear radio continuum source (Condon 1983; Vila et al. 1990) from an active nucleus. Neither is there a nuclear starburst (Paper I). The exponential scale length in V and I bands within 0.5 arcsec from the center is $\sim 0.47''$, or 80 pc deprojected. Just beyond this distance, the deprojected scale lengths change to 360 pc in V and 270 pc in I.

## 3. Radiative Transfer Model

In order to estimate gas densities, the dust spiral was studied using a radiative transfer model (Block et al. 1996) that was fit to an approximately EW scan positioned $1.638'' = 278$ pc north of the nucleus (see arrows, Fig. 1). The V and I-band intensity profiles along the scan are shown on the bottom of figure 2, along with the model fits (dashed lines). The model considers an inclined disk with properties that are typical for galaxies: exponential radial profiles with the same

scale lengths for the stars, gas and dust; Gaussian profiles perpendicular to the disk with a smaller scale height $h$ for the gas and dust mixture than the stars (for which $h = 100$ pc is assumed), and the same scale heights for the dark features as for the regions between them. Note that the value of the stellar scale height does not matter much as long as it is several times larger than the gaseous scale height. Four dust features with Gaussian profiles parallel to the disk cause the absorption dips seen in the scans. The fit was made to the I band because extinction is weakest there; only the ratio of extinction to gas column density was varied between V and I bands, as appropriate for these two wavelengths. Scattering is included in the models, but found to be relatively unimportant.

Some aspects of the model are uniquely specified by the data. The observed widths of the dust features have to match the projected dimensions in the models, and then the midplane densities in the dust features are determined uniquely by the line-of-sight opacities of the absorption dips. The intrinsic disk scale length in the model is also determined by the observations, but only approximately, because internal absorption flattens the disk profile (Byun, Freeman, & Kylafis 1994). As a result, the model gives the internal extinction, the gas surface density between the dust lanes, and the intrinsic disk scale length, but each are uncertain by a factor of $\sim 2$.

The radiative transfer fit in figure 2 has a V-band extinction in the midplane at the position of the strip equal to $\sim 9$ optical depths per kiloparsec between the dustlanes. This corresponds to an average hydrogen density of $\sim 6$ cm$^{-3}$ with the conventional dust-to-gas conversion factor (Bohlin, Savage & Drake 1978) and the usual assumption that gas and dust are well mixed. The perpendicular scale height of the inner disk is $\sim 35$ pc, and the intrinsic exponential scale lengths of the V

and I band emissivities are 170 pc and 220 pc (these are less than the observed scalelengths because absorption in the disk flattens the apparent intensity profile). The hydrogen densities in the four dustlanes, in order from east to west (left to right in Fig. 2), are 11, 17, 45, and 16 $cm^{-3}$, and their in-plane dimensions are $\sim$ 20, 20, 5, and 25 pc. The average ratio of the density in a dustlane to the density between the dustlanes is $\sim$ 4. Most of the projected extents of these dustlanes are from the perpendicular disk scale height. The products of the line-of-sight dustlane thicknesses and the midplane densities give effective line-of-sight V-band extinctions through the dust features of $\sim$ 1.2, 1.8, 1.2, and 2.1 optical depths, respectively. The total extinction between the dustlanes, perpendicular to the disk, is the product of twice the disk scale height and the opacity, or 0.6 optical depths in V band.

The radiative transfer solution is the only way to estimate the gas density at high resolution; the radio observations are at much lower resolution. The radiative transfer suggests that the average hydrogen column density between the dustlanes at this radius, measured perpendicular to the disk, is $\sim 1.3 \times 10^{21}$ $cm^{-2}$, which corresponds to a mass column density of 14 $M_\odot$ $pc^{-2}$ including helium. This is larger than the inclination-corrected VLA[10] measurement (Paper I) of $\sim$ 3 $M_\odot$ $pc^{-2}$ for HI, including helium, in a 13.5″ × 12″ beam centered on the nucleus. There are no direct CO observations of the nucleus, but there are two CO detections made by one of us (MT) with a 43″ beam at the Swedish-ESO Submillimetre Telescope (La Silla, Chile), centered 1/4-beam E and W of the nucleus; both detections include the nucleus in the beam pattern. The integrated CO emissions are each 6.9 K km $s^{-1}$ on the main beam temperature scale, so the inclination-corrected mass column

[10]The National Radio Astronomy Observatory (NRAO) is operated by Associated Universities, Inc., under cooperative agreement with the National Science Foundation.

density for molecular hydrogen plus helium is 29 $M_\odot$ $pc^{-2}$, assuming the standard conversion factor for CO luminosity to molecular mass (Strong et al. 1988). All of these observations suggest the nuclear disk has a relatively low gas column density, consistent with the lack of a starburst in the inner region.

## 4. Possible Origins for the Nuclear Spirals

What is the origin of the dust spirals in the nuclear disk of NGC 2207? Spirals like these are not typically present in galaxies with strong nuclear or inner ring starbursts, where the dust features are accompanied by star formation (e.g., NGC 6946 – Engelbracht et al. 1996), nor are they as symmetric as dust features in bars (e.g., NGC 4321 – Sakamoto et al. 1995; Knapen et al 1995). The nuclear dust spirals are also not likely to be related to the main spiral structures because the nuclear spirals lie inside the inner Lindblad resonance for the outer spirals (Elmegreen, Elmegreen & Montenegro 1992) and inside a Q barrier that might come from a bulge. Both of these features shield the nuclear region from incoming spiral waves (Bertin et al. 1989). The position inside the inner resonance also precludes any resonance excitation that might come from the outer spirals (Sellwood & Lin 1989; Sellwood & Kahn 1991).

This leads us to suspect that the spirals are formed and dispersed continuously in the nuclear disk. They could be strong compressions or shock fronts caused by turbulent motions that are driven by gas inflow (Struck 1997) or other irregularities in the nuclear disk, or they could result from local instabilities.

The magnetically-driven instability discussed by Balbus & Hawley (1991) is a reasonable choice, discussed already in this context by Dopita et al. (1997).

However, it might not be appropriate for low-density nuclear disks like NGC 2207 because it requires high angular shear. The disk in M87 studied by Dopita et al. surrounds a black hole and probably has the required shear, but the situation in NGC 2207 is not so clear. We would prefer an explanation for the spirals in NGC 2207 that works with little shear.

Another well-known instability produces multiple-arm spirals in the main disks of galaxies, and is driven by the gravity of the stars and gas (Lin & Shu 1964; Toomre 1981). This instability becomes strong when a dimensionless parameter $Q = \kappa a/(\pi G\sigma)$ has a value of around 2 or less (Toomre 1981), and it continues to work with small angular shear if $Q \sim 1$. Here $\kappa$ is the frequency of weak radial oscillations for slightly displaced material, $a$ is the rms velocity dispersion, $G$ is the gravitational constant, and $\sigma$ is the gas mass column density of the disk. We do not observe $a$ and $\kappa$ in the nuclear region directly because the angular scale is too small, but we can estimate them from the radiative transfer solution. We consider solid-body rotation at angular rate $\Omega$, for which $\kappa = 2\Omega$, and treat first a non-self-gravitating disk, where the scale height is $h = a/\Omega$. These combine to give $Q = 2a^2/(\pi G\sigma h)$. The radiative transfer solution gives $\sigma \sim 14$ $M_\odot$ pc$^{-2}$ and $h = 35$ pc in the vicinity of the strip. Thus $Q \sim 0.3a^2$ with $a$ in km s$^{-1}$. The VLA data (Paper I) suggest that the entire disk, including the inner portion, has a relatively large gaseous velocity dispersion, possibly in excess of 40 km s$^{-1}$. If $a$(km s$^{-1}$) $> 10$, which is likely, then $Q$ is much larger than 2, consistent with our use of $h \sim a/\Omega$. We note that this estimate for $\Omega \sim a/h \sim 0.28$ km s$^{-1}$ pc$^{-1}$ is also consistent with ground-based optical observations (Rubin et al. 1983) at 1″ resolution. This implies that even the usual expression for $Q$, which is valid for a self-gravitating disk as well, gives a large value. Setting $\Omega > 0.1$ km s$^{-1}$ pc$^{-1}$ from Rubin et al., we get $Q = \kappa a/(\pi G\sigma) > 1.1a$ for $a$ in km s$^{-1}$. This is again much larger than 2

for reasonable velocity dispersion $a$. Because of the large $Q$, the self-gravitational instability that drives spirals in the main disks of galaxies cannot operate in the nuclear disk of NGC 2207.

If self-gravity cannot generate the spirals, then another local source must be present. An intriguing possibility is the natural tendency for sound waves to amplify at small galactocentric radii (Montenegro 1998; Montenegro, Yuan & Elmegreen 1998). Consider a disk in rigid rotation with constant surface density (exponential variations in $\sigma$ and $a$ and radial variations in $\Omega$ do not affect the results significantly). The governing equation for a wave-like perturbation in column density, $\sigma_1 \sim h_1 e^{i(\omega t - m\theta)}$, is

$$\frac{d^2 h_1}{dr^2} + \frac{1}{r}\frac{dh_1}{dr} + (\frac{\kappa^2}{a^2}(\nu^2 - 1) - \frac{m^2}{r^2})h_1 = 0.$$

Here $\nu \equiv (\omega - m\Omega)/\kappa$, $m$ is the azimuthal wavenumber, $r$ is the galactocentric radius, and $\Omega$, $\kappa$, and $a$ were defined above. When

$$\frac{\kappa^2}{a^2}(\nu^2 - 1) \equiv \alpha^2 > 0,$$

the solutions are Bessel functions $J_m(\alpha r)$ and $Y_m(\alpha r)$; $Y_m$ diverges at small $\alpha r$. For $\alpha r \sim \kappa r/a$ large, $J_m$ and $Y_m$ combine to give outgoing and incoming sonic waves. In NGC 2207, there is little activity in the nucleus; the waves generated locally are probably moving in both directions. Those that propagate outward become weaker by geometric effects (amplitude $\propto r^{-1/2}$) and viscous damping. Those that propagate inward amplify as $Y$ diverges; then they dissipate by shocks when r approaches the center near $r = m/\alpha \sim ma/\kappa$. At this radius, the separation between waves equals the minimum possible distance, which is the radius of epicyclic motion at the sound speed. Thus waves with high $m$ occupy mostly the outer regions of the nuclear disk. This result is in agreement with the observations in figure 1: there are many more dust features in an annulus at large radius than at small radius.

The waves also propagate in the azimuthal direction with angular speed $\omega/m$, as long as $\nu^2 - 1 > 0$. Waves with different $m$ therefore interact to form complex structures and intersections, as seen in NGC 2207. The waves may also become sheared by slight differential rotation to form open trailing spirals, although shear is not required to make the gas unstable.

The above solutions assume the frequency $\omega$ is real and the radial wavenumber, $k \equiv -id(\text{phase})/dr$, is complex. We can assume alternatively that $k$ is real and $\omega$ is complex, in which case the waves, fixed in space, grow in time. The result (Montenegro et al. 1998) is a growth time for the waves equal to the propagation time, $r/a$, and because $r/h \sim r\Omega/a \sim 6$ in the part of NGC 2207 considered here, this is also about the orbit time. After this time, the waves shock and dissipate, as in the solution $Y$ above.

These properties of sonic noise at small galactocentric radii should be appropriate for a nuclear galactic disk that is not dominated by a strong bar, black hole, or starburst. They agree well with the characteristics of the dust features observed at the center of NGC 2207. Acoustic spirals have not been considered for galaxies before because the main disks typically have sound speeds much less than orbit speeds, and they also have much stronger self-gravity. Nevertheless, acoustic spirals may be an important agent for driving gas accretion in some nuclei.

The accretion rate from acoustic spirals may be estimated from the energy dissipation rate. If the waves become mild shocks, then the energy flux into each shock is $\sim 1.5\rho a^3$, and the total shock dissipation rate is $\sim 1.5\rho a^3 \times 2h \times mL$ for number of arms $m$ and arm length $L$. Dividing this by the orbital energy available, which is $\sim 0.5\rho v^2 \times 2h \times \pi r^2$ for orbit speed $v$, the loss rate becomes several times $a^3 m/(v^2 r)$, considering that $L \sim r$. Now we can use $r \sim ma/\kappa$ to describe the radius

of wave shocking, from the Bessel function solution above, and then the overall evolution rate is $\sim \kappa(a/v)^2$. The mass accretion time is therefore comparable to the orbit time multiplied by the square of the ratio of the orbit speed to the sound speed. In nuclear regions like this, the orbit speed may be only only a few times the sound speed, and then the gas accretion time can be relatively short. Presumably there is self-regulation, however, because persistent shocking in acoustic waves might heat the gas to the point where shocks no longer appear. Then the accretion process would slow down until the gas cools again. The overall impact of acoustic waves on accretion is therefore difficult to assess.

## 5. Summary

NGC 2207 contains peculiar dust spiral arms in its nuclear disk that are not obviously related to star formation, bar structure, or gravity-driven spiral density waves. They could be regions of forced compression that are stirred, for example, by inflow, but they could also be amplified acoustic waves, which tend to drive spiral structure at small relative radii (i.e., $r\kappa/a$ not much larger than 1). The resulting spiral arms steepen and shock in an orbit time, which is only $\sim 2 \times 10^7$ years in the region studied, and this shocking ultimately causes the gas to lose angular momentum and energy. Then it can accrete to the nucleus.

Acoustic spirals may be the primary agent for gas accretion in the most quiescent nuclear disks, i.e., those with weak self-gravity and bar forcing, limited access to outer disk activity, and little shear. It may also be an important supplement to other accretion processes, such as bar-driven shocks and the Balbus & Hawley (1991) instability, in more active regions. A more quantitative assessment of its role in general nuclear environments is difficult to make at the present time.

Support for this work was provided by NASA through grant number GO-06483-95A from the Space Telescope Science Institute, which is operated by the Association of Universities for Research in Astronomy, Inc., under NASA contract NAS5-26555. Figure 1 was made using the IBM Data Explorer software, with the help of Dr. Tom Jackman.

## REFERENCES

Bertin G., Lin C.C., Lowe S.A. & Thurstans R.P. 1989, ApJ, 338, 78

Balbus, S.A., & Hawley, J.F. 1991, ApJ, 376, 214

Block, D.L., Elmegreen, B.G. & Wainscoat, R.J. 1996, Nature, 381, 674

Bohlin, R.C., Savage, B.D. & Drake, J.F. 1978, ApJ, 224, 132

Byun, Y.I., Freeman, K.C., & Kylafis, N.D. 1994, ApJ, 432, 114

Carollo, C.M., Stiavelli, M., & Mack, J. 1998, AJ, in press

Condon, J.J. 1983, ApJS, 53, 459

Devereux, N., Ford, H. & Jacoby, G. 1997, ApJ, 481, L71

Dopita, M.A., Koratkar, A.P., Allen, M.G., Tsvetanov, Z.I., Ford, H.C., Bicknell, G.V., & Sutherland, R.S. 1997, ApJ, 490, 202

Elmegreen, B.G., Elmegreen, D.M. & Montenegro, L. 1992, ApJS, 79, 37

Elmegreen, D.M., Kaufman, M., Brinks, E., Elmegreen, B.G. & Sundin, M. 1995a ApJ, 453, 100

Elmegreen, B.G., Sundin, M., Kaufman, M., Brinks, E. & Elmegreen, D.M. 1995b, ApJ, 453, 139

Engelbracht, C.W., Rieke, M.J., Rieke, G.H., & Latter, W.B. 1996, ApJ, 467, 227

Ford, H.C., et al. 1994, ApJ, 435, L27

Knapen, J.H., Beckman, J.E., Heller, C.H., Shlosman, I., & de Jong, R.S. 1995, ApJ, 454, 623

Lauer, T.R., et al. 1992, AJ, 103, 703

Lin, C.C., & Shu, F.H. 1964, ApJ, 140, 646

Montenegro, L. 1998, PhD Dissertation, City College of New York

Montenegro, L., Yuan, C., & Elmegreen, B.G. 1998, submitted to ApJ.

Phillips, A.C., Illingworth, G.D., MacKenty, J.W. & Franx, M., 1996, AJ, 111, 1566

Rubin, V.C. & Ford, W.K., Jr. 1983, ApJ, 271, 556

Sakamoto, K., Okumura, S., Minezaki, T., Kobayashi, Y., & Wada, K. 1995, AJ, 110, 2075

Sellwood, J.A. & Lin, D.N.C. 1989, MNRAS, 240, 991

Sellwood, J.A. & Kahn, F.D. 1991, MNRAS, 250, 278

Strong, A.W. et al. 1988, A&A, 207 1

Struck, C. 1997, ApJS, 113, 269

Thornley, M.D., & Mundy, L.G. 1997, ApJ, 490, 682

Toomre, A. 1981, in The Structure and Evolution of Normal Galaxies, ed. S.M. Fall & D. Lynden-Bell, Cambridge: Cambridge Univ. Press, p. 111

Vila, M.B., Pedlar, A., Davies, R.D., Hummel, E. & Axon, D.J. 1990, MNRAS, 242, 379

---

This manuscript was prepared with the AAS LaTeX macros v4.0.

Fig. 1.— (left) Hubble Space Telescope image of the nuclear region of NGC 2207 in color rgb format, with r taken to be the I-band image, b the V-band image, and g the average of these two images. Arrows at the top indicate the strip used to fit the radiative transfer model. North is indicated by the arrow in the lower right. (right) Unsharp-masked image of the V-band showing intricate dust structure as dark bands. The unsharp mask was made by subtracting the convolution of the V image with a Gaussian of 0.5 arcsec FWHM from the original V image.

Fig. 2.— (top) Intensity profiles in V and I bands along a strip 5 pixels (= 0.228″) wide through the nucleus, parallel to the strip used for the radiative transfer model, shown by the arrows in figure 1. (bottom) Intensity profiles in V and I bands through a strip north of the nucleus, and radiative transfer fits (dashed lines) to these profiles.

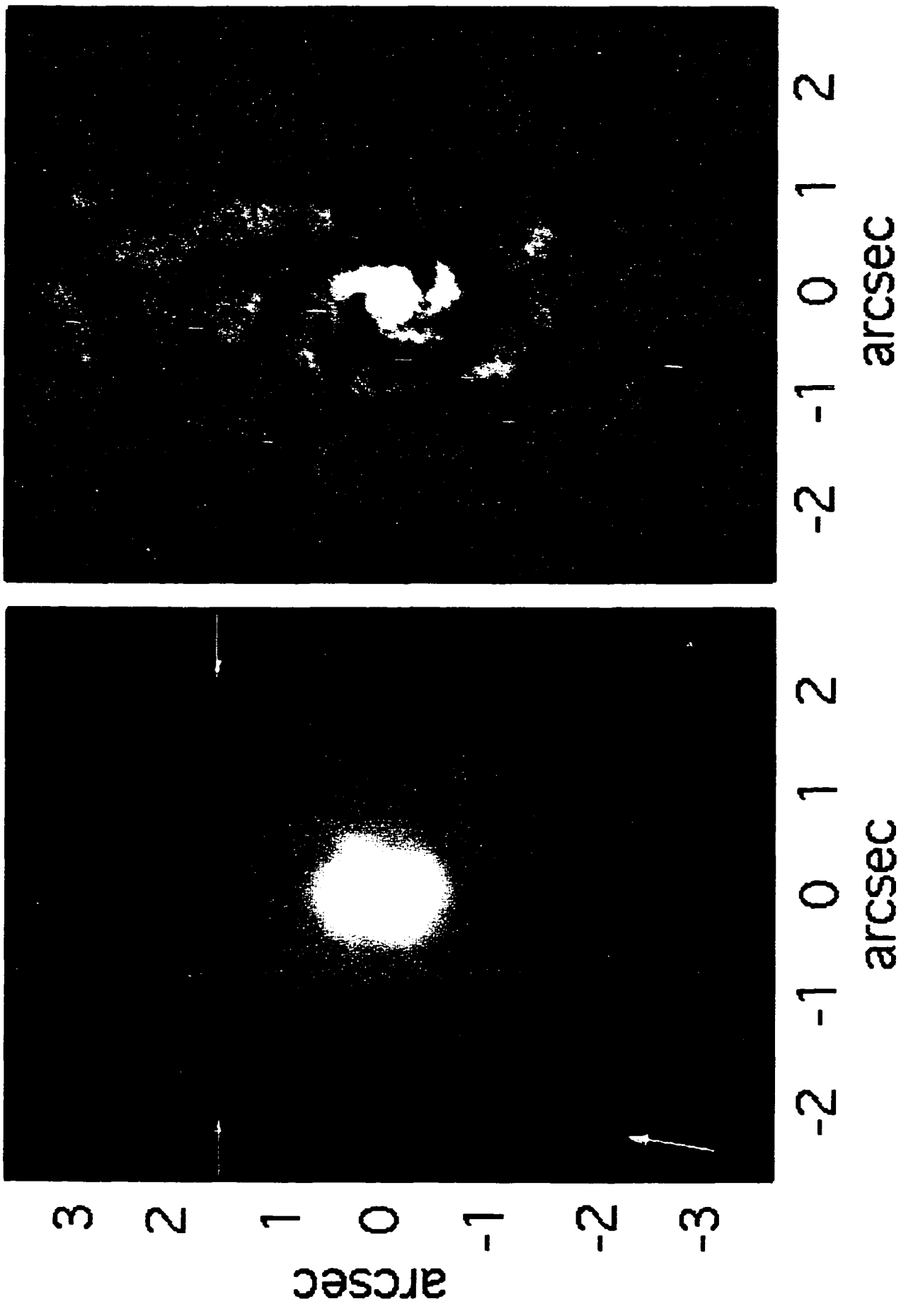


bge Host: bge2.watson.ibm.com Job: n2207fig1.ps Date: 7/9/1998 Time: 17:20 Queue: W12120AQ Printer: W12120AQ

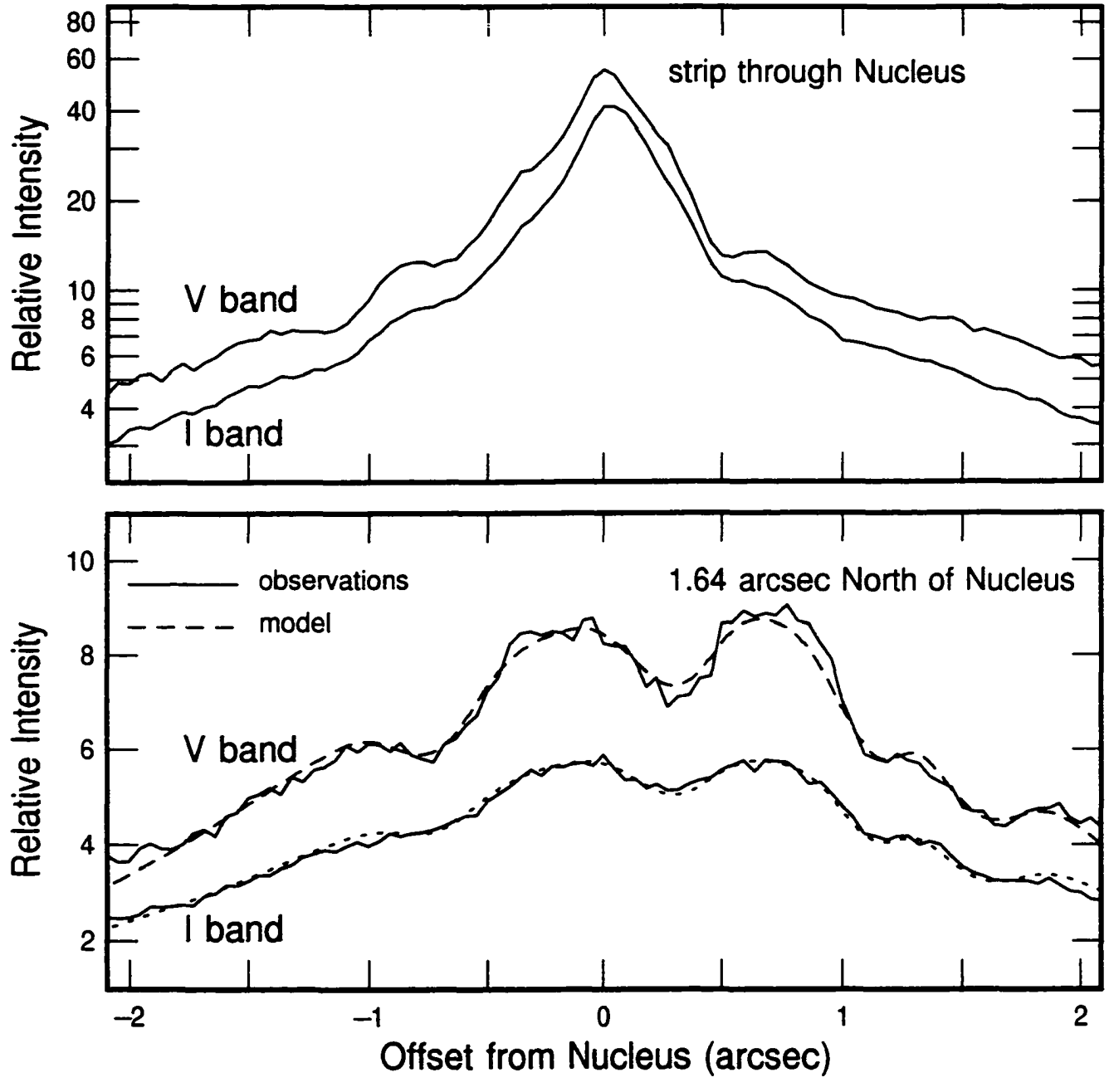

# Chapter 4

# Hidden Three-Armed Spirals in a Sample of 18 Galaxies

# Optical Tracers of Spiral Wave Resonances in Galaxies: II. Hidden Three-Arm Spirals in a Sample of 18 Galaxies

Bruce G. Elmegreen

IBM Research Division, T.J. Watson Research Center Yorktown Heights, NY 10598

Debra Meloy Elmegreen

Vassar College Observatory, Poughkeepsie, NY 12602

and

Luis E. Montenegro

City College of New York, 138th St on Convent Ave., New York, NY 10031

Received _____; accepted _____

## ABSTRACT

Computer enhanced galaxy images reveal underlying spiral structures with three symmetric arms that extend between $\sim$ 25% and $\sim$ 85% of the outer radii of the two-arm spirals. Many of the galaxies containing multiple arms or other complex spirals are clear superpositions of simple two- and three-arm structures. The three-arm spirals appear to extend exactly from the inner to the outer 3:1 resonances in most cases, and the more prominent two-arm spirals begin outside the inner 2:1 resonance and extend to the outer 2:1 resonance. Evidence for the corotation radius is clear in the gas-rich galaxies, in the form of sharp endpoints to star formation ridges and dust lanes in the two-arm spirals. The inner 4:1 resonance is also evident in some cases as a pair of spurs exactly midway between the main spiral arms and diametrically opposite to each other in the galaxy. All of these resonance fits are in near perfect agreement with the ratios of resonance radii determined theoretically from rotation curves for each galaxy, and so they define the spiral pattern speed for each galaxy with some redundancy. The pattern speeds for the m=2 and m=3 spirals are the same to within 10%.

We interpret these results to imply that most of the two-arm spirals are self-sustaining wave modes with inner wave reflections from bars inside corotation or evanescent regions where the non-barred spirals wrap into a circle. The asymmetry in the main spirals produces an m=1 component which beats with the m=2 component to drive the observed m=3 spiral exactly between its absorbing resonance limits. In this interpretation, the three-arm spirals are not independent wave modes with their own amplifiers and reflective barriers, but are instead driven waves and a likely source of

energy loss from the two-arm mode. The observation of relatively weak three-arm spirals in the interacting galaxies NGC 5194 (M51) and NGC 3031 (M81) implies that three-arm spirals in general may take several revolutions to build up once an asymmetric two arm spiral appears. In that case, tidal interactions may first stimulate a two arm mode, forming a grand design spiral when the companion is still close, but in time the morphology should change to a multiple arm or irregular-looking galaxy because of the increasing contribution from the three arm component.

## 1. Introduction

The optical appearance of most spiral galaxies is dominated by the brightest spiral arms, which are often symmetric about the nucleus in the inner regions. When this symmetry extends throughout the whole disk, the arms give the appearance of a "grand design," as modeled by Lin and collaborators with wave modes (Bertin et al. 1989), and by Toomre (1981), Hernquist (1990) and others with tidal interactions. When the arms are not symmetric in the outer parts, they often have a "multiple arm" or "flocculent" structure, depending qualitatively on the number, length, and inner symmetry of the arms (Elmegreen and Elmegreen 1989). Typically both multiple arm and grand design galaxies contain stellar density waves, as shown by the similarity between their B and I band images, while flocculent galaxies contain mostly star formation features (Elmegreen and Elmegreen 1984;1985; hereafter EE84, EE85).

The physical differences between these types of spirals are thought to be related to the distributions of mass and velocity dispersion in the disk and halo and to the presence or lack of a wave-reflecting inner barrier from a bulge or a bar (see

reviews in Bertin 1991, Elmegreen 1991). Some of these differences show up in the rotation curves (Fridman et al. 1987; Elmegreen and Elmegreen 1990b; Biviano et al. 1991). Although no real galactic spiral has yet been fitted by a theoretical model, computer simulations can reproduce the general forms of these three types of structures reasonably well (e.g., see Thomasson, et al. 1990; Carlberg and Freedman 1985; Elmegreen and Thomasson 1993, respectively).

Unfortunately, most of what we know about the morphology of spiral structure comes from visual impressions of blue photographic images, which are usually dominated by the brightest arms. Morphological classification systems therefore emphasize only the qualities most visible to the eye, such as spiral arm pitch angle (Hubble 1926), arm continuity and thickness (van den Bergh 1960) or continuity and symmetry (Elmegreen and Elmegreen 1989), and the spiral- or ring-like approach to the nucleus (de Vaucouleurs 1963). But real spirals are usually more complicated than these classification systems suggest. Dust clouds and star formation make spiral arms patchy and unevenly thick, non-linear processes in the stellar and gas waves make spurs (Shu et al. 1973) and excite more waves at resonances (Taggar et al. 1987), and independent wave patterns may coexist (Lin and Lowe 1990). One of the goals of computer enhanced imagery is to unravel this complexity in an objective way.

Fourier transforms of galaxy images can reveal more about spiral structure than simple visual inspection (Krakow et al. 1982; Iye et al. 1982; Considère & Athanassoula 1988) but the high order components that are found by Fourier analysis can sometimes be ambiguous. For example, the presence of a strong m=4 component in the Fourier transform of a galaxy image (in this paper $m$ refers to azimuthal variations of the form $e^{im\theta}$ for azimuthal angle $\theta$) does not guarantee that there is

an underlying four-arm structure; usually there is not. Strong m=4 components are usually caused by non-linear two-arm spirals that have wide interarm valleys and narrow arm crests. Such non-linearity is common because the arm/interarm contrasts in the blue and near-infrared typically exceed 3, and then the azimuthal profiles of spiral arm intensity, which appear peaked or sinusoidal when plotted as a surface brightness (i.e., log intensity; see Schweizer 1976; Strom, Jensen, and Strom 1976; EE84, EE85), have wide interarm valleys and narrow arm crests. The Fourier m=3 component can also give a false impression that there is a three-arm spiral when there is none. For example, the intensity from a pure two-arm spiral may be modulated by interarm star formation or by an intensity gradient from one side of the galaxy to the other (from internal extinction and inclination effects); then an m=3 component can appear as a beat frequency. Such ambiguities can always be resolved if the Fourier components are summed, but when the arms are typically non-linear, the number of terms in the sum must be large to avoid artificial ringing and false interarm features. Foreground stars are also a problem for Fourier analysis.

This paper introduces a better computer algorithm for extracting various types of symmetries from galaxy images. It preserves the non-linear shapes of the spiral arms without introducing false interarm components, and it displays the m=2,3,4, etc. subcomponents in whole galaxies all at once to avoid confusion with localized star formation and foreground stars. The algorithm is applied to 18 galaxies with various types of spirals. Conventional Fourier transform techniques are also used to study the arm structures. We find that underlying three-arm spirals are common in our sample and that a few galaxies have a complex four-arm or five-arm system too. To check whether this structure is sensible, we compare the termination radii of the two, three, and four arm spirals to the corresponding resonance radii predicted from theory. We find that the symmetric components in nearly all of the galaxies end at

their outer wave-epicycle resonances, i.e., where $\Omega + \kappa/m = \Omega_p$ for angular rotation rate $\Omega$, epicyclic frequency $\kappa$, and pattern speed $\Omega_p$, and that this pattern speed is about the same for $m = 2$ and $m = 3$ systems.

The symmetric images for the various components are remarkable even by themselves. Most of the galaxies in our sample show a substantial amount of two- and three-fold symmetry, not only in the overall spiral patterns, but also in the spurs, kinks, bifurcations, and termination points of the individual arms. Asymmetric images (equal to the difference between the original image and the symmetric image) also show interesting structures, mostly from star formation. The one-arm components of the spirals are best seen on these asymmetric images. Unwrapped spiral images, in which the logarithm of the radius is plotted versus the azimuthal angle, are presented as well, one for each of the symmetric and asymmetric images. These unwrapped images are useful for examining the continuity, pitch angles, and lengths of the arms and the relative azimuthal angles of the interarm features. Ultraharmonic resonance spurs, for example, occur midway in angle between the main spiral arms (Elmegreen, Elmegreen and Seiden 1989; hereafter EES); this is difficult to see on sky images of the galaxies but immediately obvious in $(\log R, \theta)$ coordinates.

## 2. Making Symmetric Images

Blue band images of the galaxies in Table 1 (from Elmegreen 1981) were digitized and calibrated with a microdensitometer (cf. Angilello et al. 1984; EE84, EE85). The images were then rectified, enhanced, and made symmetric in order to study the spiral structure.

The rectification to a face-on aspect was done by stretching pixels along the minor axis by a factor equal to the inverse cosine of the inclination angle, from de Vaucouleurs, de Vaucouleurs and Corwin (1976). The largest inclinations were for NGC 598 (55 deg), NGC 3031 (58 deg) and NGC 5055 (56 deg), which are small enough to cause no severe distortions of the spiral arms. The foreground stars and galactic bulges may appear distorted into ovals, however. North is approximately up in all images, although after deprojection the sky coordinates are not rectilinear.

The enhancement was done in two steps: first, by subtracting the mean radial light profile, as determined from a running boxcar average over a number of pixels equal to $R_{25}/4$, and then by normalizing the rms variation of the intensity at each radius to a constant value throughout the image. Here $R_{25}$ is the radius at a surface brightness of $25 mag\, arcsec^{-2}$ (from $D_{25}$ in de Vaucouleurs, de Vaucouleurs and Corwin 1976). The purpose of normalizing the rms variation with azimuth is to enhance the features in the inner part of the galaxy, where the arm-interarm contrast tends to be small. The resulting rectified and enhanced images are shown in the upper left panels of Figures 1a-r (Plates 0000-0000). They will be called *sky-enhanced* images. The white parts of the calibration bars on the right have a length equal to $R_{25}$ given in Table 1, and the calibration bars on the left represent 100 pixels.

The symmetric parts of the galaxies were illustrated by making images from successive rotations and subtractions, using the IBM IAX image processing software package. The two-fold symmetric part of a galaxy (designated the $S_2$ image) was made from the original image $I$ by the operation

$$S_2(r,\theta) = I(r,\theta) - [I(r,\theta) - I(r,\theta+\pi)]_T \qquad (4.1)$$

where the subscript T stands for truncation, meaning that pixels with negative

intensities are set to 0. The results are displayed in the middle and lower left panels of Figures 1. With this definition, the $S_2$ image consists of all bright features in the original image that have equally bright features diametrically across the galaxy. This procedure highlights symmetric *emission* such as spiral arm spurs, star formation regions, and so on, but it introduces spurious absorption features. For example, if there is a dust lane in only one arm, then only the bright part of that arm will appear in both arms of the $S_2$ image; this gives the false impression that there is a dust lane in the other arm too.

The features in a galaxy that are not present in the $S_2$ images are shown in the middle right panels of Figure 1. These asymmetric images (hereafter $A_2$) were made from the formula

$$A_2(r,\theta) = I(r,\theta) - S_2(r,\theta). \tag{4.2}$$

The $A_2$ image tends to show star formation and irregularities in the spiral structure in addition to some of the one-arm and three-arm structure.

Three-fold symmetric images ($S_3$) are shown in the top and lower right panels of Figures 1. They were obtained from the equation

$$S_3(r,\theta) = 2I(r,\theta) - [I(r,\theta) - I(r,\theta + 2\pi/3)]_T - [I(r,\theta) - I(r,\theta - 2\pi/3)]_T . \tag{4.3}$$

According to this equation, features that occur on only two of the three sides of an equilateral triangle are half as bright as features that occur on all three sides. Thus, the $S_3$ images are not perfectly symmetric, but have a gray scale representation of three-fold symmetries, with the most symmetric parts being brightest.

In a fifth type of image enhancement, the spiral arms were unwrapped by plotting the images in coordinates where the azimuthal angle, $\theta$, is the abscissa, and the logarithm of the radius, $R$, is the ordinate (Elmegreen 1985, EES; see also Iye

et al. 1982). The azimuthal coordinate ranges from 0 to $4\pi$, with tic marks at $\pi$, $2\pi$, and $3\pi$, and is measured counterclockwise from the northernmost major axis. In most cases, the radial coordinate ranges from $0.08R_{25}$ to $1.2R_{25}$, with tic marks every $0.1R_{25}$. Spirals wrapped in the sense of the letter z (s) have arms which slant from the lower left (right) to the upper right (left). As with the enhanced images discussed above, the $(\log R, \theta)$ images have their average radial profiles subtracted and the residuals normalized to a constant rms; but here, the radial average is determined pixel-by-pixel rather than from a boxcar average. As a result of the rms normalization, radii at which there are single bright features such as foreground stars or bright HII regions have diminished contrast elsewhere.

Figure 2 shows $(\log R, \theta)$ images for each of the four types of images in Figure 1, in the same order on the page (i.e., sky-enhanced - top left, $S_3$ - top right, $S_2$ - bottom left, and $A_2$ - bottom right). The straightness of the arms on these diagrams demonstrates the approximate logarithmic nature of the spirals (Danver 1942; Kennicutt 1981); the average slope of the arms is proportional to the tangent of the pitch angle. The $(\log R, \theta)$ diagrams are convenient for identifying and measuring features that are important for linking spiral structure theory to observations. For example, on the $(\log R, \theta)$ diagram of NGC 4321 the spurs at a radius of $0.4R_{25}$ are readily seen to be at an azimuthal angle exactly midway between the main arms. This location of the spurs is consistent with their interpretation as tracers of the 4:1 resonances (EES).

# 3. Resonance Radii from Two and Three Arm Structures

## 3.1. Theoretical Ratios of Resonance Radii

Figure 1 shows that even the most symmetric-looking two-arm galaxies, such as NGC 4321, can have a substantial amount of three-fold symmetry that is not apparent in conventional photographs. The less symmetric two-arm galaxies, such as NGC 628, and many multiple arm galaxies, such as NGC 5457, NGC 6946, and NGC 1232, also have prominent three-fold symmetry. We show here that this three-fold structure usually extends exactly between the inner and outer 3:1 wave-epicycle resonances for approximately the same pattern speed as the two-arm spiral.

This result complements our earlier conclusion (EES, Elmegreen and Elmegreen 1990a; hereafter EE90) that the termination radii for two-arm spirals in NGC 3031, NGC 4321, NGC 5194, and NGC 1566 are at the outer 2:1 resonances (outer Lindblad resonances, hereafter OLR). This identification was shown to be consistent with many other resonance indicators for these relatively simple galaxies, given their rotation curves. These other resonance indicators are interarm spurs at the inner 4:1 resonance, termination points of the bright star formation ridges at the corotation resonance and circles of star formation around the galaxy at this resonance, and inner spiral arm kinks and bar-to-spiral transition points at the inner Lindblad resonance. The stellar spirals were also found to have inner limits outside their inner Lindblad resonances unless there is a small bar in the nuclear region, in which case the ILR is near the end of the bar. When there is no bar, the stellar spirals wrap into a circle in the inner regions, presumably as a result of wave reflection. The gas spirals were found to penetrate this circle. We also found evidence for the theoretically predicted leading spiral that reflects back to corotation as part of the amplification cycle for the main two-arm trailing spiral pattern in M81 (see Figures

1 and 2 in Elmegreen 1991). These results are all consistent with the linear density wave and modal theories, which have long postulated that most m=2 stellar spirals should end at the OLR (Lin and Shu 1967) and reflect in the inner regions, and they are consistent with the results of a numerical simulation of a standing wave mode (Thomasson et al. 1990) which found the same resonance features. Athanassoula et al. 1987) also suggested that some galaxies have spirals that end at the OLR, although in their study, several others ended at corotation too. However, Patsis et al. (1991) put the inner 4:1 resonances at the ends of the spirals, which differs substantially from our conclusions.

The present study is designed to expose the normally hidden $m = 3$ spirals so that the same type of resonance analysis can be applied to them as for the $m = 2$ spirals. We show here that most of the spirals in our sample, even those which look very complex in conventional photographs, can be separated into two separate spiral systems that are each relatively simple, consisting of two and three-arm structures that lie between their respective resonance radii. Section 3.2 considers this separation, one galaxy at a time, building up from simple cases to the most complex. We use figures 1 and 2 for the measurements (along with atlas photographs when available), and illustrate the results with circles at the resonance radii in the bottom $S_2$ and $S_3$ images in Figure 1.

An important tool in this procedure is the theoretical ratio of resonance radii for a rotation curve that is locally of the form $V(R) \propto R^{\alpha}$. This ratio is

$$\frac{R_{res}}{R_{CR}} = \left( \frac{1-2}{m\left[\frac{1+alpha}{2}\right]^{1/2}} \right)^{1/(1-\alpha)} \tag{4.4}$$

where $m = 2$ at the inner Lindblad resonance, -2 at the outer Lindblad resonance, 3 and -3 at the inner and outer 3:1 resonances, and so on. To determine $\alpha$ for galaxies

without rotation curves, or for galaxies with large spiral arm streaming motions in their rotation curves, we use the rotation curve fits in Persic and Salucci (1991) and convert their slopes $\Delta$ into powers $\alpha$ using the interpolation formula

$$\alpha = \frac{\log\left(\frac{2.2+\Delta}{2.2-1.2\Delta}\right)}{\log 3.2}. \tag{4.5}$$

The values of $\Delta$ come from Table 1 in Persic and Salucci (1991) when the particular galaxy was observed by them, and they come from their equation (2) when it was not, i.e., from $\Delta = 0.12 + 0.096(M_B + 21.5)$ for absolute magnitudes $M_B$ from Sandage and Tammann (1981), who use a Hubble constant of 50 $kms^{-1}Mpc^{-1}$, the same as Persic and Salucci (1991). (Our overall results are independent of the Hubble constant because the slope of a rotation curve is independent of this quantity, but the conversion of absolute magnitude into $\Delta$ for our study should use the same Hubble constant that was used to calibrate this empirical relation from the observed rotation curves.) For M81 and M51 we take $\alpha = -0.2$ and $-0.16$ from rotation curves in Visser (1980) and Tully (1974). According to Persic and Salucci (1991), their expression for rotation curves is valid for galactocentric radii between about $0.3R_{25}$ and $R_{25}$, which includes approximately the inner and outer 3:1 and 4:1 resonances, corotation and the outer Lindblad resonance. The power law expression used here should be valid over the same radial range, possibly longer. Table 1 gives the galaxy parameters used to determine $\alpha$ and Table 2 gives various useful ratios of resonance radii determined from equation (4).

### 3.2. Comments on Each Galaxy

The galaxies in our sample are described here individually in order of increasing complexity. The observed radii for particular spiral arm features are measured from Figures 1 and 2 and from atlas photographs, always in units of $R_{25}$ The types of

features we look for are endpoints of spiral arms, star formation ridges and dust lanes, and interarm spurs. Ratios of the observed radii are then compared to the theoretical ratios of resonance radii given in Table 2. For each galaxy, we seek the unique pattern of radii for specific resonance features that matches the theoretically predicted pattern of radii for the rotation curve of that galaxy. When such a pattern of radii is found for a large number of features, then the spiral resonances associated with those features would seem to be correct and the pattern speed uniquely determined. If only a small number of features can be found, then some ambiguity remains. Typically four or five resonance features can be found for each galaxy.

The circles on the $S_2$ images in Figure 1 show our solutions for the radii of the inner 4:1, corotation, and outer Lindblad resonances, in order of increasing radius. The circles on the $S_3$ images show the inner and outer 3:1 resonance radii. These circles have radii that are uniquely related by the ratios in Table 2; once any one resonance is located, the other four are determined only from the tabulated ratios. Table 3 summarizes the radii of the circles in Figure 1.

The order of the galaxies in the following discussion is determined by their structure, rather than NGC number. The first two galaxies, NGC 613 and 5457, are clearly separated into two spiral arm systems with well-defined and thin arms in each system. The next three galaxies, NGC 4321, 5248, and 628, have thin two-arm spirals and thick three-arm spirals that are well defined, and the next four, NGC 6946, NGC 598, IC 342, and NGC 1232, have relatively thick and patchy spirals in both the two- and three-arm components. NGC 1232 also has a small two-arm spiral in the nuclear region which we propose is excited by a resonance interaction with the spiral in the outer galaxy. Next in order are NGC 4254 and 6912, which are dominated by the three-arm component, and NGC 1300 and 157, which are barred

galaxies with only triangles in their $S_3$ images. Then there are three galaxies with somewhat flocculent features, NGC 3938, 7793, and 5055; the first of these may have a regular five or six arm spiral, while the others appear to have no regularity at all. Finally we consider the grand design galaxies NGC 5194 and 3031, which have extremely weak three arm components, and which may be the only examples of companion-triggered spirals in our sample.

### *NGC 613*

The two-arm pattern begins approximately at the end of the bar and ends at $\sim 0.9R_{25}$, as seen from Figure 2c. In the $S_3$ image, there is an equilateral triangle surrounding the center, spiral arms come off from each apex of the triangle with a break or kink, and then there is further three-arm structure beyond. The inner radius of the triangle (i.e., the radius of an inscribed circle) is $\sim 0.26R_{25}$, as measured directly from Figure 1c, and the radius of the break in the three arms is $\sim 0.7R_{25}$, as measured best from Figure 2c. The far-outer radius of the three-arm structure is about the same as the outer radius of the two-arm structure.

We identify the outer extent of the two-arm structure at $0.9R_{25}$ with the OLR, as discussed above, in which case Table 2 indicates that the inner 3:1 resonance should be at $0.26R_{25}$ and the outer 3:1 resonance at $0.77R_{25}$. These are the limits of the continuous part of the three-arm structure as shown on the bottom right of Figure 1c. Thus we identify the inner radius of the triangle with the inner 3:1 resonance and the outer extent of the continuous three arms with the outer 3:1 resonance. Note that this implies that the three-arm and two-arm structures have about the same pattern speeds.

Table 2 also indicates that corotation is at $0.570.9R_{25} = 0.51R_{25}$, which is the end of the bar, as seen most clearly from Figure 1c. The apex of the equilateral triangle has a radius comparable to this, but slightly smaller, $0.40R_{25}$. The inner 4:1 resonance, at $0.32R_{25}$, corresponds to the inner extent of the bright star-forming part of the bar. This inner extent of star formation is also at the inner 4:1 resonance for the other strongly barred galaxy in our sample, NGC 1300 (see sect. 3.2.12).

Figure 1c indicates that NGC 613 is a clean superposition of a two-arm pattern with a bar and a three-arm pattern with a triangle. Most of the arc-like features in the original galaxy can be identified with one or another part of this superposition, including the ovals that surround the bar and give it an eyelid shape. Even though this galaxy appears to have a complicated structure, it is somewhat simple when broken into the two components shown on the $S_2$ and $S_3$ images. The resonances also clearly delineate this structure.

*NGC 5457 (with a comparison to NGC 3031)*

NGC 5457 is another example of a galaxy that appears complex in the sky but is much more simple when broken into its two main components (plus a seemingly random residual from star formation, seen on the $A_2$ image). The outer extent of the symmetric two-arm spirals, i.e., on the $S_2$ image, is $\sim 0.75R_{25}$. Some very bright star formation patches make the spirals go further than this on the sky-enhanced image, but this extension may not be part of the stellar density wave because the patches are not symmetric or continuous. Moreover, gas spirals which might contain such star formation can go beyond the outer stellar Lindblad resonance because of dissipation.

A strong three-fold spiral is present in the $S_3$ image of NGC 5457, with an equilateral triangle in the inner part and continuous arms emanating from the apexes. This is similar to the three-fold structure in NGC 613. The inner radius of the triangle is $\sim 0.19R_{25}$ and the outer extent of the three spirals is $\sim 0.63R_{25}$.

We identify the outer extent of the symmetric two-arm spirals at $0.75R_{25}$ with the OLR. Then Table 2 predicts an inner 3:1 resonance at $0.19R_{25}$ and an outer 3:1 resonance at $0.63R_{25}$, which are the radii limiting the observed three-fold structure (see circles on the $S_3$ image in Fig. 1n). Thus the three-fold structure in NGC 5457 has the same resonance limits as the nearly identical structure in NGC 613. Again this implies that the pattern speeds for the two and three-arm spirals are about the same.

Table 2 also indicates that corotation for NGC 5457 should be at $0.41R_{25}$. As seen best on Figure 2n, this is the radius on the $S_2$ image where the arms break and shift in angle by about 76 deg. This break gives the false impression that NGC 5457 has a four arm structure (Fig. 1n; and see below), but in fact the break is almost identical to one in NGC 3031, as discussed earlier (EES) and shown here again in Figures 1g and 2g. Note how similar the $S_2$ $(\log R, \theta)$ diagram for NGC 5457 looks to either the $S_2$ or the sky-enhanced $(\log R, \theta)$ diagrams for NGC 3031. The spiral arms in each case have a segment with a high pitch angle ($\sim 25$ deg and $\sim 17$ deg respectively) at intermediate radii, between $0.24R_{25}$ and $0.4R_{25}$ for NGC 5457 and between $0.35R_{25}$ and $0.5R_{25}$ for NGC 3031. Then there is a gap in spiral arm brightness with a shift in phase of the spiral arms by $\sim 76$ deg for NGC 5457 and $\sim 65$ deg for NGC 3031. At larger radii, the spirals continue with about the same pitch angle they had at intermediate radii until they stop abruptly at $0.75R_{25}$ on the $S_2$ image of NGC 5457 and at $\sim 0.9R_{25}$ on both the enhanced and the $S_2$

images of NGC 3031.

The $S_2$ and enhanced images of NGC 3031 appear much more similar to each other than the same two images of NGC 5457 because NGC 3031 has much less star formation than NGC 5457, which has giant HII regions all the way out to $R_{25}$. Aside from this difference in gas content, and aside from the strong $m = 3$ spiral in NGC 5457, the underlying $m = 2$ spirals in the outer parts of the two galaxies appear very similar. The spirals in the inner parts of the two galaxies also differ because they are strong all the way to the nucleus in NGC 5457 while they end in a large circle at $0.35R_{25}$ in NGC 3031. Presumably this difference results from the presence of a wave-reflecting bulge in NGC 3031 (EES) but not in NGC 5457, and from the large amount of gas in NGC 5457, which allows spiral penetration through the inner Lindblad resonance or to a small bar in the inner region. In NGC 3031, there is a weak spiral, visible mostly as a dust lane, that goes into the nucleus in the same way as the strong spiral does in NGC 5457.

Even though the $m = 2$ parts of the spirals in NGC 3031 and NGC 5457 appear very similar to each other, there is an important difference in the locations of the resonances. In NGC 3031 the spiral arm break is at the inner 4:1 resonance (EES) and in NGC 5457 it is at corotation. This difference shows up on Figure 2 as a larger outer arm segment beyond the break in NGC 3031 than in NGC 5457. Because these diagrams are plotted in the logarithm of radius, a larger extent beyond the break corresponds to a larger ratio of the OLR (at the ends of the arms) to the resonance radius at the break.

NGC 5457 also has another prominent feature at corotation that is not shared by the gas-poor galaxy NGC 3031. This is a termination point for the bright star formation ridges and dust lane structures in the main arms to the north and south.

Such star formation ridges were also found in NGC 4321 (EES) and 1566 (EE90), with similar terminations at corotation. This is a sensible resonance feature in these gas rich galaxies because star formation should be most strongly associated with the spirals inside corotation (Roberts 1969).

The impression from the $S_2$ image that NGC 5457 contains four arms is the result of an inward extension of the outer symmetric arms from $0.40R_{25}$, where the break occurs, to $0.20R_{25}$. In this radial range there are really four arms. This structure is clear on the $S_2$ $(\log R, \theta)$ diagram in Figure 2n, especially between $0.25R_{25}$ and $0.35R_{25}$, and also on the sky-enhanced $(\log R, \theta)$ diagram between $0.20R_{25}$ and $0.40R_{25}$. Part of this four-arm structure is a very bright strip of star formation pointing almost in the radial direction, due south of the galactic center between $0.21R_{25}$ and $0.27R_{25}$, and midway between the main arms in this radial range (see Fig. 2n). There is no counterpart on the opposite side of the galaxy, so it does not appear on the $S_2$ image or the $S_2$ $(\log R, \theta)$ diagram. This strip of star formation, along with the arm extensions making the four-fold structure, occur near the inner 4:1 resonance, which, from Table 2, is at $\sim 0.32$ times the OLR radius, or $0.24R_{25}$, as shown by the circle on the $S_2$ image in Figure 1n. At this radius, the four spiral arms are clearly seen to be equally separated in angle.

Similar spurs were found at the 4:1 resonance radii in NGC 3031, NGC 4321 (EES) and NGC 1566 (EE90), and nowhere else in these other galaxies. They were also found at the inner 4:1 resonance in M51 (EES), but in this case there is another set of spurs at corotation, so the picture is less clear. Perhaps this second set of spurs in M51 is the result of a beat interaction at corotation between two $m = 2$ spirals, one a tidal arm in the outer part and the other an inner wave mode (EES, E91, Taggar, private communication). Apparently such complications do not arise

for many galaxies, in which case the observation of spurs midway between the arms, or the observation of short four-arm structures, provide clues to the location of the 4:1 resonance.

*NGC 4321*

Resonances for this grand design galaxy were previously discussed in EES. The best fit places the OLR at $1.1R_{25}$ where the main two-arm spiral system ends, corotation at $0.57R_{25}$, where the bright ridge of star formation in each arm and the prominent dust lanes end, and where there is a circle of interarm star formation all around the galaxy, the inner 4:1 resonance at $0.35R_{25}$, where there is a pair of spurs midway between the main arms and diametrically opposite each other in the galaxy, and either no ILR or an ILR that lies inside the main spiral system, which appears to end in the inner region in a circle where the wave reflects. These resonance radii are consistent with the $S_2$ images given here too. (Note that the ratios in Table 2 suggest the inner 4:1 resonance is at $0.33R_{25}$ for an OLR at $1.1R_{25}$, but the better fit given here is $0.35R_{25}$. This resonance for NGC 4321, and several resonances for NGC 5194, are the only cases where the ratios from Table 2 are not used for the circles on Figure 1 or the entries in Table 3.)

NGC 4321 also has a prominent three-fold spiral, starting in the inner region at the same radius as the inner extent of the main two-arm spiral, at $\sim 0.25R25$, and continuing out to a maximum radius of about $0.9R_{25}$, as seen best on the $(\log R, \theta)$ diagram of the $S_3$ image. These are the same radii as the inner and outer 3:1 resonances, respectively, if we use Table 2 and an OLR at $1.1R_{25}$. Thus the three-arm spiral in NGC 4321 extends between the 3:1 resonance limits for about the same pattern speed as the two-arm spiral.

*NGC 5248*

NGC 5248 has strong two-arm spirals that extend out to $\sim 1.0R_{25}$ with very strong star formation ridges and dust lanes in each arm, ending sharply at $0.53R_{25}$. This structure is best seen on the sky-enhanced image. The $S_2$ image suggests that there may be an oval potential in the inner region, because of the way the dust lanes twist in, as in a barred galaxy.

The three-arm structure is less clear here than in other galaxies, but there are still at least two out of the usual three arms (separated by 120 deg) in the inner region, and there are faint triple arms in the outer region. The inner extent of the three-arm structure is $\sim 0.24R_{25}$ and the far outer extent of the faint outer structure is $\sim 0.84R_{25}$, as seen best from the $S_3$ image. There is a gap in the three-arm structure at a radius between $0.5R_{25}$ and $0.6R_{25}$.

We take the OLR to be the outer radius of the two-arm spirals, at $1.0R_{25}$. Then Table 2 suggests corotation is at $0.53R_{25}$, which is nicely placed at the end of the bright star formation ridge and dust lane structure. The inner 3:1 resonance is at $0.24R_{25}$ from Table 2, which is the inner extent of the 3:1 spiral, and the outer 3:1 resonance is at $0.84R_{25}$ from Table 2, which is about the observed outer extent of the three arms. Thus the two and three-arm spirals are both limited by their respective resonance radii (see circles in Figure 1m), but there is a gap in the three-arm structure at corotation.

The inner 4:1 resonance is expected to be at around $0.31R_{25}$ from Table 2, but there is no obvious *mid-arm* spur at this location. There is an asymmetric spur or feature there, however, between $0.30R_{25}$ and $0.40R_{25}$ on the $(\log R - \theta)$ version of the sky-enhanced image, but this feature is not midway between the arms, as are the other 4:1 resonance spurs discussed here. Nevertheless, it is the most prominent

spur in this galaxy, and its location near the 4:1 resonance suggests an analogy with the other spurs.

*NGC 628*

NGC 628 is a multiple arm galaxy with numerous star formation patches. The two-fold structure on the $S_2$ image extends to $0.9R_{25}$. There are prominent ridges of star formation in each of these two arms, abruptly stopping almost due north and south of the nucleus at $0.46R_{25}$ (see the $S_2$ image especially). There are also spurs of star formation at about this same radius, and another, fainter pair of symmetrically opposed spurs at radii between $0.18R_{25}$ and $0.30R_{25}$.

NGC 628 also contains a strong three-fold structure with an inner equilateral triangle (irregular in this case) having an inner radius of $\sim 0.20R_{25}$ and an outer spiral extent of $\sim 0.75R_{25}$. Inside the inner radius there are three symmetric dustlanes, but all three are probably not real (see discussion sect. 2); their presence here illustrates the fact that the two real dustlanes in the inner region are not perfectly symmetric across the galactic center.

We take the outer extent of the two-fold symmetric spiral, at $0.9R_{25}$, to be the OLR. Then Table 2 indicates that the outer 3:1 resonance should be at $0.75R_{25}$, which is where the three-fold structure ends, and the inner 3:1 resonance should be at $0.20R_{25}$, which is about the inner extent of the three-arm spiral.

Corotation in NGC 628 should be at $0.46R_{25}$, according to Table 2. This is where the ridges of star formation and strong dust lanes end on the two main arms, and so is a sensible result. There is also a bright pair of spurs at this radius. The inner 4:1 resonance should be at $0.26R_{25}$ according to Table 2, and this is the

location of the inner symmetric spurs. All of these theoretical resonance radii are shown as circles in Figure 1d; the suggested correlations with details of the spiral structure are clear.

*NGC 6946*

The $S_2$ image of NGC 6946 is dominated by a thick and bifurcated two-arm spiral, and the $S_3$ image shows a thick three-arm spiral. The inner radius of the three-arm spiral is $0.18R_{25}$ and the outer radius is $0.78R_{25}$. The ratio of these distances is 4.3, which is also the theoretical ratio for the 3:1 resonances in Table 2, so an identification with these resonance limits seems reasonable. The OLR is then determined from the outer 3:1 resonance to be at $0.78R_{25}/0.82 = 0.95R_{25}$, which is the far outer extent of the main spiral system. Corotation is at $0.47R_{25}$ according to Table 2, and this is about the termination radius for the main dust lanes and bright star-forming regions in the main symmetric ($S_2$) arms in the northeast and southwest and also the radius of a bifurcation in the northeastern arm. The inner 4:1 resonance is at $0.25R_{25}$, which is not particularly distinctive except perhaps as a demarkation for the inner extent of the strong star formation. There is a strong one-arm spiral inside the inner 4:1 resonance; a symmetric counterpart to this arm is not visible in the sky image and it may have been lost by the galaxy's inclination.

*NGC 598*

NGC 598 has a multiple arm structure with a bar in the central region, a two-arm spiral with a large pitch angle, and a three-arm spiral with an inner triangle. The $S_2$ image also shows a faint *leading* spiral between the outer part of the bar and

the outer part of the main trailing arms, giving an overall eyelid shape. There are also faint outer arms on the $S_2$ image, making a large figure eight shape with the two leading arms.

According to Table 2, the ratio of the outer to the inner 3:1 resonances is expected to be 5.8, which is extremely large because of the large $\alpha$. This makes sense on the $S_3$ image if we identify the inner 3:1 resonance with the inner extent of the three radial pieces that jut inward from the sides of the equilateral triangle, at $\sim 0.13R_{25}$, and the outer 3:1 resonance with the outer extent of the three bright arms, at $0.75R_{25}$. Then the OLR is at $0.95R_{25}$, from Table 2, and corotation is at $0.40R_{25}$. This OLR is close to the overall extent of the spiral system, seen for example on the Palomar Observatory Sky Survey (not in the figures here), and so is a sensible result. The corotation resonance is at about twice the bar length and where the bright star formation ends in the east on the sky-enhanced image, and the dark dust lanes end in the east and west on the $S_2$ image. There are other star-forming ridges beyond this presumed corotation radius, however, and this makes our fit somewhat uncertain. The inner 4:1 resonance at $0.19R_{25}$ is where the bar ends and the bright star formation in the arms begins.

## *IC 342*

IC 342 has open multiple arms similar to those in NGC 598. The overall extent of the arms is $\sim 1.4R_{25}$ and the extent of the inner bright part is $\sim 0.7R_{25}$. The three arm structure lies between $\sim 0.28R_{25}$ and $1.13R_{25}$. We take these latter values to be the inner and outer 3:1 resonances because they have about the correct ratio from Table 2. Then the OLR is at $1.38R_{25}$, where all the arms end, corotation is at $0.68R_{25}$ where the two inner star formation ridges end, and the inner 4:1 resonance

is at $0.37R_{25}$, which has no special feature except perhaps for an inner limit to the bright star formation in the arms. The features that fit these resonances are similar to what we found elsewhere, although additional, perhaps random, arms seem to be present in IC 342 also.

*NGC 1232*

This is a multiple arm galaxy with patchy star formation. There is a thin symmetric two-arm spiral in the inner region and a broad symmetric two-arm spiral in the outer region (on the $S_2$ image). The outer spiral ends on the sky-enhanced image at $\sim 0.91R_{25}$, which we identify as the OLR. There is also a three-arm spiral on the $S_3$ image, beginning at $0.23R_{25}$ and ending at $0.78R_{25}$, which are approximately the inner and outer 3:1 resonance radii calculated from Table 2, given the OLR at $0.91R_{25}$. Table 2 also indicates that corotation should be at $0.53R_{25}$, which is the outer extent of the star formation ridges in the north and east (see the image in Sandage and Bedke 1988, where north is to the left), and the outer envelope of the star formation patches in the south. There is nothing obvious at the inner 4:1 resonance, at $0.34R_{25}$.

The inner extent of the three arm spiral is not exactly at the predicted inner 3:1 resonance, as it is for many of the other galaxies studied here. The inner 3:1 fit at $0.27R_{25}$ (from Tables 2 and 3 and where the circle is on Fig. 1e) is slightly too large. The inner 4:1 fit at $0.34R_{25}$ is also slightly too large, if we consider that many of the other galaxies have their main star formation ridges outside the inner 4:1 resonance, out to corotation. The corotation resonance and OLR fits are sensible for NGC 1232, however. The agreement in the inner part of the galaxy would be better if the rotation curve did not have a constant $\alpha$ down to $0.27R_{25}$ but a larger $\alpha$ at

small radii than in the vicinity of corotation. This corresponds to a larger extent of the rising part of the rotation curve in the inner region of the galaxy, compared to the other galaxies studied here.

The brightest part of the thin inner spiral lies almost entirely within the theoretically estimated ILR at $0.15R_{25}$. This ILR identification is unusual for our sample (most of our galaxies have an ILR well inside the spiral patterns), and it may have important implications. For M51, we found (EES) that the main spiral arm system, especially in the I band, ends at the outer edge of the bright disk but not at the outer edge of the whole spiral pattern. We identified this outer disk edge with the OLR of the main pattern given the other resonance indicators, such as the termination radii for star formation ridges and dust lanes, spurs at the inner 4:1 resonance, and so on (see also 3.2.17 below). Beyond the OLR for NGC 5194, another two-arm spiral extends out to about $R_{25}$, with a kink and slight phase shift with respect to the inner main spiral at the radius of overlap. We followed Tully (1974) in identifying this outer spiral system as material tidal arms. Then we found that the corotation resonance for the inner spiral system lies within the approximate range of radii for the inner Lindblad resonances of the outer material arms (as determined by Howard and Byrd 1990), and suggested that these outer arms triggered the inner spiral pattern, which we take to be a wave mode, by a resonance interaction. Such triggering is analogous to the resonant excitation discussed by Taggar et al. (1987).

NGC 1232 may have a similar resonance interaction. It is unusually luminous for our sample, so it has one of the smallest values of $\alpha$ and one of the largest ratios of the ILR to the OLR. This means that the ILR is relatively far out in the main disk, at $0.15R_{25}$ according to the discussion above. Then the inner part of the disk is perturbed by the main spiral system, and if conditions are right, can form an

independent wave mode with corotation at the ILR of the outer spiral. Thus we suggest that the thin inner spiral in NGC 1232 has a different pattern speed than the main spiral, and a corotation resonance at about $0.15R_{25}$, which is our guess for the inner Lindblad resonance of the outer spiral. This puts the OLR for the inner spiral at $\sim 0.26R_{25}$ for the same $\alpha$ as in the outer disk, or at larger radii if $\alpha$ is larger in the inner regions. This is approximately where the inner spiral joins onto the outer spiral, and is the inner boundary of the three-arm structure (see Fig. 2e).

*NGC 4254*

This galaxy differs from others in the sample because it is largely dominated by a three arm structure. The same result was obtained by Iye et al. (1982) who also found a strong one-arm spiral using Fourier transforms; our images show more precisely where the three arm structure comes from. The $S_3$ image indicates that the three arms end in the outer part at an average radius of $\sim 0.9R_{25}$, and they extend in the inner regions to $\sim 0.23R_{25}$. The ratio of these radii is 3.9, which is the expected ratio of the outer to the inner 3:1 resonances, from Table 2. Thus we identify these radii with the 3:1 resonance locations. This places the OLR at $0.9R_{25}/0.83 = 1.08R_{25}$, which is the outer radius of the longest arm in the spiral system, and it places corotation at $0.54R_{25}$, which is the termination radius of the thick star formation ridge in the southern arm (see the sky-enhanced image in Figure 1i, or Sandage and Tammann 1981). Corotation is also in the midst of the patches of star formation in the east (for no obvious physical reason unless this is wave-independent star formation). The inner 4:1 resonance at $0.3R_{25}$ is at the position where the bright arm bifurcates (see the sky-enhanced image in Figure 2i).

*NGC 6912*

NGC 6912 also has mostly a three-arm structure, beginning at a radius of $\sim 0.37R_{25}$ and ending at $\sim 1.2R_{25}$, as seen best in Figure 1o. The ratio of these radii is 3.2, which equals the ratio of the outer to the inner 3:1 resonance radii from Table 2. Thus we assume that the outer 3:1 resonance is at $1.2R_{25}$ and derive an OLR at $1.41R_{25}$, which is the radius of the most distant HII regions in the spiral arms on the sky-enhanced image. Corotation is then at $0.78R_{25}$, which is the radius of a break in the three-arm spiral, as seen on the left in the $S_3$ image, and on the $(\log R, \theta\ )$ diagram of the $S_3$ image. The inner 4:1 resonance is at $0.47R_{25}$, which has no obvious resonance features. These identifications are consistent with the results for the other galaxies.

*NGC 1300*

NGC 1300 is a barred galaxy with strong star formation at the ends of the bar, at $\sim 0.5R_{25}$, and spiral arms that extend out to $\sim R_{25}$, although the two-fold symmetric part of the arms ends at about $0.9R_{25}$. There is a three-arm component also with slightly smaller extent. A reasonable fit to resonances with the ratios in Table 2 places the OLR at $0.88R_{25}$, where the symmetric spirals end, corotation at $0.52R_{25}$, which is slightly outside the bar end and at a place in the arms where the dust lanes appear to cross from inside to outside the arms (e.g., see image in Sandage 1961), the outer 3:1 resonance at $0.76R_{25}$, which is approximately where the three-fold structure ends, and the inner 3:1 resonance at $0.27R_{25}$, which is the inner extent of the triangle. The inner 4:1 resonance in NGC 1300 is at the inner extent of the bright star formation in the bar, as it was for NGC 613. There is no obvious explanation for this 4:1 resonance limit, but the other circles in Figure 1f

are reasonable, considering the results for the other galaxies.

*NGC 157*

NGC 157 contains a strong inner symmetric spiral and outer irregular arms. The $S_3$ image is mostly triangular as in NGC 1300. The outer extent of all the arms is $\sim 0.77R_{25}$, the outer extent of the strong symmetric arms on the $S_2$ image is $\sim 0.44R_{25}$ and the outer extent of the triangle is $\sim 0.65R_{25}$. These radii have the proper ratios from Table 2 to be the OLR, CR, and outer 3:1 resonances, respectively. The strong symmetric arms are apparently triggered star formation (see image in Sandage 1961). The inner 3:1 resonance is then at $0.22R_{25}$, which is the inner extent of the triangle. The inner extent of the inner two-arm symmetric spiral, where there appears to be a bar, is approximately at the inner 4:1 resonance, at $0.27R_{25}$. The circles in Figure 1a indicate that these fits are similar to those for the other galaxies.

*NGC 3938*

NGC 3938 has an irregular spiral structure with two strong arms in the inner part and multiple arms in the outer part, extending out to $\sim 1.1R_{25}$. We group it here with the two flocculent galaxies, NGC 7793 and 5055, although it is probably different in nature. The irregular structure ends at about $0.8R_{25}$, which is inside the outer 3:1 resonance if we take the OLR at $1.1R_{25}$, so in this respect NGC 3938 is unlike the galaxies discussed previously. Indeed, there is no convincing three-arm structure in the $S_3$ image of Fig. 1h.

There is a higher order structure, however, and this was investigated by making

the $S_4$, $S_5$ and $S_6$ images shown in Figure 3 (using equations similar to those in sect.2). The $S_4$ image shows very little structure, but the $S_5$ and $S_6$ images have relatively clear spirals, with the five arm structure the clearest. Thus NGC 3938 probably contains five arms in a semi-regular pattern. The circles in Figure 3 are the inner and outer 4:1, 5:1, and 6:1 resonances for an OLR at $1.1R_{25}$; they are at $0.30R_{25}$ and $0.81R_{25}$, $0.35R_{25}$ and $0.76R_{25}$, and $0.38R_{25}$ and $0.72R_{25}$, respectively. The 5:1 and 6:1 resonances bracket the spirals nicely.

With this fit, the corotation resonance is at $0.55R_{25}$ and the inner and outer 3:1 resonances are at $0.23R_{25}$ and $0.91R_{25}$, as shown by the circles in Figure 1h. The circles on the $S_3$ image have no relation to the spiral structure, as discussed above. The circles on the $S_2$ image are sensible limits to the outer extent of the two-arm spiral and, at corotation, to the outer extend of the bright part of the inner spiral, which may be triggered star formation (see image in Sandage and Bedke 1988).

### *NGC 7793*

NGC 7793 is a flocculent galaxy without any prominent two-arm spiral, but it still has a three-lobed structure on the $S_3$ image. This may be the result of a random distribution of star formation, but one can still imagine a triangular structure there, as on many of the other $S_3$ images. If the outer 3:1 resonance is the outer extent of this triangle, at $0.79R_{25}$, then the OLR from Table 2 is at the far outer extent of the galaxy, at $1.01R_{25}$, which is consistent with the OLRs for the other galaxies even though there is no two-arm spiral here. The inner 4:1 resonance in this case marks the inner limit of the spiral system, at $0.19R_{25}$, and the inner 3:1 resonance at $0.13R_{25}$ is inside the inner extent of the three-fold structure. Perhaps there is a weak three-arm mode in NGC 7793 with an inner reflection at $\sim 0.23R_{25}$, outside

the inner 3:1 resonance, but no $m = 2$ mode. There is also a lot of star formation in patches everywhere, so there could be no waves at all.

*NGC 5055*

NGC 5055 is a flocculent galaxy similar to NGC 7793, but in this case there is no perceptible symmetric structure in either the $S_2$ or $S_3$ images. For comparison with the other galaxies, we draw a circle at the outer edge of the disk, at $0.76R_{25}$, and four other circles at radii proportional to this value, corresponding to the ratios of the inner 4:1, 3:1, corotation and outer 3:1 resonances in Table 2.

*NGC 5194*

NGC 5194 has a bright three-fold structure that differs from the others here, with a strong triangle between an inner radius of $\sim 0.2R_{25}$ and an outer radius of $\sim 0.5R_{25}$, and two faint arms that extend from the ends of this triangle. These two faint arms are probably not parts of a true three-arm spiral, because of contamination by the companion galaxy. One of the three arms, in the southwest, is the same as one of the strong two arms, and the other of the three arms, in the north, is part of the emission from the companion and probably not a true arm. There is no third arm at the other apex of the triangle.

For the resonances we take the same fit as that given in EES, which originally came from Tully (1974). Using Figure 5 in Tully (1974), we derive corotation at $0.4R_{25}$, the OLR at $0.56R_{25}$, the inner and outer 3:1 resonances at $0.20R_{25}$ and $0.51R_{25}$, and the inner 4:1 resonance at $0.25R_{25}$. These radii are shown by the circles in Figure 1. The resonance features that fit the inner 4:1, CR and OLR

radii were discussed in EES: spurs at the inner 4:1 resonance, the ends of the bright star formation ridges on each side of the galaxy at CR, a crossing of the spiral arms by the dust lanes at CR, and the edge of the bright part of the disk and the near-infrared spirals at the OLR. Now we see in addition that the inner and outer 3:1 resonances bracket nicely the three-fold structure in Figure 1. This is consistent with the 3:1 resonance limits for the three-fold structure found in other galaxies in this survey, but here the structure is not a spiral, nor is it like the weak triangles in NGC 1300 and 157.

*NGC 3031*

NGC 3031 has a bright circle with three lobes in the $S_3$ image and a faint three-arm structure radiating from this circle. There is also a small amount of three-arm structure inside the circle. The outer extent of the three faint arms is $\sim 0.80R_{25}$, and the inner extent is $\sim 0.38R_{25}$, as determined from both the $S_3$ image and the $(\log R - \theta)$ version of this image. The ratio of these two radii is 2.1, which is the same as the expected ratio of the outer to the inner 3:1 resonance radii.

The two-arm resonance locations in NGC 3031 were previously estimated by EES. The OLR was placed at $1.05R_{25}$, but a better estimate here is $0.90R_{25}$, which is a more precise match to the outer extent of the main spiral arms and, according to Table 2, also equal to the OLR position if the outer 3:1 resonance is as $0.80R_{25}$, as suggested above. Then the inner 4:1 resonance is at $0.44R_{25}$, which is the radius where the interarm spurs in the north are midway between the arms. Corotation is then at $0.60R_{25}$, according to Table 2. The inner extent of the spiral is well outside the ILR, presumably because of a wave reflection at $0.35R_{25}$. Other features in NGC 3031 were discussed above in Section 3.2.2.

## 3.3. Summary

The resonance fits for the 18 galaxies discussed above are summarized in Table 4. All of the galaxies except NGC 5055 have two-arm structures that end at the outer 2:1 resonance (but NGC 5194 has tidal arms outside this), and all but NGC 3938 and NGC 5055 have three-arm structures that end at the outer 3:1 resonance. All but two, NGC 3938 and NGC 7793, have three-arm spirals that end in the inner region at the inner 3:1 resonance. These exceptions result from a lack of spiral waves in NGC 5055 and 7793, which are flocculent; NGC 3938 probably has a five arm spiral. Thirteen of the galaxies have star formation ridges and dense dust lanes that end at corotation, a few others have only dust lanes that end there, and five have spurs or four arm structure at or near the inner 4:1 resonance. Most have an inner limit to the realm of brightest star formation that is at or close to the inner 4:1 resonance.

All of the galaxies with strong two arm spiral waves (i.e., not NGC 3938, 7793, or 5055) have some possibility of an inner wave reflection in the inner parts, either at a bar or oval or in a hot bulge outside the inner Lindblad resonance. None of the galaxies but NGC 7793 has the possibility of a similar type of reflection for a three arm spiral, and in this case there may not be a wave at all. Most of the three arm spirals exist exactly between the inner and outer 3:1 resonance limits for the same pattern speeds as the two arm spirals. We conclude from this latter result that most three arm spirals are not wave modes with reflection and self-amplification, but rather waves driven out to their resonance limits by the two arm spirals.

This latter possibility was checked by examining the asymmetry in the two arm spirals, as seen on the $A_2$ images. If the three arm spirals arise as a beat frequency interaction between the two arm spirals and a one arm component, then

the brightest arm in the two arm spiral should occur at the same position as one of the three arm spirals. This is true in every case where there is a clear three arm spiral (i.e., it is not true for NGC 157, 1300, 5055 and 7793). One of the three arms coincides with the brightest part of the two arm spiral, as seen on the $A_2$ image, and the other two arms in the three arm spiral coincide with only minor features on the original or enhanced image. NGC 598 is an exception because different parts of different arms in the three arm pattern coincide with patches in the main pattern, which is not clearly dominated by only two arms. We could also say that the three arm spirals never have an arm that coincides with the weaker of the two arms in the two arm system.

Thus there are three independent arguments that lead to the conclusion that the three arm spirals are driven by the two main arms: (1) the two and three arm systems have the same pattern speeds, when each is fitted to its respective outer limiting resonance radii; (2) the three arm spirals are located precisely between their inner and outer resonance radii, so there is no possibility of wave reflection, and (3) the stronger of the two main arms coincides with one of the three arms, so the driving arm in the mutually rotating 2+3 arm component system is identified.

## 4. Fourier Transforms

Figure 4 shows the power in the m=2 and m=3 components of the azimuthal Fourier transforms of each galaxy, as functions of radius. As expected, the grand design spirals NGC 3031, 4321, and 5194 are dominated by the m=2 component, and the three-arm galaxies, NGC 4254 and 6912, have large m=3 components at some radii. Other galaxies have relatively strong m=3 components where the three-arm spirals appear in Figure 1, but the general run of Fourier transform power with

radius contains too many fluctuations to identify the end points of these three arm spirals as well as they can be identified on an S sub 3 image. The m=1 component is not plotted because it is usually dominated by background intensity gradients and not by spiral arm asymmetries.

## 5. Conclusions

Most galaxies have three-arm spirals in addition to the more prominent two-arm spirals. The ratio of the outer to the inner extents of the three-arm spirals is usually the theoretical ratio of the outer to the inner 3:1 resonances, making these limits reasonable resonance indicators. Then the outer extents of the two arm spirals are the outer Lindblad resonances in every case, in agreement with Lin and Shu (1967), and corotation is consistent with theoretical expectations based on gas dynamics and star formation. For example, at corotation the brightest ridges of star formation and the darkest dust lanes generally end on each side of the galaxy. The implied inner 4:1 resonances are sometimes visible too, in the form of spiral arm spurs exactly midway between the main arms and in the form of four-arm structure, which is rare. This is a very different interpretation of resonances than that given by Patsis et al. (1991), who suggest that the entire visible spirals in many galaxies are inside the 4:1 or corotation resonances. We see no evidence for this limitation here, and have suggested elsewhere (EE90; Elmegreen 1991) that the lack of dissipation and forcing from gas in their calculation could give them an artificial limitation at the inner 4:1 resonance. If spirals exist primarily outside the inner 4:1 resonances anyway, as found here, or if, as in the case of M81, they have a gap in strength at this resonance, then there would seem to be no problem with the star-wave scattering found by Patsis et al. (see also Artymowicz and Lubow 1992).

The inner extents of the main two-arm spirals are always outside the inner Lindblad resonances, unless a small bar is present in the inner region (e.g. EE90), and these inner spirals usually wrap into a circle at $\sim 0.2 \pm 0.1 R_{25}$. This suggests that the two-arm spirals have reflective barriers in the inner regions, and that they are wave modes. Most three-arm spirals are not independent modes, however, because their inner limits usually coincide with the inner 3:1 resonances. The three-arm spirals instead are probably driven waves, which absorb energy from the two-arm spirals that rotate around with them, and lose energy to random stellar motions at the 3:1 resonances. Presumably the three-arm spirals build up in strength with time after the two-arm spirals are formed. In that case, predominantly two-arm galaxies would have younger patterns than multiple-arm galaxies, which get this chaotic structure from the superposition of two and three-arm (or even higher order) components.

It is particularly interesting that the strong two-arm galaxies NGC 3031 and NGC 5194 have relatively weak or no three-arm spirals. These galaxies are likely to have been exposed to tidal forces recently (which would account for their two-arm structures) and it is possible that strong three-arm structures will eventually form in them, as in the other galaxies, but the three-arm structures in them now have not yet had time to grow to the strength that we see in the other galaxies. Perhaps three-arm structures will provide a good measure of the time that has elapsed since a tidal interaction.

A secondary result of this study is that spiral density waves apparently trigger or organize star formation with greatest intensity between the inner 4:1 resonance and the corotation resonance, as found before (EES). Such organization is shown by a bright continuous ridge of star formation with a sharp boundary, often accompanied

by a continuous dust lane. Because the radial extents of the observed star formation ridges are only small fractions ($\sim$ 20%) of the total extents of the optical disks (out to $R_{25}$), and even smaller fractions ($\sim$ 15%) of the areal extents of the disk, the fraction of the total star formation in a galaxy that is directly triggered by a spiral density wave would seem to be small, consistent with the estimate in Elmegreen and Elmegreen (1986) that it is less than 50%. Most of the star formation in a spiral galaxy is apparently initiated without a strong density-wave shock. Conversely, most of the reason why we see the spirals is because the waves are strong, not because triggered star formation highlights them (Elmegreen 1987).

Acknowledgments: We thank Philip Seiden for substantial contributions to the computer programming involved with this study, and C.C. Lin for helpful comments. Thomas Blersch and David Reiss were involved in an early phase of this work, and Victoria Moore helped with some of the final image production. D.M.E. is grateful for a Vassar College research grant.

## REFERENCES

Angilello, J., Chiang, W.H., Elmegreen, D.M., and Segmuller, A. 1984, in Proc. Conf. Goddard Astronomical Microdensitometry, ed. D.A. Klinglesmith (NASA CP- No. 2317), p. 229.

Artymowicz, P., and Lubow, S.H. 1992, ApJ, 389, 129.

Athanassoula, E., Bosma, A., and Papaioannou, S. 1987, AA ,179, 23.

Bertin, G., Lin, C.C., Lowe, S.A., and Thurstans, R.P. 1989, ApJ, 338, 78.

Bertin, G. 1991, in Dynamics of Galaxies and their Molecular Cloud Distributions, ed. F. Combes and F. Casoli, Dordrecht: Kluwer, p. 93.

Biviano, A., Girardi, M., Giuricin, G., Mardirossian, F., and Mezzetti, M. 1991, Ap.J., 376, 458.

Carlberg, R.G., & Freedman, W.L. 1985, ApJ 298, 486.

Considére, S., and Athanassoula, E. 1988, AA Suppl., 76, 365.

de Vaucouleurs, G. 1963, ApJ Suppl, 8, 31.

de Vaucouleurs, G., de Vaucouleurs, A., and Corwin, H.G., 1976, Second Reference Catalogue of Galaxies, (Austin: Univ. of Texas).

Danver, C.G. 1942, Lund Obs.Ann. Vol. 10.

Elmegreen, B.G. 1987, in IAU Symposium 115: Star Forming Regions, ed. M. Peimbert and J. Jugaku, (Dordrecht: Reidel), 457

Elmegreen, B.G. 1991, in Dynamics of Galaxies and their Molecular Cloud Distributions, ed. F. Combes and F. Casoli, Dordrecht: Kluwer, p. 113.

Elmegreen, B.G., and Elmegreen, D.M. 1985, ApJ 288, 438.

Elmegreen, B.G., and Elmegreen, D.M. 1986, ApJ 311, 554.

Elmegreen, B.G., and Elmegreen, D.M. 1990a, ApJ 355, 52.

Elmegreen, B.G., and Elmegreen, D.M. 1990b, ApJ 364, 412.

Elmegreen, B.G., and Thomasson, M. 1993, A A, 272, 37.

Elmegreen, B.G., Elmegreen, D.M., and Seiden, P.E. 1989, ApJ, 343, 602.

Elmegreen, D.M. 1981, ApJS, 47, 229.

Elmegreen, D.M., 1985, in IAU Symposium No. 106: The Milky Way, ed. H. van Woerden, Dordrecht: Reidel, p. 255.

Elmegreen, D.M., and Elmegreen, B.G. 1984, ApJ Suppl., 54, 127.

Elmegreen, D.M., and Elmegreen, B.G. 1989, ApJ, 314, 3.

Fridman, A.M., Morozov, A.G., Nezlin, M.V., Pasha, I.I., Polyachenko, V.L., Rylov, A.Yu., Snezhkin, E.N., Torgashin, Yu.N., Trubnikov, A.S. 1987, in Observational Evidence of Activity in Galaxies, ed. E.Ye. Khachikian, K.J. Fricke, and J. Melnick, (Dordrecht: Reidel), p. 147.

Hernquist, L. 1990, in Dynamics and Interactions in Galaxies, ed. R. Wielen, (Berlin: Springer), p. 108.

Howard, S., and Byrd, G.G. 1990, AJ, 99, 1798.

Hubble, E. 1926, ApJ, 64, 321.

Iye, M., Okamura, S., Hamabe, M., and Watanabe, M. 1982, ApJ, 256, 103.

Kennicutt, R.C., Jr. 1981, AJ, 86, 1847.

Krakow, W., Huntley, J.M., and Seiden, P.E. 1982, AJ, 87, 203.

Lin, C.C., & Shu, F.H. 1967, in IAU Symposium No. 31, Radio Astronomy and the Galactic System, ed. H. van Woerden (New York: Academic Press), p. 313.

Lin, C.C., and Lowe, S.A. 1990, in Galactic Models, Annals of the New York Academy of Sciences, ed. J.R. Buchler, S.T. Gottesman, and J.H. Hunter, Jr., Vol. 596, p. 80.

Patsis, P.A., Contopoulos, G., and Grosbol, P. 1991, AA, 243, 373.

Persic, M., and Salucci, P. 1991, ApJ, 368, L60.

Roberts, W.W. 1969, ApJ, 158, 123

Sandage, A. 1961, The Hubble Atlas of Galaxies, Carnegie Institute of Washington, Washington D.C.

Sandage, A., and Bedke, J. 1988, Atlas of Galaxies, (Washington D.C., US GPO).

Sandage, A., and Tammann, G.A., 1981, A Revised Shapley Ames Catalog of Bright Galaxies, Carnegie Institute of Washington.

Schweizer, F. 1980, ApJ Suppl., 31, 313.

Shu, F.N., Milione, V., and Roberts, W.W. 1973, ApJ, 183, 819.

Strom, S.E., Jensen, E.B., and Strom, K.M. 1976, ApJ, 206, L11.

Tagger, M., Sygnet, J.F., Athanassoula, E., and Pellat, R. 1987, ApJ, 318, L43.

Thomasson, M., Elmegreen, B.G., Donner, K.J., and Sundelius, B. 1990, ApJ, 356, L9.

Toomre, A. 1981, in The Structure and Evolution of Normal Galaxies, ed. S.M. Fall and D. Lynden-Bell, (Cambridge: Cambridge Univ. Press), p. 111.

Tully, R.B. 1974, ApJ Suppl., 27, 449.

van den Bergh, S. 1960, ApJ, 131, 215.

Visser, H.C.D. 1980, AA, 88. 149.

Wevers, B.M.H.R. 1984, PhD Dissertation, Groningen.

---

This manuscript was prepared with the AAS LaTeX macros v4.0.

Table 1: Galaxy Sample

| Name | Hubble Type | $R_{25}$ (arc min) | Absolute magnitude ($M_B$) |
|---|---|---|---|
| NGC 157 | SAB(rs)bc | 2.13 | -22.19 |
| 598 | SA(s)cd | 30.8 | -19.07 |
| 613 | SB(rs)bc | 2.88 | -22.24 |
| 628 | SA(s)c | 5.12 | -21.75 |
| 1232 | SAB(rs)c | 3.88 | -22.57 |
| 1300 | SB(rs)bc | 3.23 | -21.99 |
| 3031 | SA(s)ab | 12.85 | -20.75 |
| 3938 | SA(s)c | 2.69 | -20.54 |
| 4254 | SA(s)c | 2.69 | -21.59 |
| 4321 | SAB(s)bc | 3.46 | -21.91 |
| 5055 | SA(rs)bc | 6.15 | -21.34 |
| 5194 | SA(s)bcp | 5.48 | -21.6 |
| 5248 | SAB(rs)bc | 3.23 | -21.19 |
| 5457 | SAB(rs)cd | 13.45 | -21.51 |
| 6912 | SB(s)c | 0.79 | -21.75[1] |
| 6946 | SAB(rs)cd | 5.48 | -20.3 |
| 7793 | SA(s)d | 4.56 | -18.85 |
| IC 342 | SAB(rs)cd | 8.89 | -20.43[2] |

[1] This is an estimate based on distance and angular size.

[2] Based on $V_0 = 228$km s$^{-1}$ and $B_T^0 = 7.86$ from de Vaucouleurs, de Vaucouleurs and Corwin (1976), and $H = 50$km s$^{-1}$Mpc$^{-1}$.

Table 2: Theoretical Ratios of Resonance Radii

| Name | $\alpha$ | $\frac{R_{ILR}}{R_{OLR}}$ | $\frac{R_{1/3}}{R_{OLR}}$ | $\frac{R_{1/4}}{R_{OLR}}$ | $\frac{R_{CR}}{R_{OLR}}$ | $\frac{R_{3/4}}{R_{OLR}}$ | $\frac{R_{OLR}}{R_{1/2}}$ |
|---|---|---|---|---|---|---|---|
| NGC 157 | 0.046 | 0.15[1] | 0.28 | 0.35 | 0.57 | 0.85 | 3.01 |
| 598 | 0.31 | 0.038 | 0.14 | 0.20 | 0.42 | 0.79 | 5.79 |
| 613 | 0.042 | 0.15 | 0.29 | 0.36 | 0.57 | 0.86 | 2.99 |
| 628 | 0.15 | 0.10 | 0.22 | 0.29 | 0.51 | 0.83 | 3.71 |
| 1232 | 0.015 | 0.16 | 0.30 | 0.37 | 0.58 | 0.86 | 2.85 |
| 1300 | 0.00 | 0.17 | 0.31 | 0.38 | 0.59 | 0.86 | 2.78 |
| 3031 | -0.20 | 0.29 | 0.42 | 0.49 | 0.67 | 0.89 | 2.12 |
| 3938 | 0.19 | 0.082 | 0.21 | 0.27 | 0.50 | 0.83 | 4.02 |
| 4254 | 0.17 | 0.087 | 0.21 | 0.28 | 0.50 | 0.83 | 3.91 |
| 4321 | 0.14 | 0.10 | 0.23 | 0.30 | 0.52 | 0.84 | 3.62 |
| 5055 | 0.00 | 0.17 | 0.31 | 0.38 | 0.59 | 0.86 | 2.78 |
| 5194 | -0.16 | 0.26 | 0.40 | 0.46 | 0.65 | 0.89 | 2.22 |
| 5248 | 0.13 | 0.11 | 0.24 | 0.31 | 0.53 | 0.84 | 3.55 |
| 5457 | 0.10 | 0.12 | 0.25 | 0.32 | 0.54 | 0.84 | 3.35 |
| 6912 | 0.083 | 0.13 | 0.26 | 0.33 | 0.55 | 0.85 | 3.22 |
| 6946 | 0.21 | 0.074 | 0.19 | 0.26 | 0.49 | 0.82 | 4.23 |
| 7793 | 0.33 | 0.033 | 0.13 | 0.19 | 0.42 | 0.78 | 6.20 |
| IC 342 | 0.19 | 0.078 | 0.20 | 0.27 | 0.49 | 0.82 | 4.11 |

[1] The positions for the inner Lindblad resonances assume that the rotation curve has the same power law form this close to the center, which is very unlikely. The real ILRs could have positions that differ in radius by a factor of 2 or more; there may not even be an ILR. This entry is given here only for rough comparisons with the inner extents of the spirals.

Note: $\alpha$ for NGC 1300, 4321, 4254, and 5055 are directly from the values of $\Delta$ and not $M_n$ in Persic and Salucci (1991); $\alpha$ for NGC 628, NGC 3031, and NGC 5194 are from the rotation curves in Wevers (1984), Visser (1980), and Tully (1974).

Table 3: Resonance Fits in Units of $R_{25}$

| Name | $R_{i3}$ | $R_{i4}$ | $R_{CR}$ | $R_{O3}$ | $R_{O2}$ |
|---|---|---|---|---|---|
| NGC 157 | 0.22 | 0.27 | 0.44 | 0.65 | 0.77 |
| 598 | 0.13 | 0.19 | 0.40 | 0.75 | 0.95 |
| 613 | 0.26 | 0.32 | 0.51 | 0.77 | 0.9 |
| 628 | 0.20 | 0.26 | 0.46 | 0.75 | 0.9 |
| 1232 | 0.27 | 0.34 | 0.53 | 0.78 | 0.91 |
| 1300 | 0.27 | 0.34 | 0.52 | 0.76 | 0.88 |
| 3031 | 0.38 | 0.44 | 0.6 | 0.8 | 0.9 |
| 3938 | 0.23 | 0.30 | 0.55 | 0.91 | 1.1 |
| 4254 | 0.23 | 0.3 | 0.54 | 0.9 | 1.08 |
| 4321 | 0.25 | 0.35[1] | 0.57 | 0.92 | 1.1 |
| 5055 | 0.24 | 0.29 | 0.45 | 0.65 | 0.76 |
| 5194[2] | 0.20 | 0.25 | 0.4 | 0.51 | 0.56 |
| 5248 | 0.24 | 0.31 | 0.53 | 0.84 | 1. |
| 5457 | 0.19 | 0.24 | 0.41 | 0.63 | 0.75 |
| 6912 | 0.37 | 0.47 | 0.78 | 1.2 | 1.41 |
| 6946 | 0.18 | 0.25 | 0.47 | 0.78 | 0.95 |
| 7793 | 0.13 | 0.19 | 0.42 | 0.79 | 1.01 |
| IC 342 | 0.28 | 0.37 | 0.68 | 1.13 | 1.38 |

[1] This value is from EES, and sensible considering the spurs at this location, but it differs slightly from the value expected from Table 2, which is $0.33R_{25}$ for an OLR at $1.1R_{25}$.

[2] For NGC 5194, the resonance radii are from the rotation curve in Tully (1974), not from the approximation using $\alpha$ nor from the ratios of resonances in Table 2.

Table 4: Resonance Features in Galaxies

| Name | inner circle(C) bar(B) or spiral(S)? | inner triangle? | 4:1 spur? | SF ridge ending at CR? | spiral arm endpt at OLR? | inner limit of $S_3$ at inner 3:1? | outer limit of $S_3$ at outer 3:1? |
|---|---|---|---|---|---|---|---|
| NGC 157 | B | Y | N | Y | Y | Y | Y |
| 598 | B | Y | N | Y[1] | Y | Y | Y |
| 613 | B | Y | N | N | Y | Y | Y |
| 628 | S | Y | Y | Y | Y | Y | Y |
| 1232 | S | N | N | Y | Y | Y | Y |
| 1300 | B | Y | N | Y | Y | Y | Y |
| 3031 | C | N | Y | N | Y | Y | Y |
| 3938 | C | N | N | Y | Y | N[2] | N[2] |
| 4254 | B | N | N | Y | Y | Y | Y |
| 4321 | C | Y | Y | Y | Y | Y | Y |
| 5055 | S | N | N | N | N | Y | N |
| 5194 | S/B | Y | Y | Y | Y[3] | Y | Y |
| 5248 | S/B | N | N[4] | Y | Y | Y | Y |
| 5457 | S/B | Y | Y | Y | Y | Y | Y |
| 6912 | C | N | N | N | Y | Y | Y |
| 6946 | C/S[5] | N | N | Y | Y | Y | Y |
| 7793 | C | Y | N | N | Y | N | Y |
| IC 342 | C | N | N | Y[1] | Y | Y | Y |

[1] There is at least one star formation ridge ending at corotation in these galaxies but there are other star formation ridges too, so no ridge is a clear indicator of corotation.

[2] There is no 3:1 fit here, but the five-arm structure fits between the inner and outer 5:1 resonances. This galaxy probably contains a global five-arm spiral wave.

[3] The main spiral arms in this galaxy, especially in the near-infrared, end at the OLR, but bright, presumably tidal, arms go out further.

[4] There is a bright spur or radially extended star-formation feature at the 4:1 resonance radius, but it is unusual and not considered a spur as in the other galaxies.

[5] There is a one-arm spiral in the inner region.

Fig. 1.— (a-r) - Enhanced images of the galaxies, with the sky-enhanced view in the top left, the three-fold symmetric image, $S_3$ in the top right, the two-fold symmetric image, $S_2$ in the middle left, the two-fold antisymmetric image, $A_2$, in the middle right, $S_2$ again in the lower left with circles indicating suggested resonances at the inner 4:1, corotation and outer Lindblad resonances in order of increasing radius, and $S_3$ again in the lower right with circles indicating suggested resonances at the inner and outer 3:1 resonances. The radii of the circles are in the proportions given in Table 2 by the theory of wave-epicycle resonances, assuming power-law rotation curves appropriate to the galaxy. The order of the figures is by NGC number, from a to r, as listed in the tables. This figure, (a), is NGC 157.

Fig. 1.— b - NGC 598

Fig. 1.— c - NGC 613

Fig. 1.— d - NGC 628

Fig. 1.— e - NGC 1232

Fig. 1.— f - NGC 1300

Fig. 1.— g - NGC 3031

Fig. 1.— h - NGC 3938

Fig. 1.— i - NGC 4254

Fig. 1.— j - NGC 4321

Fig. 1.— k - NGC 5055

Fig. 1.— l - NGC 5194

Fig. 1.— m - NGC 5248

Fig. 1.— n - NGC 5457

Fig. 1.— o - NGC 6912

Fig. 1.— p - NGC 6946

Fig. 1.— q - NGC 7793

Fig. 1.— r - IC 342

Fig. 2.— a-r - Galaxy images in angular coordinates with the logarithm of the radius in the vertical direction, from $0.1R_{25}$ to $1.0R_{25}$ with tic marks at each $0.1R_{25}$, and the azimuthal angle in the horizontal direction, from 0 to $4\pi$. with tic marks at each $\pi$. Four images are given for each galaxy, with three galaxies on a page. The images are: sky enhanced on the top left, $S_3$ top right, $S_2$ bottom left and $A_2$ bottom right. On this page are from top to bottom NGC 157, NGC 598 ,and NGC 613

Fig. 2.— (d) NGC 628 (top), (e) NGC 1232 (middle), (f) NGC 1300 (bottom)

Fig. 2.— (g) NGC 3031-(top), (h) NGC 3938-(middle), (i) NGC 4254 (bottom)

Fig. 2.— (j) NGC 4321 (top), (k) NGC 5055-(middle), (l) NGC 5194 (bottom)

Fig. 2.— (m) NGC 5248 (top), (n) NGC 5457 (middle), (o) NGC 6912 (bottom)

Fig. 2.— (p) NGC 6946 (top), (q) NGC 7793 (middle), (r) IC 342 (bottom)

Fig. 3.— NGC 3938 images with 4-left, 5, and 6 fold symmetry, and circles indicating the 4:1, 5:1 and 6:1 resonances, respectively. This multiple arm galaxy is apparently dominated by structure with $\sim$ 5 semi-regular arms.

Fig. 4.— Fourier Transform powers in logarithmic coordinates are plotted versus the radii in units of the galaxy size, $R_{25}$, for the $m = 2$ (solid lines) and $m = 3$ (dashed lines) components. Usually the $m = 2$ component dominates the total power, but occasionally the $m = 3$ component is larger over a range of radii.

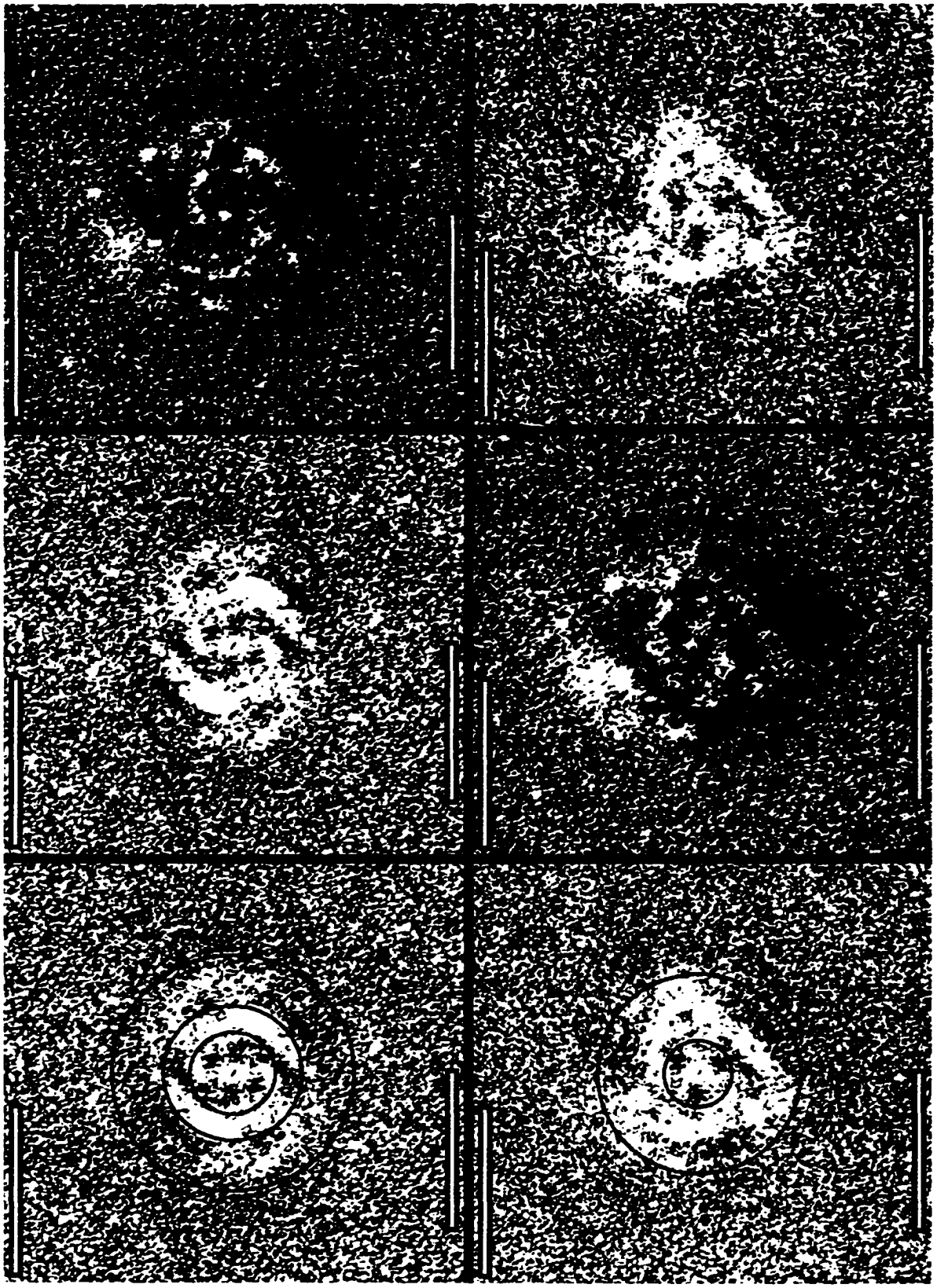

FIG. 1.—(*a–r*) Enhanced images of the galaxies, with the sky-enhanced view in the top left, the three-fold symmetric image, $S_3$, in the top right, the two-fold symmetric image, $S_2$, in the middle left, the two-fold antisymmetric image, $A_2$, in the middle right, $S_2$ again in the lower left with circles indicating suggested resonances at the inner 4:1, corotation and outer Lindblad resonances in order of increasing radius, and $S_3$ again in the lower right with circles indicating suggested resonances at the inner and outer 3:1 resonances. The radii of the circles are in the proportions given in Table 2 by the theory of wave-epicycle resonances, assuming power-law rotation curves appropriate to the galaxy. The order of the figures is by NGC number, from (*a*) to (*r*) as listed in the tables. This figure, (*a*), is NGC 157.

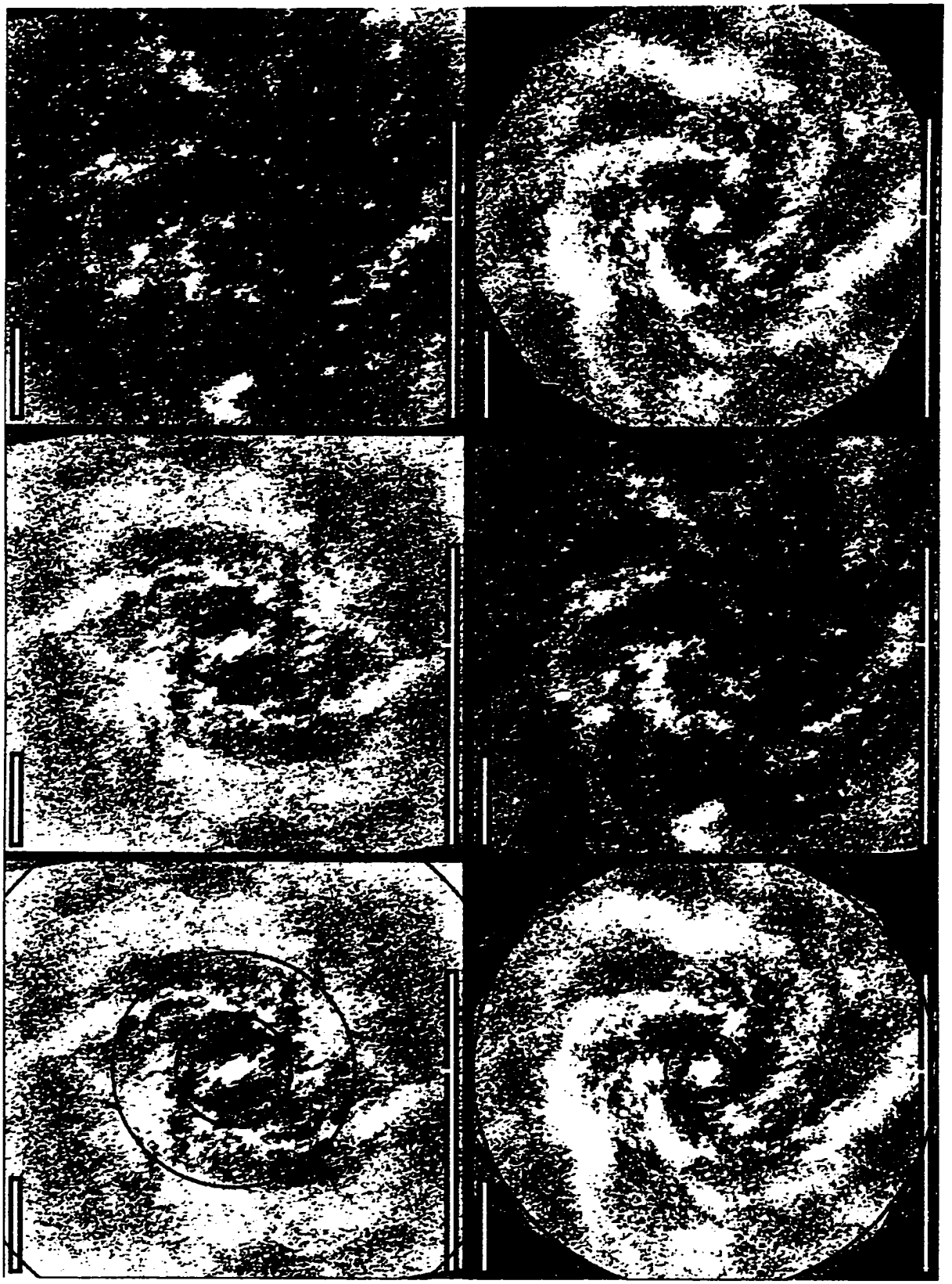

FIG. 1.—(*b*) NGC 598

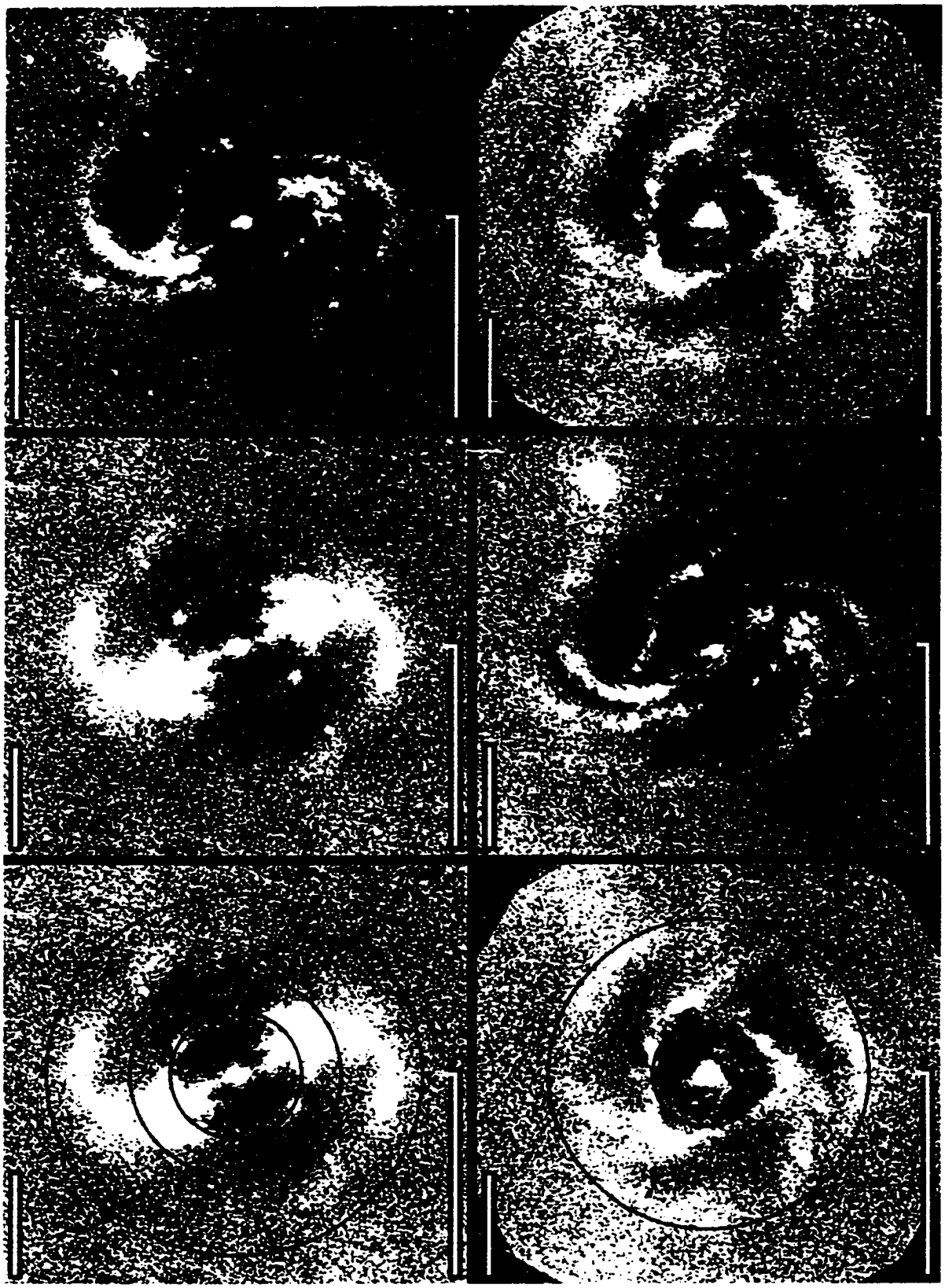

FIG. 1.—(*c*) NGC 613

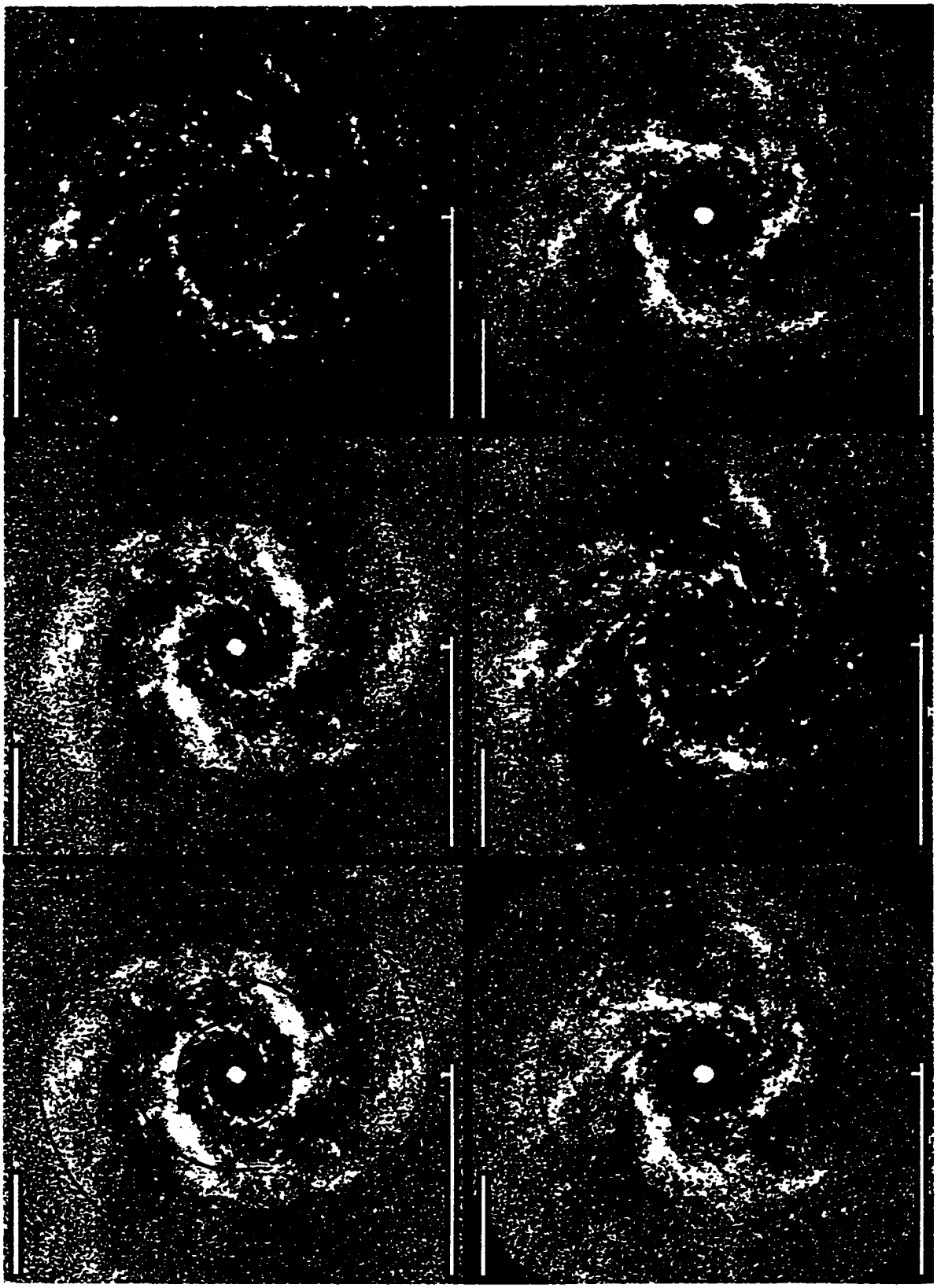

FIG. 1.—(*d*) NGC 628

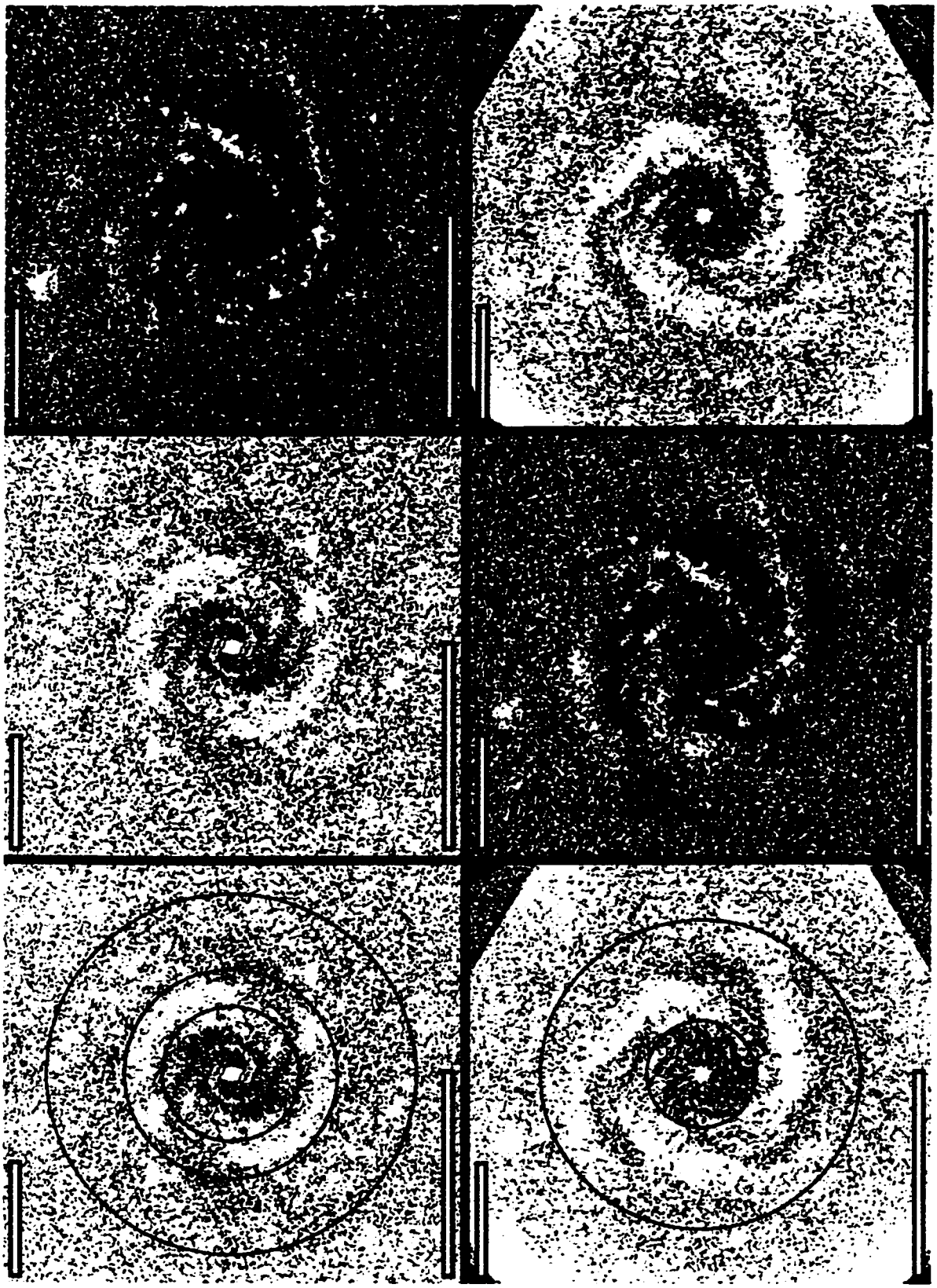

FIG. 1.—(*e*) NGC 1232

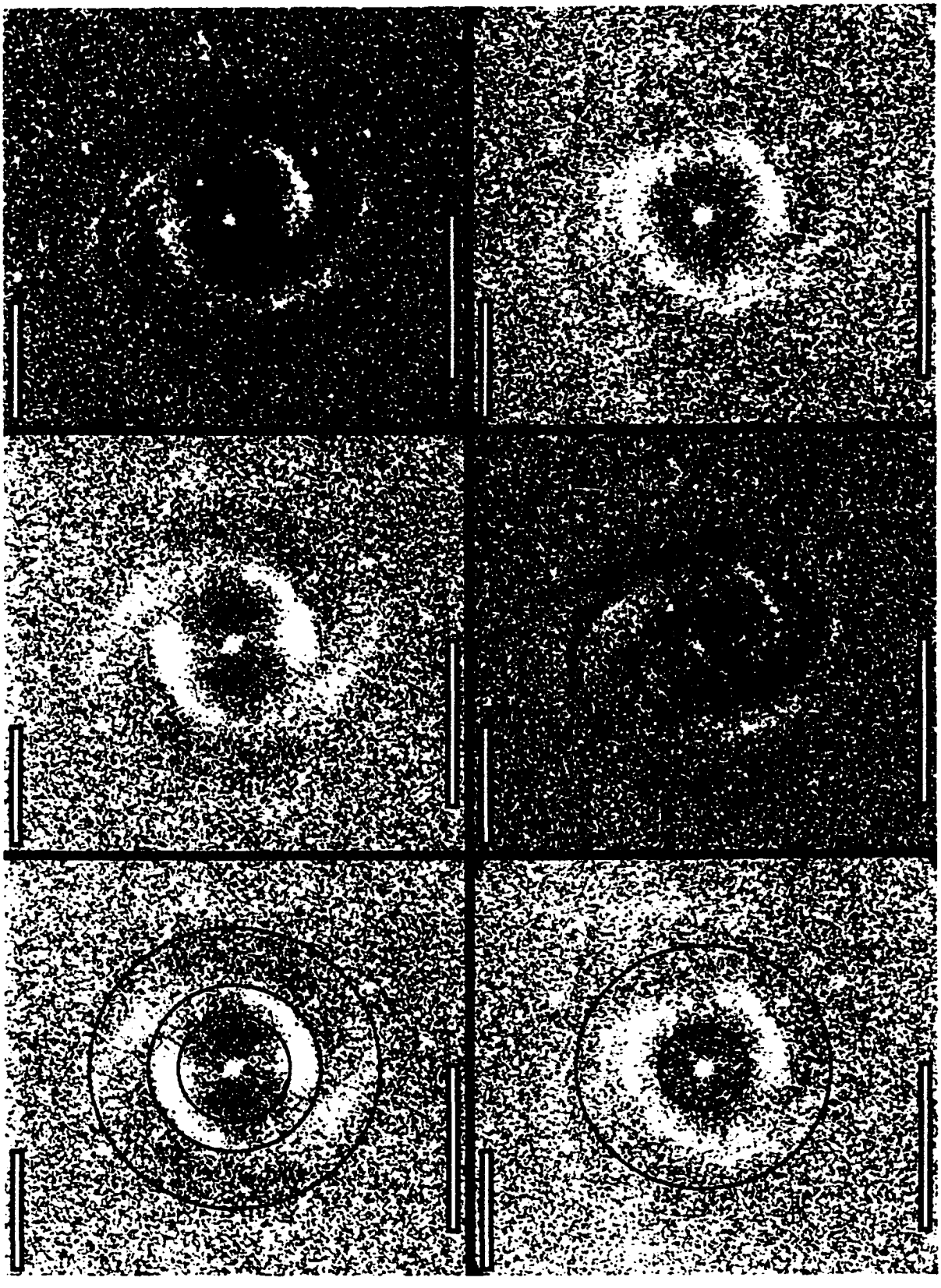

FIG. 1.—(*f*) NGC 1300

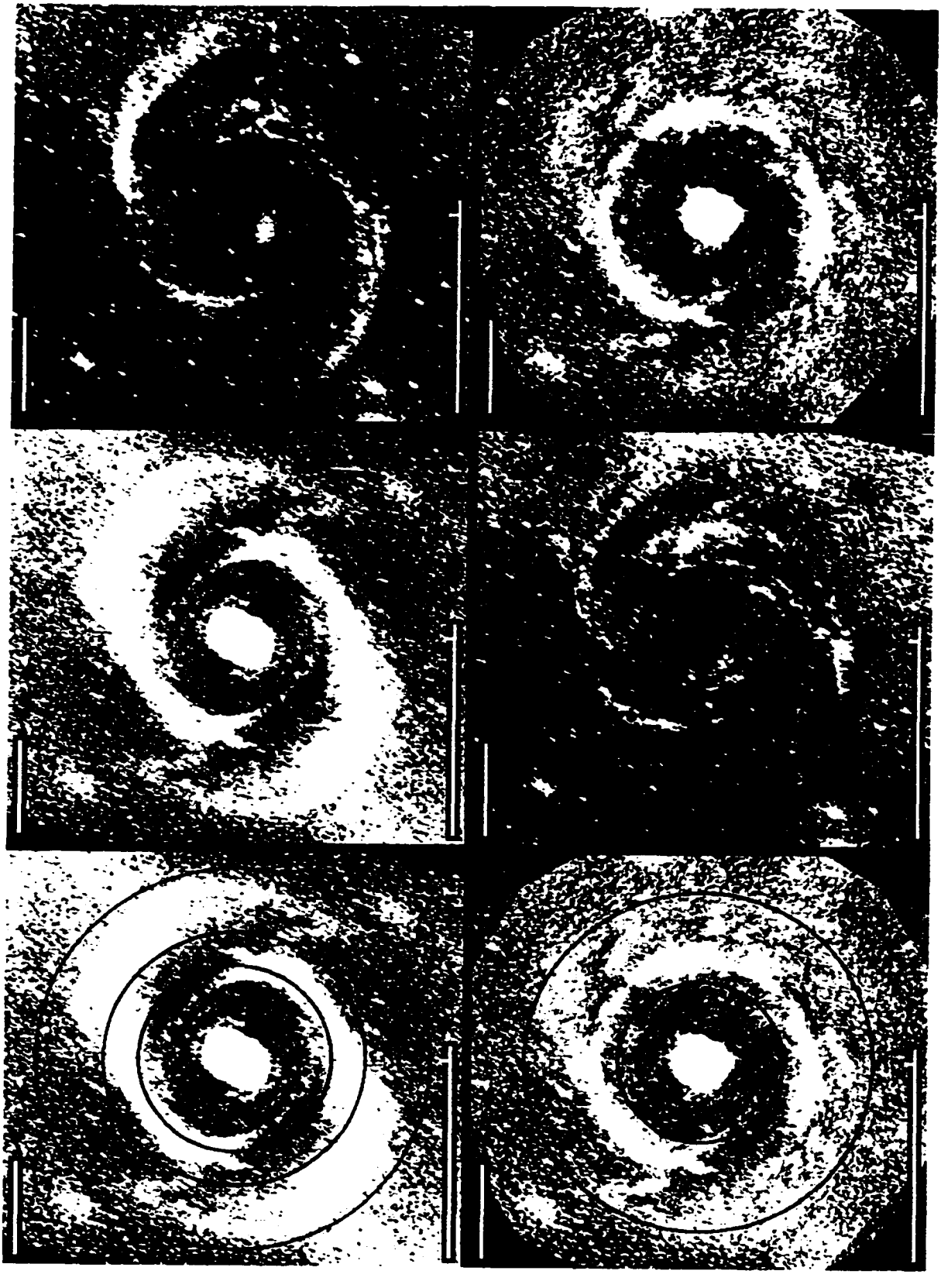

FIG. 1.—(*g*) NGC 3031

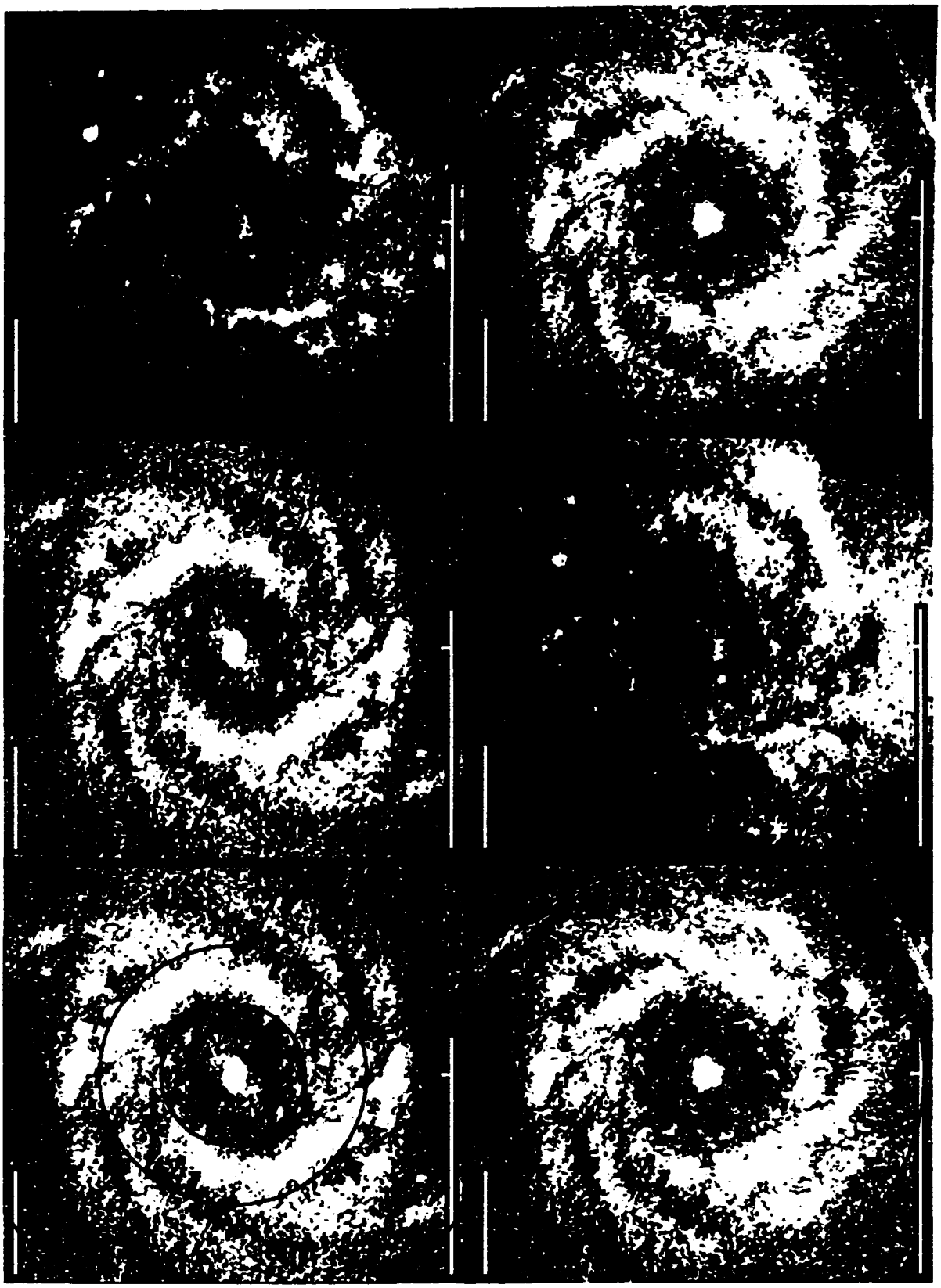

FIG. 1.—(*h*) NGC 3938

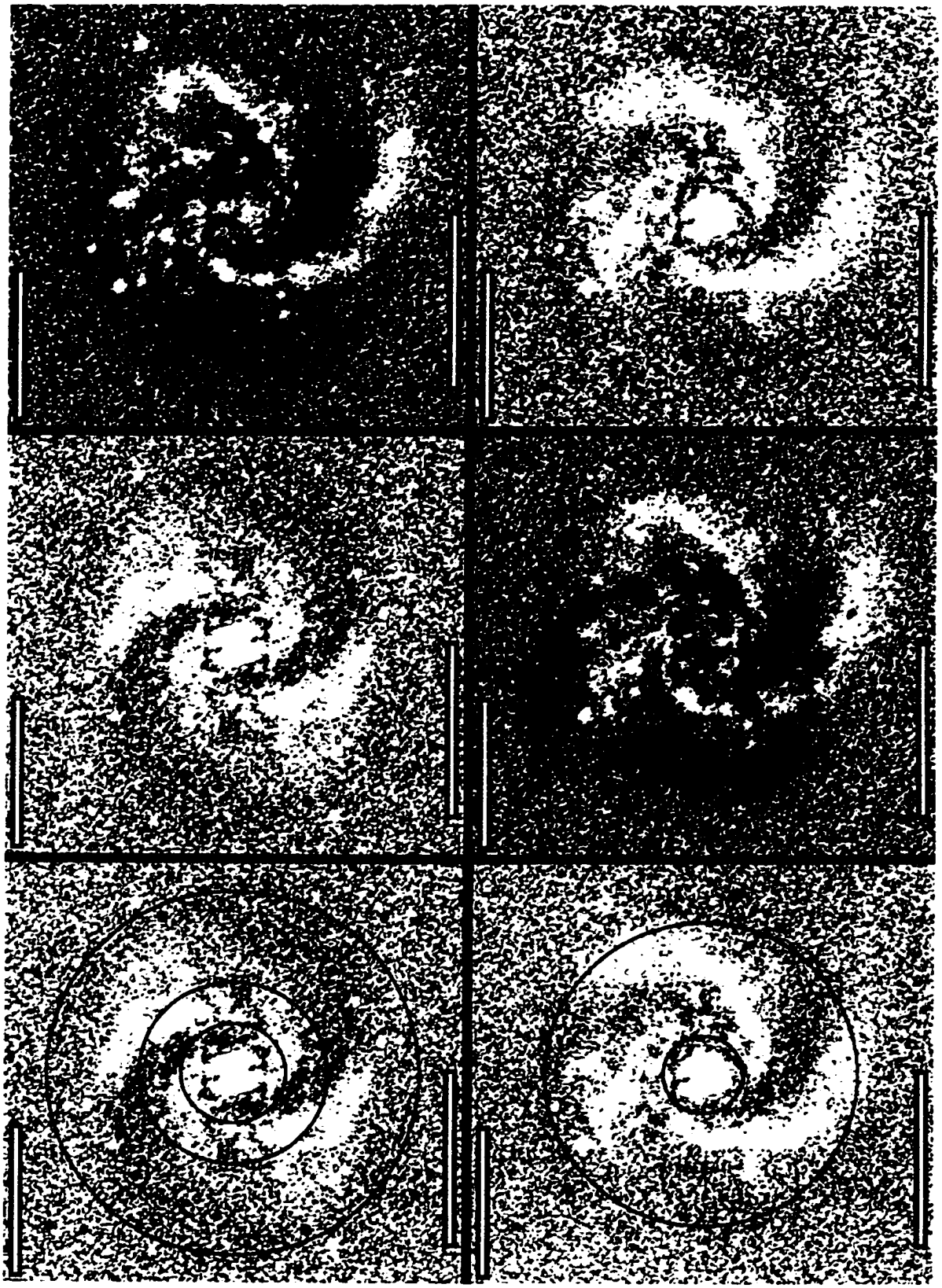

FIG. 1.—(*i*) NGC 4254

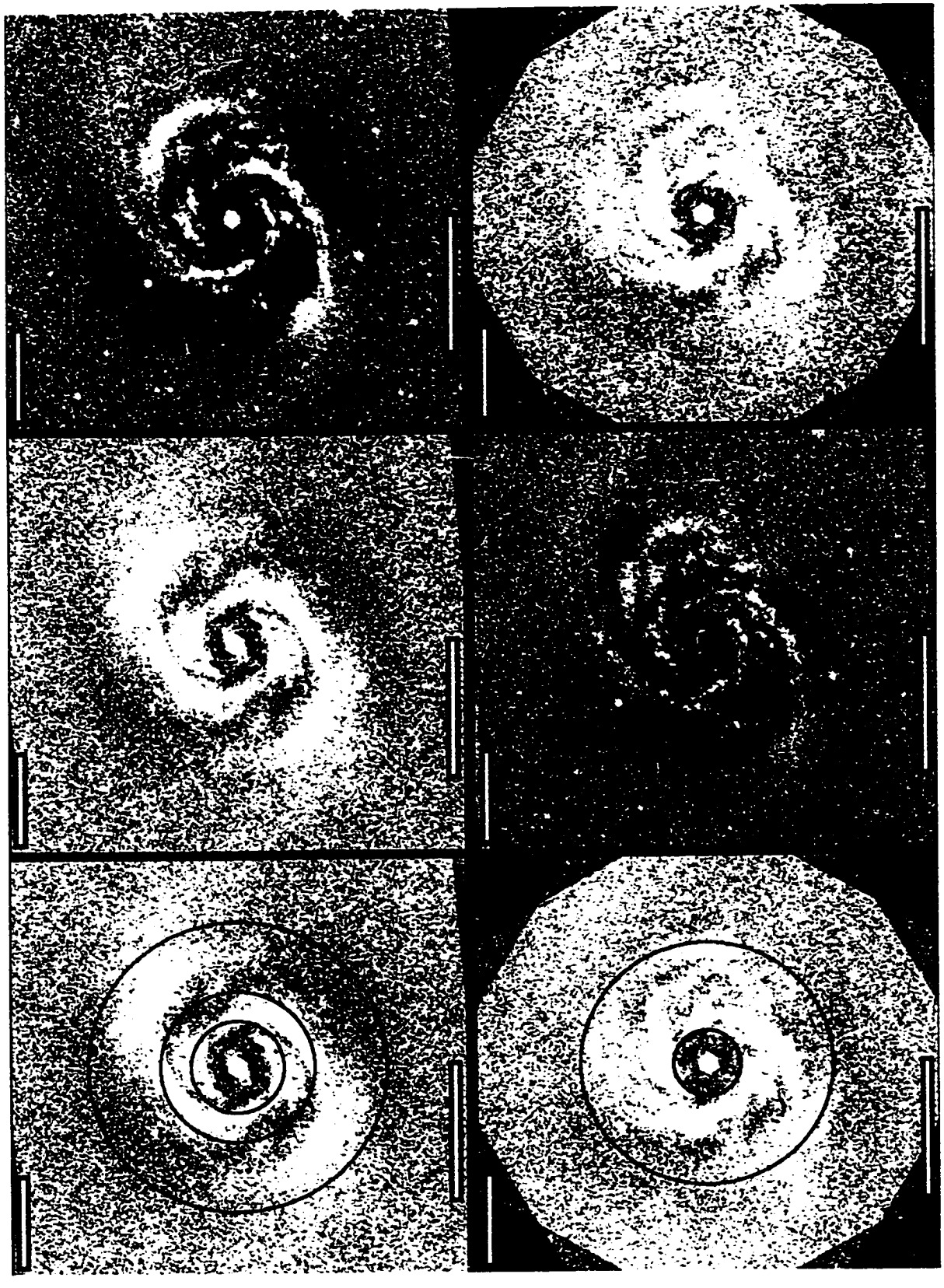

FIG. 1.—(*j*) NGC 4321

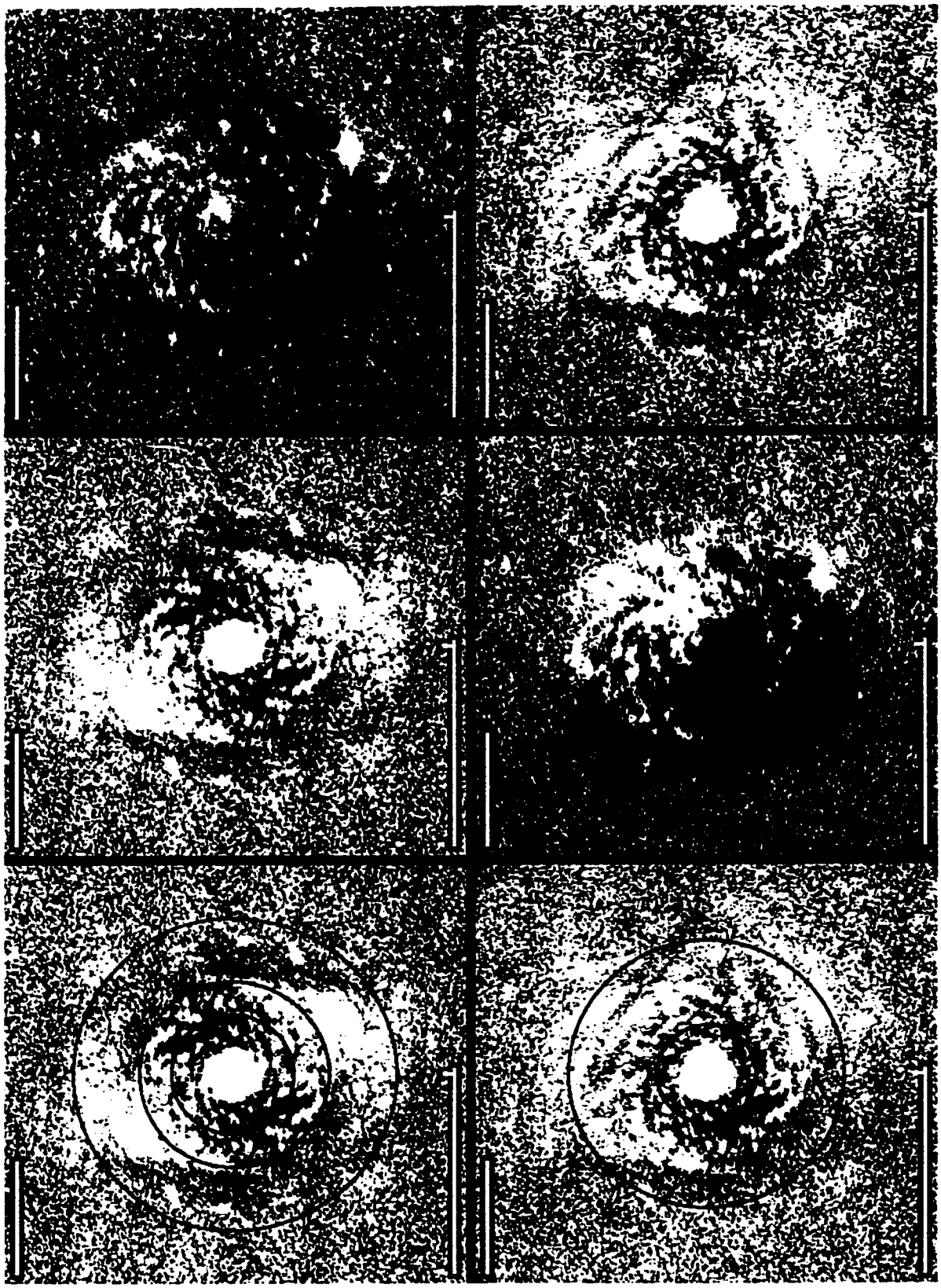

FIG. 1.—(*k*) NGC 5055

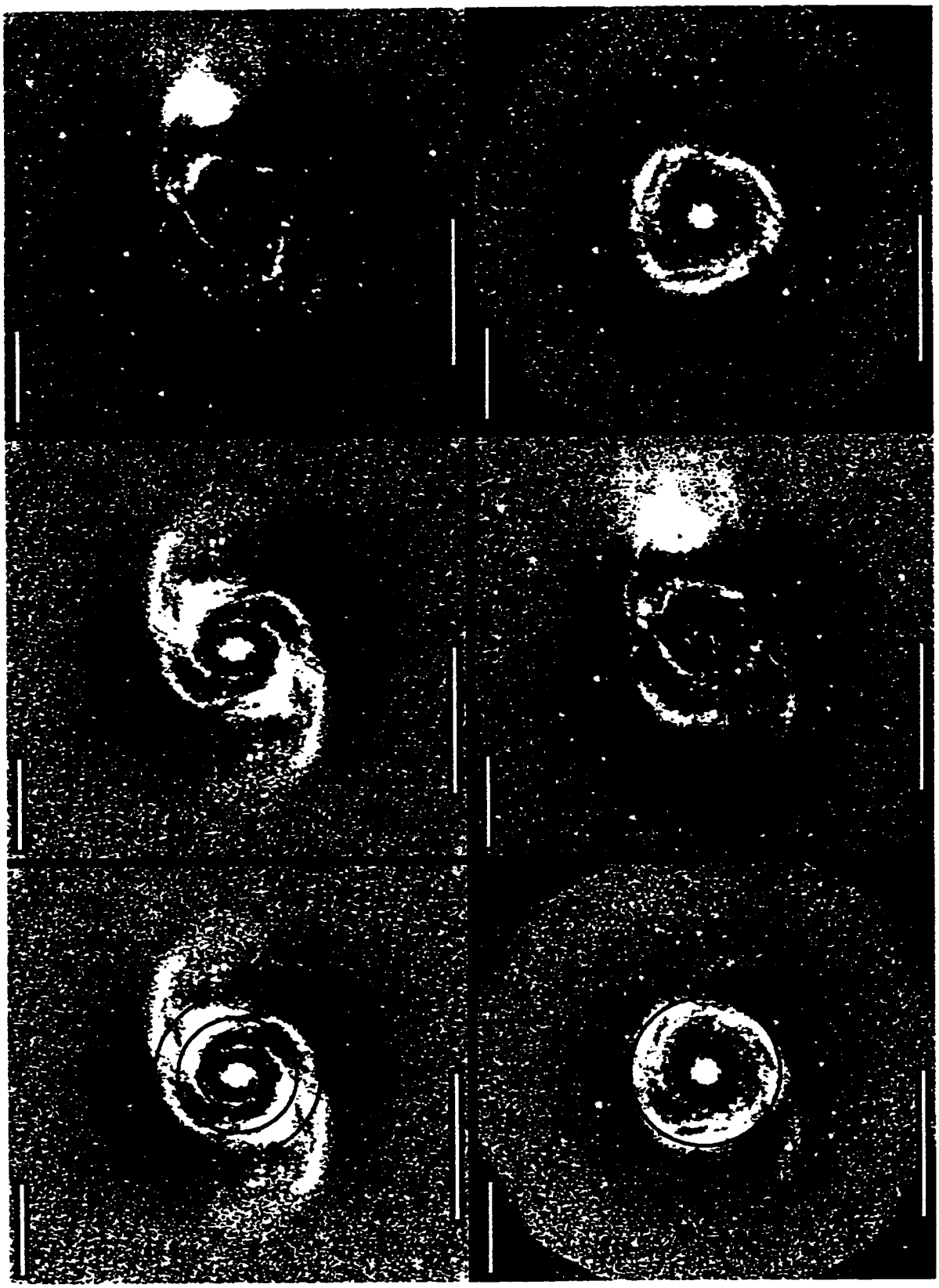

FIG. 1.—(*l*) NGC 5194

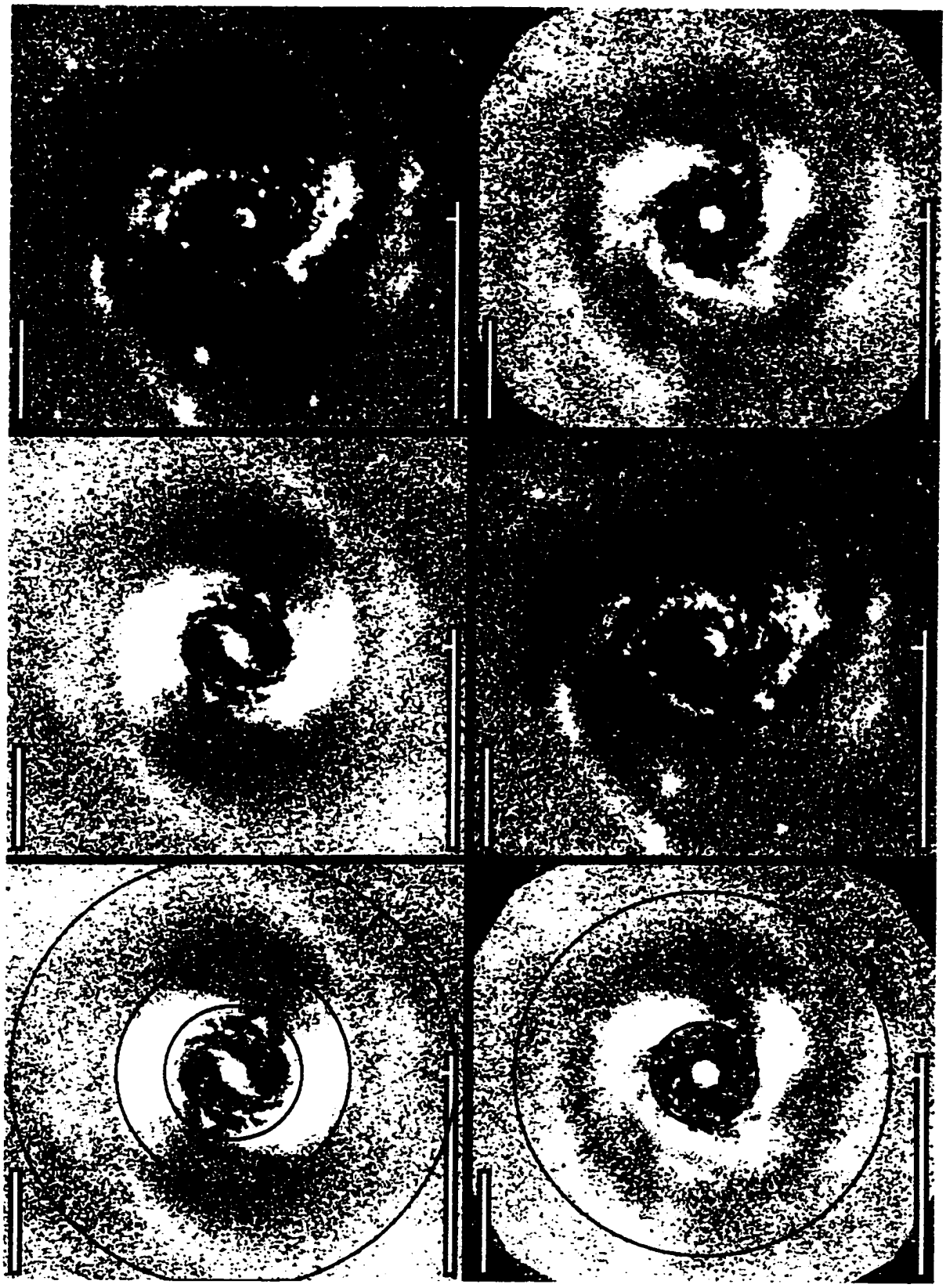

FIG. 1.—(*m*) NGC 5248

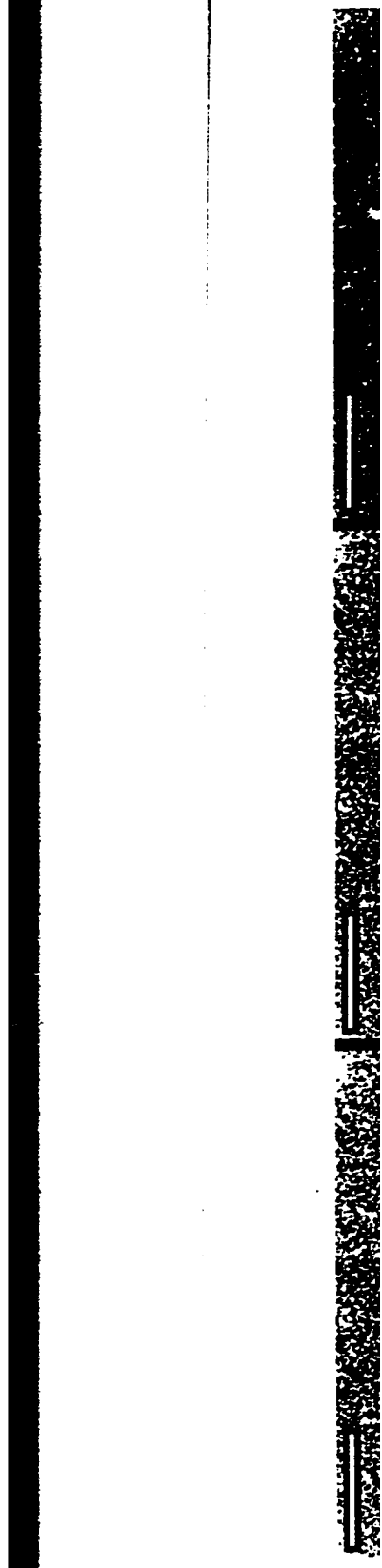

ELMEGREEN, ELM

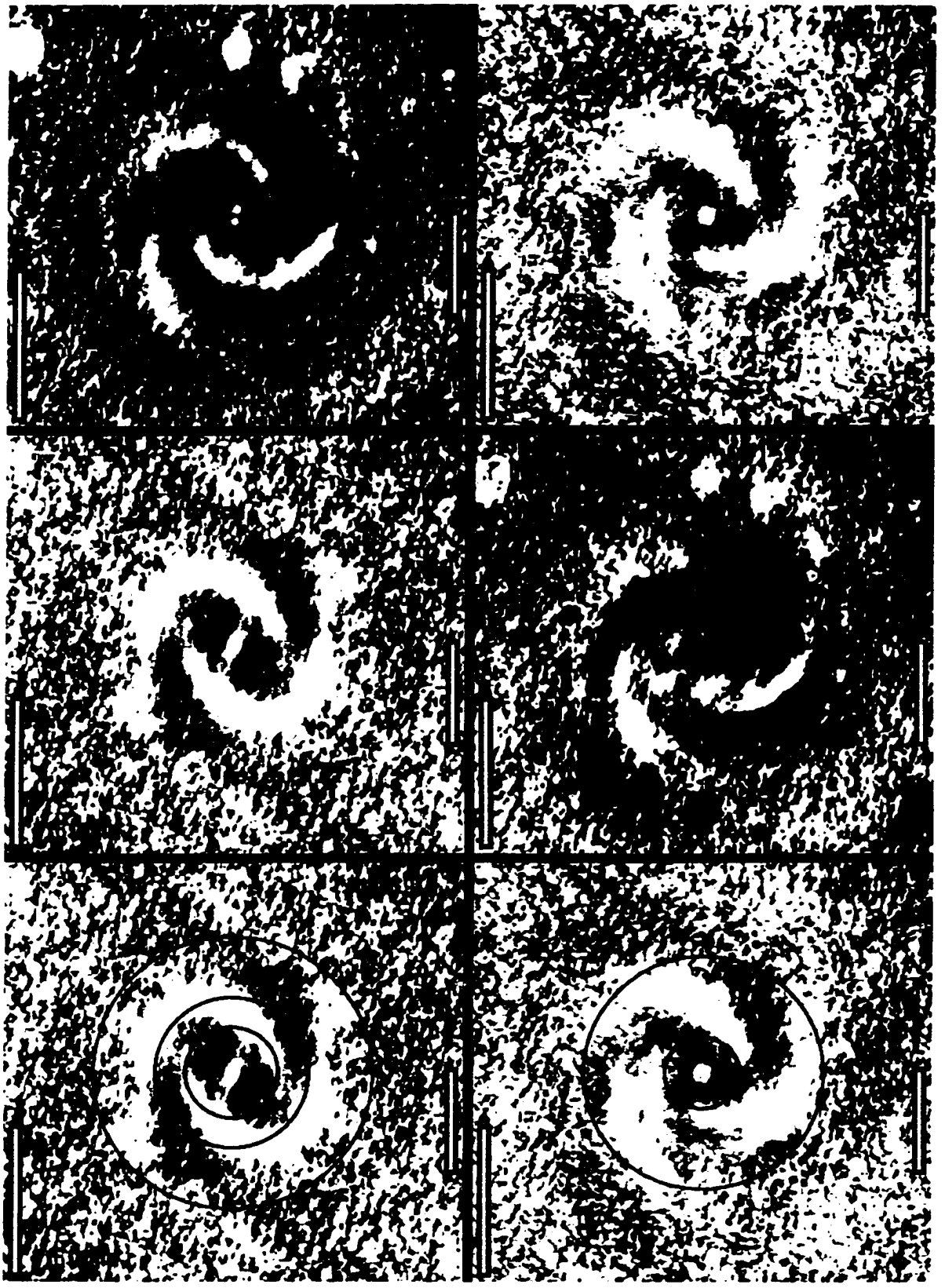

FIG. 1.—(*a*) NGC 6912

ELMEGREEN, ELMEGREEN, & M

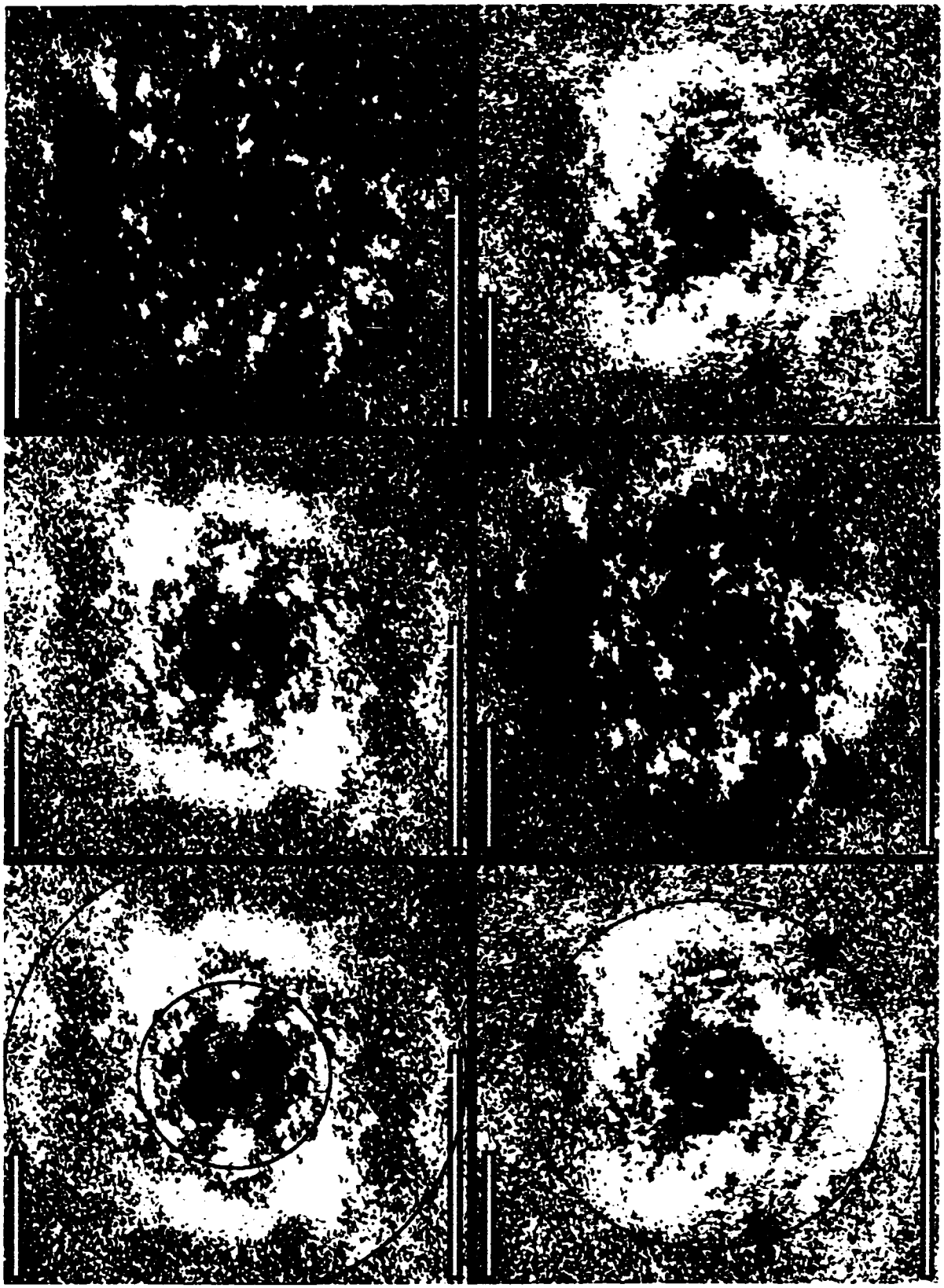

FIG. 1.—(*q*) NGC 7793

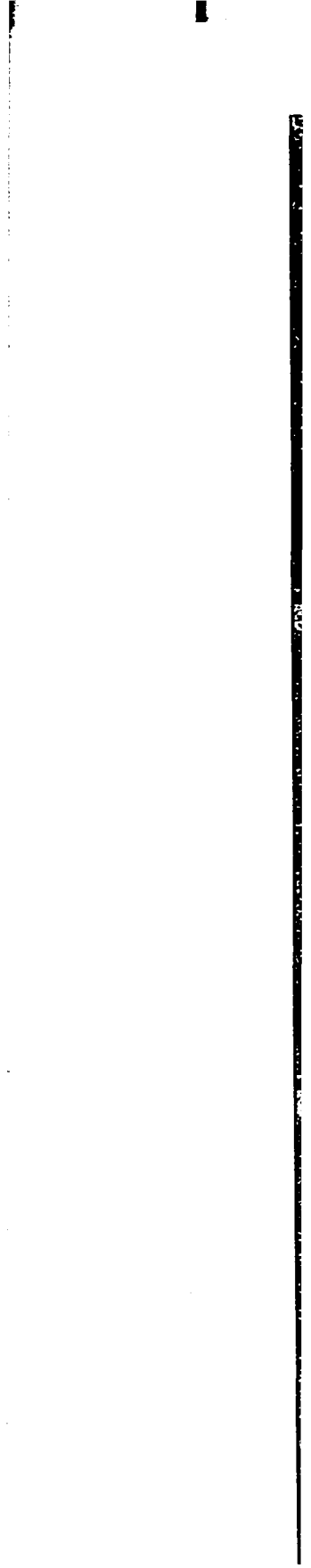

ELMEGREEN.

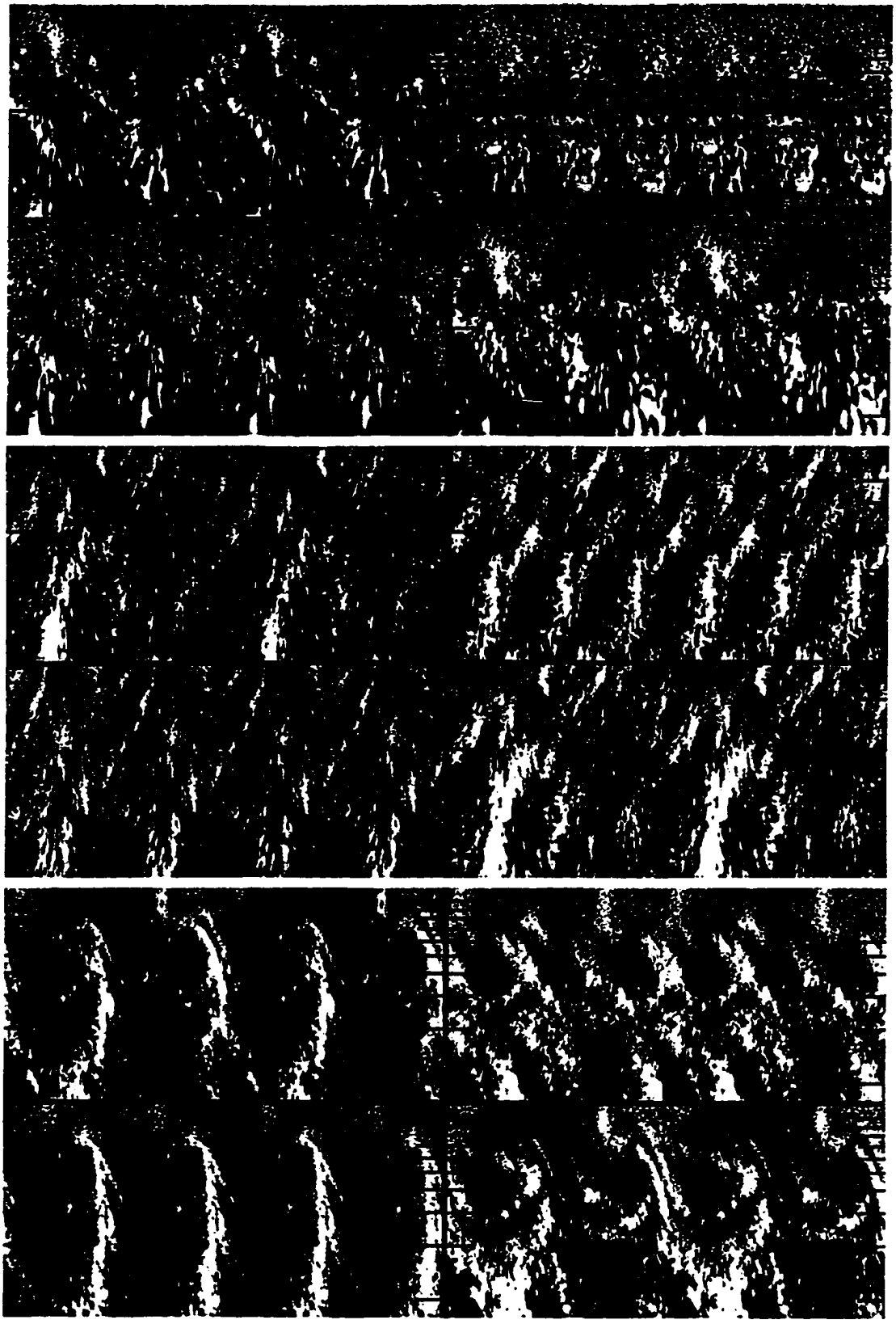

FIG. 2.—(*a–r*) Galaxy images in angular coordinates with the logarithm of the radius in the vertical direction, from 0.1 $R_{25}$ to 1.0 $R_{25}$ with tic marks at each 0.1 $R_{25}$, and the azimuthal angle in the horizontal direction, from 0 to $4\pi$ with tic marks at each $\pi$. Four images are given for each galaxy, with three galaxies on a page. The images are (*top left*) sky enhanced; $S_3$, *top right*; $S_2$, *bottom left*; and $A_2$, *bottom right*. On this page are (*a*) NGC 157 (*top*), (*b*) NGC 598 (*middle*), (*c*) NGC 613 (*bottom*).

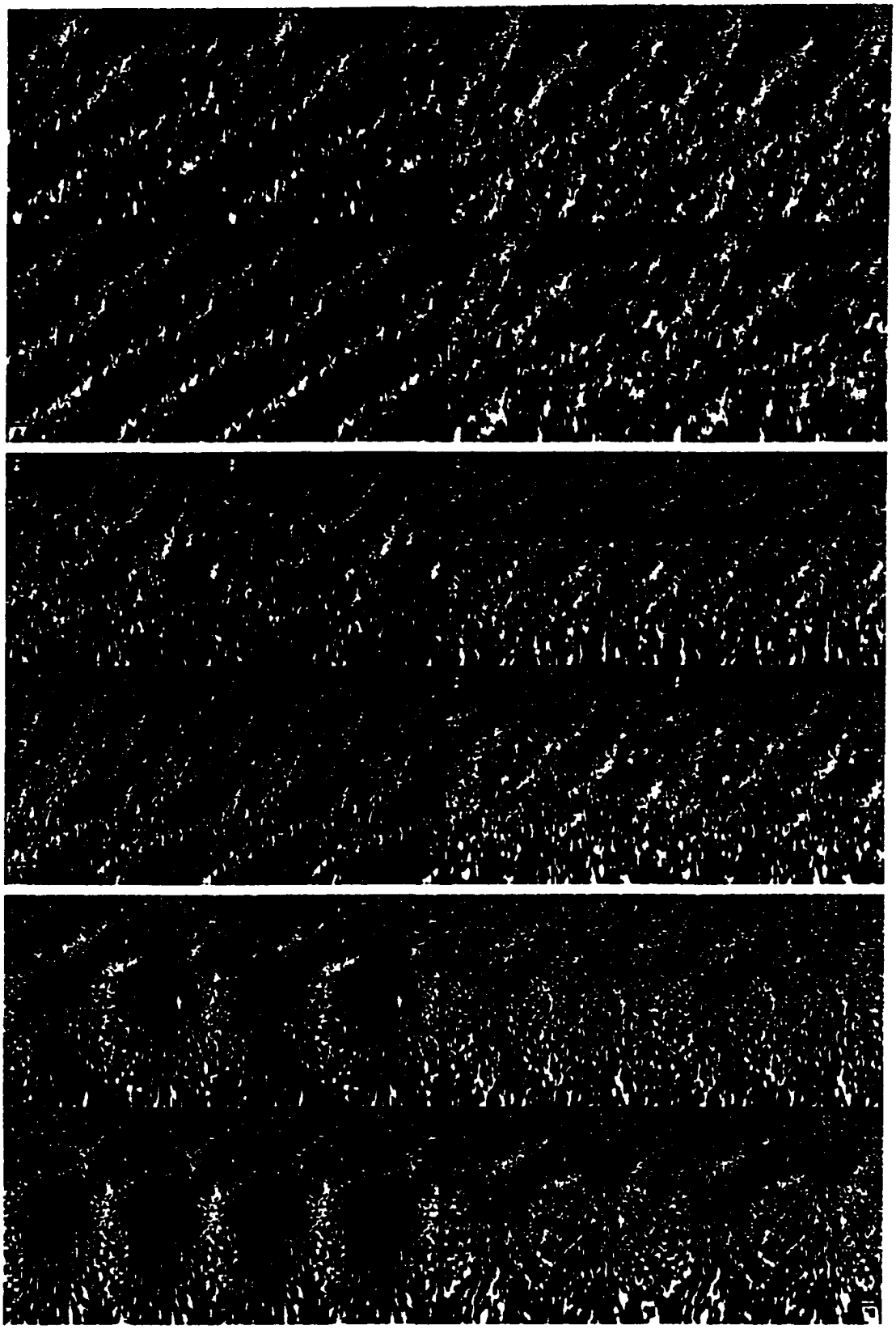

FIG. 2.—(*d*) NGC 628 (*top*), (*e*) NGC 1232 (*middle*), (*f*) NGC 1300 (*bottom*)

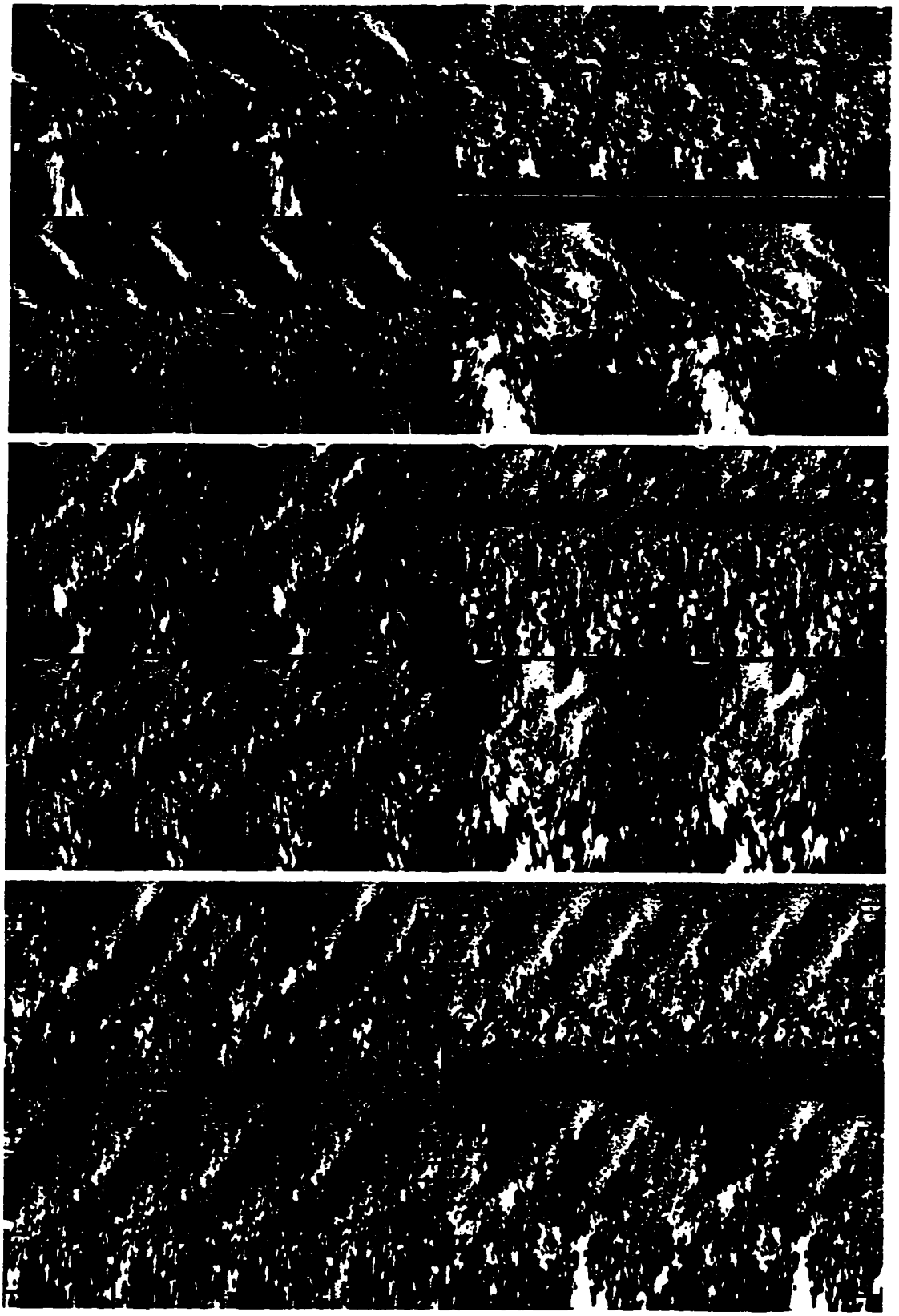

FIG. 2.—(*g*) NGC 3031 (*top*), (*h*) NGC 3938 (*middle*), (*i*) NGC 4254 (*bottom*)

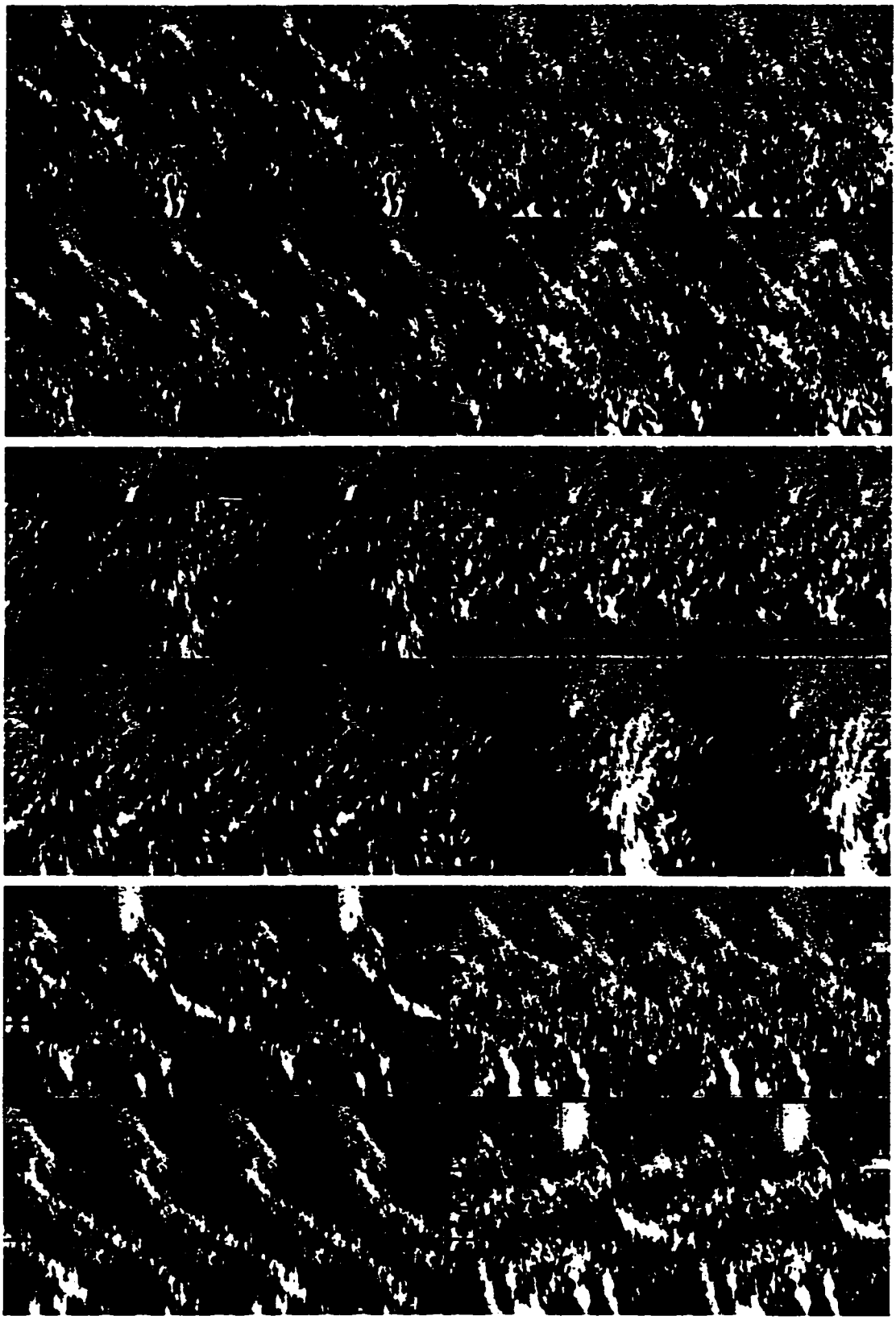

FIG. 2.—(*j*) NGC 4321 (*top*), (*k*) NGC 5055 (*middle*), (*l*) NGC 5194 (*bottom*)

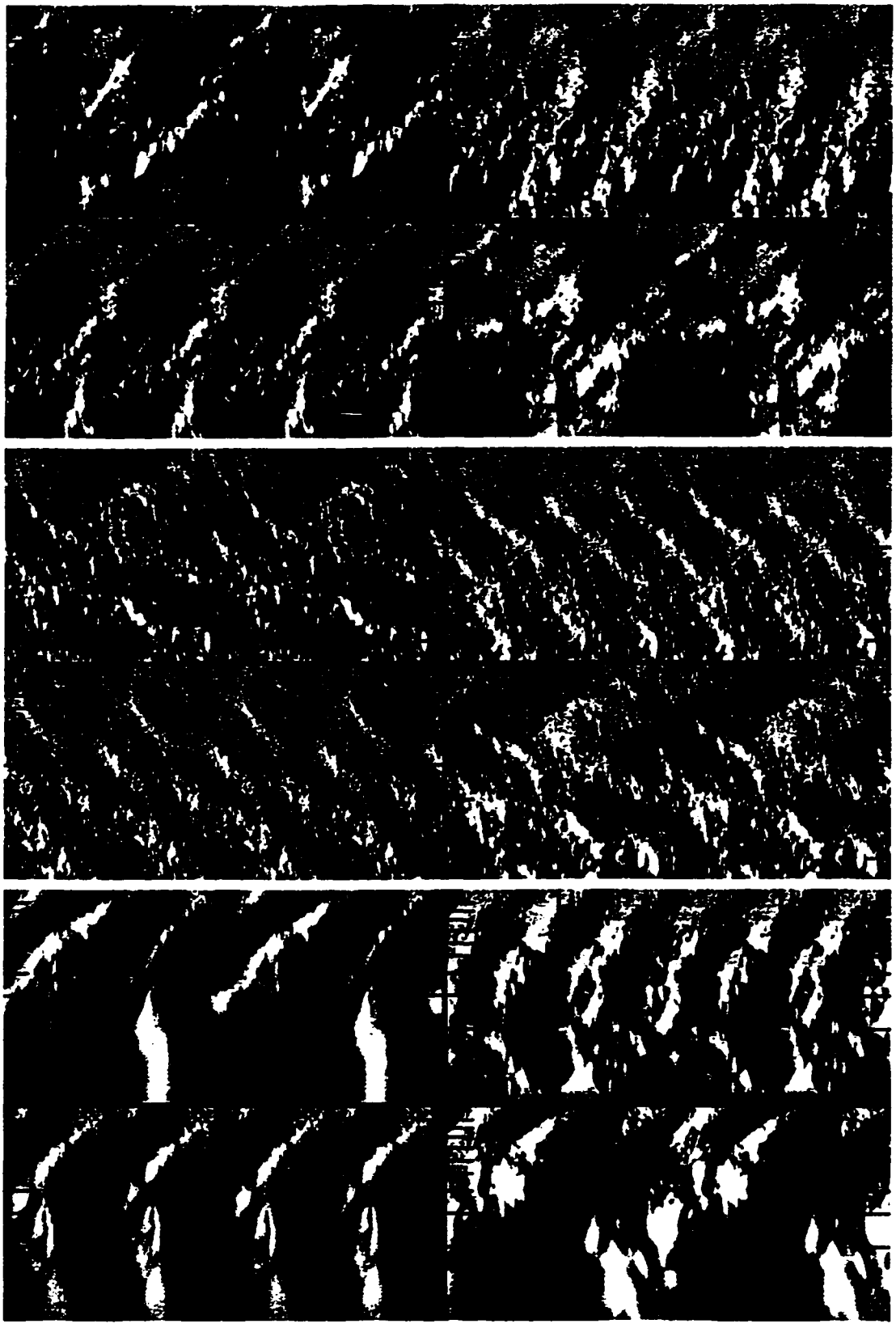

FIG. 2.—(*m*) NGC 5248 (*top*), (*n*) NGC 5457 (*middle*), (*o*) NGC 6912 (*bottom*)

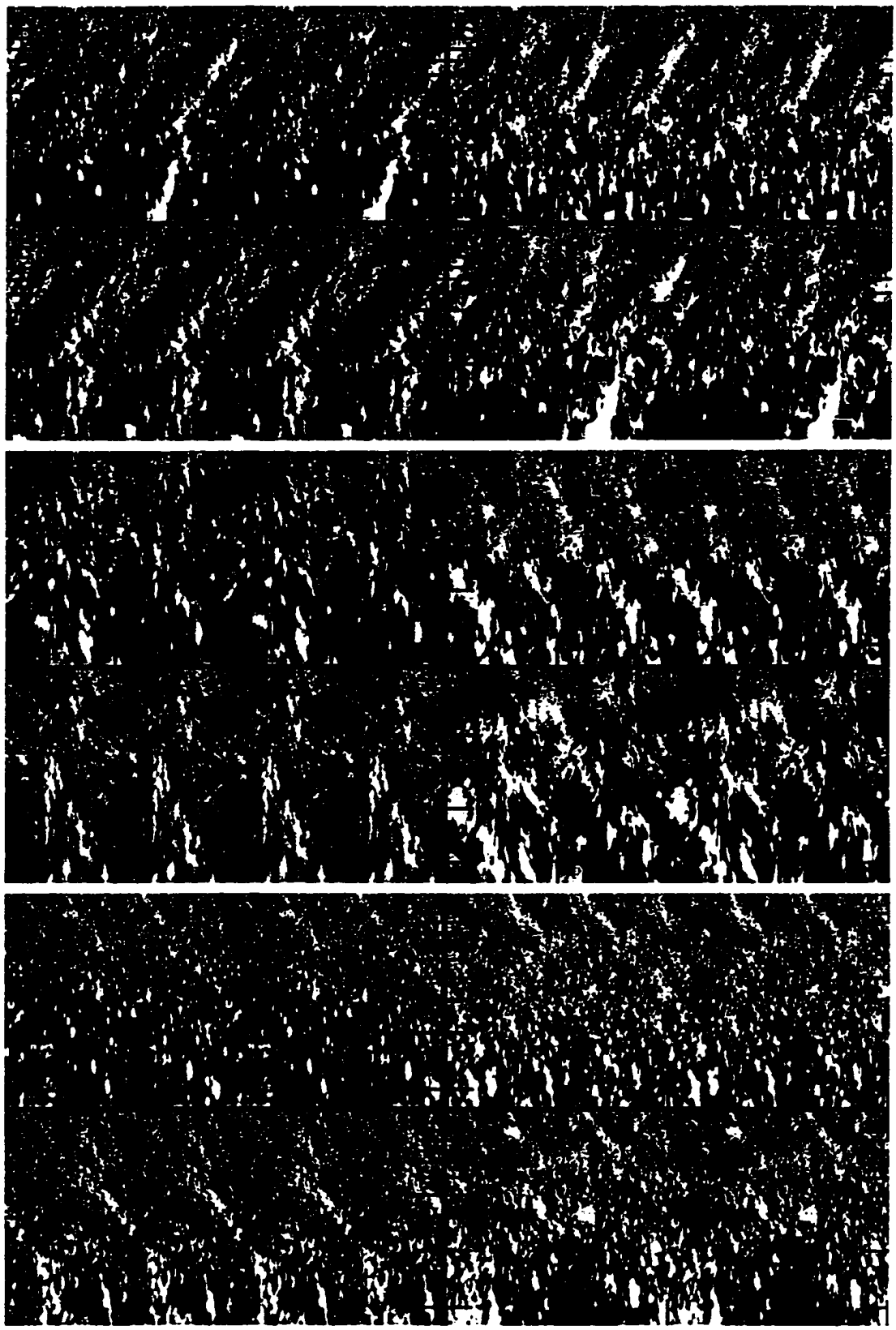

FIG. 2.—(*p*) NGC 6946 (*top*), (*q*) NGC 7793 (*middle*), (*r*) IC 342 (*bottom*)

FIG. 3.—NGC 3938 images with 4 (*left*), 5, and 6 fold symmetry, and circles indicating the 4:1, 5:1 and 6:1 resonances, respectively. This multiple-arm galaxy is apparently dominated by structure with ~5 semiregular arms.

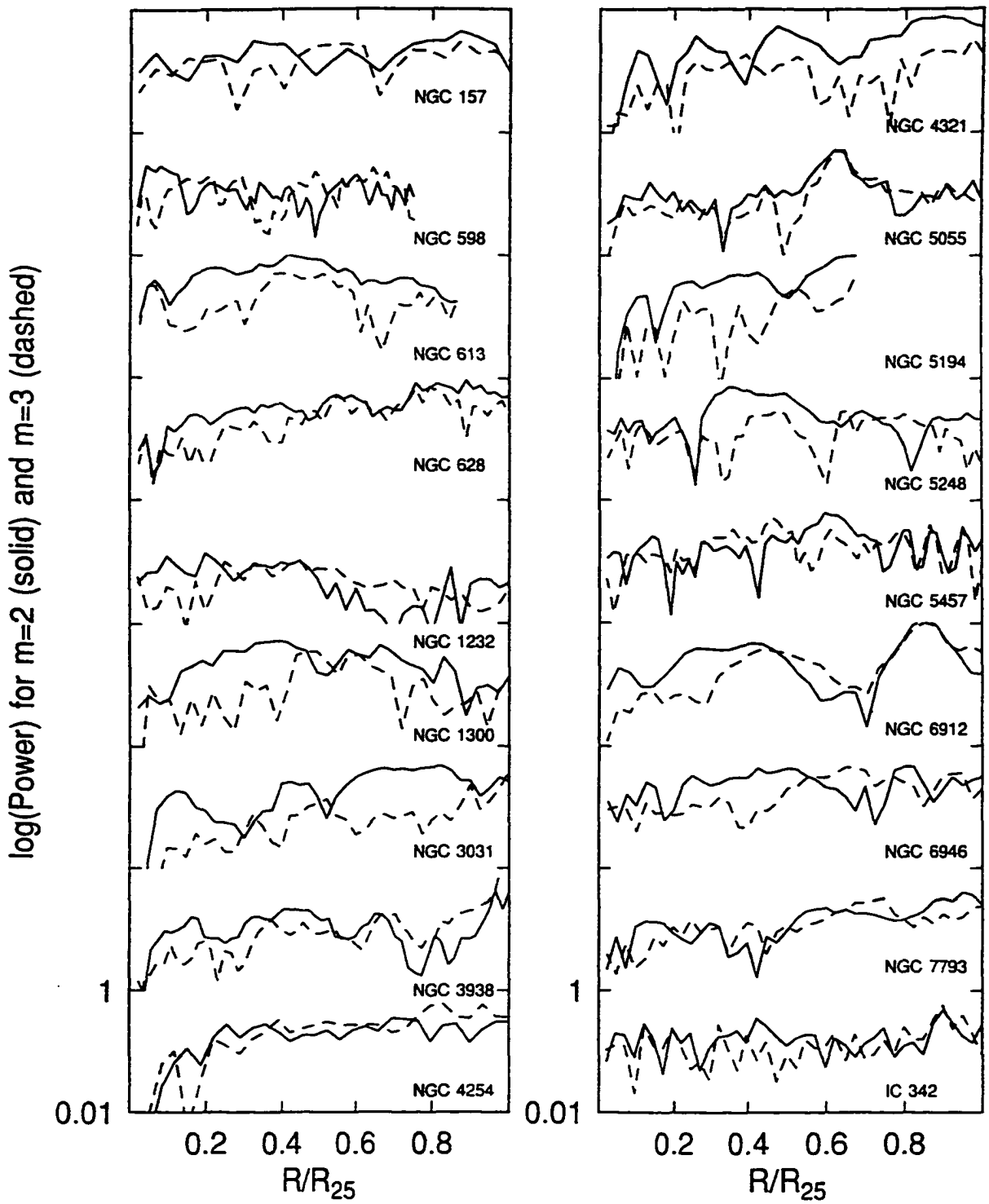

# Chapter 5

# Conclusions and Topics of Further Research

We have analyzed the response of fluid disks under the influence of spiral perturbations with varying types of differential rotation profiles using an improved tight-winding approximation. The perturbations have a time independent structure in a rotating frame. The perturbations can have multiple arms, in which case the spirals formed can be relatively open. Terms that have been neglected in the literature have been included in the analysis, these term include multiple arms, radial gradients of the background surface density, wavenumber, and perturbation amplitude, as well as curvature terms in the equations of motion and continuity.

Radial gradients coupled with curvature have been found to modify the stability conditions. In particular it has been found that there are two types of instabilities associated with curvature. When the disk is self-gravitating, gravitational-curvature instabilities are present throughout the disk for all wavelengths. The growth rates associated with this type of instability are proportional to the ratio of the disk mass

to the total mass accelerating the disk and to the inverse of the orbital time. When the disk is not self-gravitating, acoustic-curvature instabilities are present at all radii, wavelengths, and sound speeds. The growth rates for these instabilities are proportional to the ratio of the sound speed to the radius.

When a strictly local analysis is invoked (no radial gradients, no curvature), there is an acoustic instability that is present in differentially rotating disks. This instability is present for either self-gravitating or non-self-gravitating disks and is due to the asymmetry of the perturbation ($m \neq 0$) and the shearing in the disk. This instability has not been discussed in the literature in the same context as in the present work.

The findings in this investigation have applications primarily in weakly self-gravitating and non-self-gravitating disks that display spiral structure. The usual gravitational instability conditions do not apply in these systems and thus cannot explain the presence of such spiral structure. Such systems include gas-rich disks surrounding galactic nuclei, accretion disks around black holes, proto-planetary disks and low surface density dwarf galaxies. The instabilities discovered in this work are significant in the inner parts of self-gravitating disk with short rotation periods and in non-self-gravitating disk with sound speeds comparable to the rotation speeds.

The central region in the interacting disk galaxy NGC2207 displays multiple dust spirals. Radiative transfer calculations have determined that the gas is not-strongly self-gravitating, nor is there a central bar to drive the spirals. The dust spirals observed may be driven by the acoustic instabilities discussed above.

The importance of deriving a dispersion relation that includes the effect of several spiral arms was recognized when it was discovered that several disk galaxies contain multiple symmetric spirals. The most common structure is three faint

symmetric arms in superposition with the stronger two-armed spirals. It was found that the two-armed structures were self-sustaining wave modes existing between the outer Lindblad resonance and an inner turning region. The three-armed spiral were not independent modes, but driven by the two-armed structures and extending to their resonance radii.

Other studies have included effects from finite thickness in the disk, forces arising from magnetic fields, and systems consisting of two fluids interacting gravitationally. A topic of research that is a logical outgrowth of the present work is to model more realistic conditions in which these other effects are included as well as the effects studied in this investigation when appropriate. The response of gas to density waves can be highly non-linear, and theories exist that take into account the nonlinearities of gas dynamics for local approximations. No analytical theory exists as of yet that encompasses the global instabilities present in non-linear gas dynamics, and such a theory would be crucial towards understanding the response of fluid disks to spiral structures.

# Appendices

## A. Derivation of the second-order differential equation

The equation defined in the introduction of Chapter 2 (Eq. 2.2)

$$\mathcal{L}(\phi_1 + h_1) = -Ch_1 \tag{A1}$$

is derived here from first principles. If the medium is isentropic, the pressure $p$ is a function of the density and is related to the enthalpy $h$ through the equation

$$h = \int \frac{dp}{\rho}, \tag{A2}$$

where $\rho$ is the mass volume density. The force per unit mass from pressure gradients is

$$-\frac{1}{\rho}\nabla p = -\nabla h. \tag{A3}$$

The gravitational potential arising from the halo and disk mass distributions is $\phi$. The gravitational force per unit mass is $-\nabla\phi$.

The total mass density satisfies the mass continuity equation

$$\frac{\partial \rho}{\partial t} + \nabla \cdot (\rho \mathbf{u}) = 0 \tag{A4}$$

and the equation of motion is

$$\frac{\partial \mathbf{u}}{\partial t} + (\mathbf{u} \cdot \nabla)\,\mathbf{u} = -\nabla(\phi + h), \tag{A5}$$

where $\mathbf{u}$ is the velocity vector. The enthalpy can be further related to the density by the definition of the acoustic speed $a$ as

$$a^2 = \frac{dp}{d\rho} = \rho\frac{dh}{d\rho}. \tag{A6}$$

Equation (A4) can then be written in the form

$$\frac{1}{a^2}\frac{Dh}{Dt} + \nabla \cdot \mathbf{u} = 0, \tag{A7}$$

where $D/Dt = \partial/\partial t + \mathbf{u} \cdot \nabla$ is the substantive derivative. The speed $a$ can be identified with the sound speed of the fluid disk or the random velocity of the interstellar cloud, and is analogous to the root mean square value of the velocity dispersion of the stars if the system is a stellar disk.

Since the stable configuration of the disk is axisymmetric, it is natural to consider a cylindrical coordinate system ($r$, $\theta$, $z$) centered on the center of symmetry of the disk and with the $z$-axis aligned with the axis of symmetry of the disk. For an infinitely thin disk one can then speak of the total surface mass density $\sigma(r, \theta, t)$. The gravitational potential $\phi$ that produces accelerations on the mass density cannot be related to $\sigma$ via Poisson's equation because it also depends on the three-dimensional halo mass distribution. Consider perturbations that are much smaller than the equilibrium properties of the disk:

$$\begin{aligned} \sigma_1(r, \theta, t) &\ll \sigma_0(r) \\ \phi_1(r, \theta, z, t) &\ll \phi_0(r, z) \\ |\mathbf{u}_1(r, \theta, t)| &\ll |\mathbf{u}_0(r)| \end{aligned}$$

The zero-order equation of motion is

$$(\mathbf{u}_0 \cdot \nabla)\, \mathbf{u}_0 = -\nabla (\phi_0 + h_0)\,. \tag{A8}$$

In component form, the $\theta$ component is identically 0; the $r$ component is

$$-r\Omega^2(r) = -\frac{d}{dr}(\phi_0 + h_0)\,, \tag{A9}$$

where $\Omega(r) = \mathbf{u}_{0\theta}/r$ is the angular speed of the disk. The first order equation of motion is

$$\frac{\partial \mathbf{u}_1}{\partial t} + (\mathbf{u}_0 \cdot \nabla)\, \mathbf{u}_1 + (\mathbf{u}_1 \cdot \nabla)\, \mathbf{u}_0 = \nabla(\phi_1 + h_1), \tag{A10}$$

which in component form is

$$\begin{aligned} \frac{\partial u_1}{\partial t} + \Omega\frac{\partial u_1}{\partial \theta} - 2\Omega v_1 &= -\frac{\partial}{\partial r}(\phi_1 + h_1) \\ \frac{\partial v_1}{\partial t} + \Omega\frac{\partial v_1}{\partial \theta} + \left(2\Omega + r\frac{d\Omega}{dr}\right)u_1 &= -\frac{1}{r}\frac{\partial}{\partial \theta}(\phi_1 + h_1), \end{aligned} \tag{A11}$$

where the components of the perturbation velocity in the $r$ and $\theta$ direction are $[u_1(r,\theta,t),\, v_1(r,\theta,t)]$.

The equation of continuity, (Eq. A4), is identically 0 to zero-order. The first order equation is

$$\frac{\partial \sigma_1}{\partial t} + \nabla \cdot (\sigma_0 \mathbf{u_1} + \sigma_1 \mathbf{u_0}) = 0, \tag{A12}$$

or

$$\frac{\partial \sigma_1}{\partial t} + \frac{1}{r}\frac{\partial}{\partial r}(r\sigma_0 u_1) + \frac{1}{r}\frac{\partial}{\partial \theta}(\sigma_0 v_1 + \sigma_1 r\Omega) = 0. \tag{A13}$$

The first order density is related to the first order enthalpy by the relation

$$h_1 = \frac{a^2}{\sigma_0}\sigma_1. \tag{A14}$$

Equations (A11), (A13), and (A14) along with Poisson's equation

$$\nabla^2 \phi_1 = 4\pi G \sigma_1 \delta(z), \tag{A15}$$

where $G$ is the constant of universal gravitation, describe the behavior of the perturbations.

Equations (A11) and (A13) have coefficients that are independent of $\theta$ and $t$, so without loss of generality and anticipating spiral perturbations, the perturbation quantities are assumed to have the form $g_1(r,\theta,t) = g_1(r)e^{i(\omega t - m\theta)}$; $\omega$ is the frequency of oscillation if it is real, and the growth or decay rate if it is imaginary, $m$ is the number of arms. Substituting into Eq. (A11), the first order velocity components

are

$$u_1 = -\frac{i}{D}\left[(\omega - m\Omega)\frac{d}{dr} + \frac{2m\Omega}{r}\right](\phi_1 + h_1)$$
$$v_1 = \frac{1}{D}\left[\left(2\Omega + r\frac{d\Omega}{dr}\right)\frac{d}{dr} + \frac{m}{r}(\omega - m\Omega)\right](\phi_1 + h_1), \qquad \text{(A16)}$$

where $D = \kappa^2 - (\omega - m\Omega)^2$. The term $\kappa$ is called the epicyclic frequency and is defined by the relation

$$\kappa^2 = (2\Omega)^2\left(1 + \frac{1}{2}\frac{d\ln\Omega}{d\ln r}\right); \qquad \text{(A17)}$$

it is the frequency with which a fluid particle would oscillate in the radial direction if it were disturbed about an equilibrium position.

Finally substituting equations (A14) and (A16) and the functional form of the perturbation quantities into the equation of continuity (A13), we obtain (Goldreich & Tremaine 1979, Lin & Lau 1979)

$$\left(\frac{d^2}{dr^2} + A\frac{d}{dr} + B\right)(\phi_1 + h_1) = \frac{Dh_1}{a^2}, \qquad \text{(A18)}$$

where

$$A = \frac{d}{dr}\left(\frac{\sigma_0 r}{D}\right)$$
$$B = -\frac{m^2}{r^2} + \frac{2m\Omega}{\kappa r\nu}\frac{d}{dr}\left(\frac{D}{\sigma_0\Omega}\right),$$

which is equation (2.2).

## B. Derivation of Angular Momentum Flux Conservation to Higher Orders

Goldreich and Tremaine (1978) show that if there is no dissipation in the disk, angular momentum flux is conserved except at the resonances in the usual tightwinding approximation ($1/|kr| \ll 1$) for radial wavenumber $k$ and radius r. We show here that if the modified approximation is used ($1/\hat{k}r \ll 1$, $\hat{k} = \sqrt{k^2 + m^2/r^2}$), there are requirements on the properties of the spiral perturbation that allow conservation of angular momentum flux.

A disk can only transfer angular momentum to the outer regions if it supports non-axisymmetric mass distributions. The gravitational potential that affects the axisymmetric mass distribution arises from the halo mass and the disk mass. If there are spiral density perturbations in the disk, then these mass distributions will create gravitational torques that change the angular momentum of the disk. The gravitational potential of the disk is composed of an axisymmetric component,$\phi_0(r)$, and a time-dependent, asymmetric component, $\phi_1(r, \phi, z, t)$. The acceleration due to gravity is $\mathbf{g} = \mathbf{g_0} + \mathbf{g_1} = \nabla(\phi_0 + \phi_1)$.

The gravitational stress tensor is (Lynden-Bell & Kalnajs 1972)

$$\mathbf{T} = \frac{\mathbf{gg}}{4\pi\mathbf{G}} - \frac{g^2}{8\pi G}\mathbf{I}, \tag{B1}$$

where $\mathbf{I}$ is the unit tensor with components $\delta_{ij}$. Angular momentum is transported in the disk by gravitational stresses. The angular momentum flux transported from the inner part of the disk to the outer part by gravitational stresses from the wave is given by

$$\mathbf{F}_G = \int \mathbf{rxT} \cdot d\mathbf{S}, \tag{B2}$$

where the integration extends over a cylindrical region of radius $r$ and area $d\mathbf{S}$

extends along the outer normal to the cylinder. Only the first order gravitational acceleration contributes to $F_G$ in the $z$ direction,

$$F_{Gz} = \frac{r}{4\pi G} \int d\theta \int dz \Re\left(\frac{\partial \phi_1}{\partial \theta}\right) \Re\left(\frac{\partial \phi_1}{\partial r}\right), \tag{B3}$$

where $\Re()$ and $\Im()$ are the real and imaginary parts of the complex expression inside the parenthesis. We use complex expressions for the perturbation quantities in the analysis with the understanding that only the real values are taken for interpretation.

Following the terminology from Appendix A, we find that the stress tensor is (Lynden-Bell & Kalnajs 1972)

$$\mathbf{S} = \sigma \mathbf{u}\,\mathbf{u} \delta(z) + \mathbf{I} p, \tag{B4}$$

where $\sigma$ is the total surface density (disk and spiral), the first term is due to the motions in the disk and the second term is from the vertically-integrated pressure, $p$. The pressure is isotropic in the plane of the disk. The velocity can be separated into pure rotation, $\mathbf{u_0}(r)$, and motions due to a spiral perturbation, $\mathbf{u_1}(r, \theta, r) = (u_1, v_1)$, where $|\mathbf{u_1}| \ll |\mathbf{u_0}|$. Advective motions from the perturbation also create angular momentum flux. The flux transferred by advective motions of the perturbation density from the regions inside a cylinder $r$ is

$$F_{Az} = r^2 \sigma_0 \int \Re(u_1)\, \Re(v_1)\, d\theta, \tag{B5}$$

where $\sigma_0(r)$ is the axisymmetric disk surface mass density.

The asymptotic expression for the perturbation gravitational potential is (Goldreich & Tremaine 1978)

$$\phi_1 = \Phi(r) e^{-|k(r)z|} e^{i\left(\int k dr + \omega t - m\theta\right)}, \tag{B6}$$

$\Phi$ is a slowly varying amplitude, $\omega$ is the wave frequency, and $m$ is the number of

spiral arms. It is convenient to define an enthalpy function

$$h_1 = \frac{dp}{\sigma}. \tag{B7}$$

The enthalpy is related to the potential through Poisson's equation. Bertin & Mark (1979) consider tightly wound waves and obtain a linear relation between the enthalpy and the potential of the spiral perturbation, (Eq. 2.5 and discussion thereafter):

$$h_1 = -f(r)\phi_1, \tag{B8}$$

where

$$f(r) = \frac{\hat{k}}{k_J}\left[1 + i\frac{f_1}{\hat{k}r} + \frac{f_2}{(\hat{k}r)^2} + \frac{f_3 + if_4}{(\hat{k}r)^3} + ...\right], \tag{B9}$$

$k_J = 2\pi G\sigma_0/a^2$, and $a^2 \equiv dp_0/d\sigma_0$ for pressure $p_0$ for axisymmetric disk. The expansion is in the small parameter $1/\hat{k}r$; $\hat{k} = \sqrt{k^2 + m^2/r^2}$ is the combined wavenumber. The terms $f_i$ involve radial derivatives of $k$ and $\Phi$ and are pure real, for example,

$$f_1(r) = sgn(k)\frac{|k|}{\hat{k}}\left[-\frac{r\Phi'}{\Phi} - \frac{1}{2} - \frac{m^2}{2\hat{k}^2r^2}\left(1 + \frac{rk'}{k}\right)\right], \tag{B10}$$

where $'$ denotes radial derivative; $f_4$ involves higher derivatives of $k$ and $\Phi$.

The perturbation velocity components are obtained from $(\phi_1 + h_1)$ from the Appendix A (Eq. A16). Define the sum $(\phi_1 + h_1) \equiv Z$. The equation of continuity (Eqs. 2, A1) now becomes

$$Z'' + A(r)Z' + B(r)Z = Dh_1/a^2, \tag{B11}$$

where $D = \kappa^2(1 - \nu^2)$ and $A(r)$ and $B(r)$ are defined in chapter 2. They are

$$\begin{aligned} A &= \frac{d}{dr}\left[\ln\left(\frac{\sigma_0 r}{D}\right)\right] \\ B &= -\frac{m^2}{r^2} + \left(\frac{2m\Omega}{\kappa\nu r}\right)\frac{d}{dr}\left[\ln\left(\frac{D}{\sigma_0\Omega}\right)\right]. \end{aligned}$$

Assume for now that the wave frequency is pure real. Substituting the functional form of $\phi_1$ into the flux equations we find that gravitational torques produce angular momentum flux

$$F_G = sgn(k)\frac{mr\Phi(r)^2}{4G}. \tag{B12}$$

Advective motions produce flux

$$F_A = \frac{\pi m r \sigma_0}{D}\left[\Im(Z)\Re(Z') - \Re(Z)\Im(Z')\right]. \tag{B13}$$

We can simplify the expression for advective transport by recognizing that the expression inside the brackets is just $\Im(ZZ^{*'})$, where $z^*$ is the complex conjugate of the complex expression $z$. Also recall that $z'^* = z^{*'}$. The total flux is then

$$F(r) = F_G + F_A = \frac{m}{4G}\left[sgn(k)(r\Phi^2) + \frac{4\pi G r\sigma_0}{D}\Im(ZZ^{*'})\right]. \tag{B14}$$

The derivative of the flux is

$$F'(r) = \frac{m}{4G}\left(sgn(k)(r\Phi^2)' + 4\pi G\left[\left(\frac{r\sigma_0}{D}\right)'\Im\left(ZZ^{*'}\right) + \frac{r\sigma_0}{D}\Im\left(ZZ^{*''}\right)\right]\right). \tag{B15}$$

The last term is simplified since $\Im(zz^{*'})' = \Im(z'z^{*'} + zz^{*''}) = \Im(zz^{*''})$.

We can express the continuity equation as

$$Z'' + \left(\frac{D}{r\sigma_0}\right)\left(\frac{r\sigma_0}{D}\right)'Z' + B(r)Z = \frac{D}{a^2}h_1(r). \tag{B16}$$

Taking the complex conjugate of this expression, multiplying by $Z$ and taking the imaginary part of the resulting expression gives:

$$\Im(ZZ^{*''}) = -\left(\frac{D}{r\sigma_0}\right)\left(\frac{r\sigma_0}{D}\right)'\Im(ZZ^{*'}) + \frac{D}{a^2}\Im(Zh_1{}^*). \tag{B17}$$

The term $\Im(Zh_1{}^*) = \Im(\phi_1 h_1{}^* + h_1 h_1{}^*) = \Phi^2\Im(f)$, since $\Im(z^*) = -\Im(z)$. Substituting this expression into the derivative of the flux gives

$$F'(r) = \frac{m}{4G}\left[sgn(k)(r\Phi^2)' + 2k_J r\Phi^2\Im(f)\right], \tag{B18}$$

or

$$F'(r) = \frac{m}{4G}\left[sgn(k)(r\Phi^2)' + 2\Phi^2\left(f_1 + \frac{f_4}{\hat{k}^2r^2}\right)\right]. \tag{B19}$$

If we substitute the expression for $f_1$ in Eq. (B19) and drop the $f_4$ term (ignore $1/(\hat{k}^2r^2)$ terms), we get:

$$F'(r) = sgn(k)\frac{m}{4G}\left[\left(1 - \frac{|k|}{\hat{k}}\right)(r\Phi^2)' - \frac{|k|}{\hat{k}}\frac{m^2}{(\hat{k}r)^2}\left(1 + \frac{rk'}{k}\right)\Phi^2\right]. \tag{B20}$$

The pitch angle of the spiral is $P = \tan^{-1}(m/|kr|)$; in terms of $P$, Eq. (B20) is

$$F'(r) = sgn(k)\frac{m}{4G}\left[(1 - |\cos P|)\left(r\Phi^2\right)' - |\cos P|\sin^2 P\left(1 + \frac{rk'}{k}\right)\Phi^2\right], \tag{B21}$$

or

$$F'(r) = sgn(k)\frac{m}{4G}\left[r\Phi^2(1 - |\cos P|)\right]'. \tag{B22}$$

We see that for $m = 1, 2$, $|\cos P| \simeq 1$ for large $|kr|$, and angular momentum flux is conserved to lowest order. For angular momentum flux to be conserved for larger pitch angles, the amplitude $\Phi$ has to satisfy the condition

$$\Phi \propto \frac{1}{\sqrt{r(1 - |\cos P|)}}. \tag{B23}$$

This condition determines the amplitude variation along the spiral. For small pitch angle we can express $1 - |\cos P| = m^2/(2k^2r^2) + ...$, so equation (B22) becomes

$$F'(r) = sgn(k)\frac{m^3}{8G}\left[\frac{r\Phi^2}{k^2r^2}\right]', \tag{B24}$$

and for constant flux the amplitude variation becomes

$$\Phi \propto \sqrt{r}|k|. \tag{B25}$$

In the absence of gravity there are no gravitational torques, $F_G = 0$, but there is angular momentum flux from advective motions. We can obtain an expression for radial derivative of flux in terms of an enthalpy amplitude $H(r)$

$$F_A = -\pi m r \sigma_0 k H^2/D. \tag{B26}$$

To lowest order the dispersion relation in the absence of self-gravity is $\nu^2 = 1 + (a^2\hat{k}^2)/\kappa^2$ and $D = -a^2\hat{k}^2$. For $F_A$ to be constant the enthalpy amplitude has to satisfy the condition

$$H^2 \propto \frac{a^2}{r^2\sigma_0 \sin P \cos P} \tag{B27}$$

We have found that for multiple arm, relatively open spirals, angular momentum flux is conserved if the spiral amplitude and the wavenumber are related to each other. In the tightwinding limit ($1/|kr| \ll 1$) for few arms ($m \approx 1$ to 2), flux is conserved automatically. Further investigation is needed to understand how angular momentum is transferred by the spiral at the resonances in this modified tightwinding approximation.

# References

## REFERENCES

Angilello, J., Chiang, W.H., Elmegreen, D.M., and Segmuller, A. 1984, in Proc. Conf. Goddard Astronomical Microdensitometry, ed. D.A. Klinglesmith (NASA CP- No. 2317), p. 229.

Artymowicz, P., and Lubow, S.H. 1992, ApJ, 389, 129.

Athanassoula, E. 1978a, in: Structure and Properties of Nearby Galaxies, eds. Berkhuijsen, E. M. & Wielebinski, R. (Reidel Pub.), 163

Athanassoula, E. 1978b, AA 69, 395

Athanassoula, E. 1980, AA, 88, 184

Athanassoula, E. 1984, Physics Reports, 114, Nos. 5 & 6, 319

Athanassoula, E., Bosma, A., and Papaioannou, S. 1987, AA ,179, 23.

Balbus, S.A., & Hawley, J.F. 1991, ApJ, 376, 214

Bertin, G. 1991, in Dynamics of Galaxies and their Molecular Cloud Distributions, eds. F. Combes and F. Casoli, Dordrecht: Kluwer, p. 93.

Bertin, G., Lin, C.C., Lowe, S.A. & Thurstan, R.P. 1989, ApJ, 338, 78

Bertin, G., Lin, C.C., Lowe, S.A. & Thurstan, R.P. 1989, ApJ, 338, 104

Bertin, G. & Mark, J W-K. 1979, SIAM, J. Appl. Math., 36, 407

Bertin, G. & Romeo, A. B., 1988, A. A., 195, 105

Biviano, A., Girardi, M., Giuricin, G., Mardirossian, F., and Mezzetti, M. 1991, Ap.J., 376, 458.

Block, D.L., Elmegreen, B.G. & Wainscoat, R.J. 1996, Nature, 381, 674

Bohlin, R.C., Savage, B.D. & Drake, J.F. 1978, ApJ, 224, 132

Byun, Y.I., Freeman, K.C., & Kylafis, N.D. 1994, ApJ, 432, 114

Caldwell, N., Kennicutt, R., Phillips, A. C. & Schomer, R. A. 1992, ApJ, 370, 526

Carlberg, R.G., & Freedman, W.L. 1985, ApJ 298, 486.

Carollo, C.M., Stiavelli, M., & Mack, J. 1998, AJ, in press

Condon, J.J. 1983, ApJS, 53, 459

Considére, S., and Athanassoula, E. 1988, AA Suppl., 76, 365.

de Vaucouleurs, G. 1963, ApJ Suppl, 8, 31.

de Vaucouleurs, G., de Vaucouleurs, A., and Corwin, H.G., 1976, Second Reference Catalogue of Galaxies, (Austin: Univ. of Texas).

Danver, C.G. 1942, Lund Obs.Ann. Vol. 10.

Devereux, N., Ford, H. & Jacoby, G. 1997, ApJ, 481, L71

Dopita, M.A., Koratkar, A.P., Allen, M.G., Tsvetanov, Z.I., Ford, H.C., Bicknell, G.V., & Sutherland, R.S. 1997, ApJ, 490, 202

Elmegreen, B.G. 1987, in IAU Symposium 115: Star Forming Regions, ed. M. Peimbert and J. Jugaku, (Dordrecht: Reidel), 457

Elmegreen, B.G. 1991, in Dynamics of Galaxies and their Molecular Cloud Distributions, eds. F. Combes and F. Casoli, Dordrecht: Kluwer, p. 113.

Elmegreen, B.G. 1994, ApJ, 433, 39

Elmegreen, B.G., and Elmegreen, D.M. 1985, ApJ 288, 438.

Elmegreen, B.G., and Elmegreen, D.M. 1986, ApJ 311, 554.

Elmegreen, B.G., and Elmegreen, D.M. 1990a, ApJ 355, 52.

Elmegreen, B.G., and Elmegreen, D.M. 1990b, ApJ 364, 412.

Elmegreen, B.G., Elmegreen, D.M., and Seiden, P.E. 1989, ApJ, 343, 602.

Elmegreen, B.G., Elmegreen, D.M., Brinks, E., Yuan, C., Kaufman, M., Klarić, M., Montenegro, L., Struck, C. & Thomasson, M. 1998, ApJL, in press

Elmegreen, B.G., Elmegreen, D.M. & Montenegro, L. 1992, ApJS, 79, 37

Elmegreen, B.G., Sundin, M., Kaufman, M., Brinks, E. & Elmegreen, D.M. 1995b, ApJ, 453, 139

Elmegreen, B.G., and Thomasson, M. 1993, A A, 272, 37.

Elmegreen, D.M. 1981, ApJS, 47, 229.

Elmegreen, D.M., 1985, in IAU Symposium No. 106: The Milky Way, ed. H. van Woerden, Dordrecht: Reidel, p. 255.

Elmegreen, D.M. & Elmegreen, B.G. 1984, ApJS, 54, 127

Elmegreen, D.M., and Elmegreen, B.G. 1989, ApJ, 314, 3.

Elmegreen, D.M., Kaufman, M., Brinks, E., Elmegreen, B.G. & Sundin, M. 1995a ApJ, 453, 100

Engelbracht, C.W., Rieke, M.J., Rieke, G.H., & Latter, W.B. 1996, ApJ, 467, 227

Ford, H.C., et al. 1994, ApJ, 435, L27

Fridman, A.M., Morozov, A.G., Nezlin, M.V., Pasha, I.I., Polyachenko, V.L., Rylov, A.Yu., Snezhkin, E.N., Torgashin, Yu.N., Trubnikov, A.S. 1987, in Observational Evidence of Activity in Galaxies, eds. E.Ye. Khachikian, K.J. Fricke, and J. Melnick, (Dordrecht: Reidel), p. 147.

Goldreich, P. & Lynden-Bell, D. 1965, MNRAS, 130, 125

Goldreich, P. & Tremaine, S. 1979,ApJ, 233, 857.

Hernquist, L. 1990, in Dynamics and Interactions in Galaxies, ed. R. Wielen, (Berlin: Springer), p. 108.

Howard, S., and Byrd, G.G. 1990, AJ, 99, 1798.

Hubble, E. 1926, ApJ, 64, 321.

Hunter, C. 1983, in Lectures in Applied Mathematics, 20, p. 179

Hunter, D. A., Elmegreen, B. G. & Baker, A. L. 1998, ApJ, 493, 595

Iye, M., Okamura, S., Hamabe, M., and Watanabe, M. 1982, ApJ, 256, 103.

Julian, W. H., Toomre, A. 1966, ApJ, 146, 810

Kennicutt, R.C., Jr. 1981, AJ, 86, 1847.

Knapen, J.H., Beckman, J.E., Heller, C.H., Shlosman, I., & de Jong, R.S. 1995, ApJ, 454, 623

Krakow, W., Huntley, J.M., and Seiden, P.E. 1982, AJ, 87, 203.

Kuijken, K. & Gilmore, G. 1989, MNRAS, 239, 605

Kuijken, K. & Gilmore, G. 1991, ApJ367, L9

Larson, R. B. 1990, MNRAS, 243, 588

Lau, Y. Y. & Bertin, G. 1978, ApJ, 226, 508

Lauer, T.R., et al. 1992, AJ, 103, 703

Lin, C. C. 1966, *SIAM J Appl. Math.*, 14, 876

Lin, C.C. & Lau, Y. Y 1979, Studies in Appl. Math., 60, 97.

Lin, C.C., and Lowe, S.A. 1990, in Galactic Models, Annals of the New York Academy of Sciences, eds. J.R. Buchler, S.T. Gottesman, and J.H. Hunter, Jr., Vol. 596, p. 80.

Lin, C.C. & Shu, F. H 1964, ApJ, 140, 646

Lin, C.C. & Shu, F. H 1966, Proc. Nat. Acad. Sci., 55, 229

Lin, C.C., & Shu, F.H. 1967, in IAU Symposium No. 31, Radio Astronomy and the Galactic System, ed. H. van Woerden (New York: Academic Press), p. 313.

Lin, C.C. & Shu, F. H. 1971, in: Astrophysics and General Relativity, Vol. 2, eds. Chretien, M., Derer, S., and Goldstein, J. (Gordon and Breach Science Pub.) 239.

Lin, C. C., Yuan, C. & Shu, F. H. 1969, ApJ, 155, 721

Lindblad, B. 1958. Stock. Obs. Ann., 20, No. 6

Lynden-Bell, D. & Kalnajs, A. J. 1972, MNRAS, 157,1

Mark, J. W-K. 1971, Proc. Natl. Acad. Sc. USA, 68, 2095

Mark, J. W-K. 1974, in: The Formation and Dynamics of Galaxies, ed. Shakeshaft, J. (Reidel Pub.), 417

Mark, J. W-K. 1974, ApJ, 193, 539

Mark, J. W-K. 1976, ApJ, 203, 81

Mark, J. W-K. 1976, ApJ, 205, 363

Mark, J. W-K. 1976, ApJ, 206, 418

Mark, J. W-K. 1977, ApJ, 212, 645

Montenegro, L. 1998, PhD Dissertation, City University of New York

Montenegro, L., Yuan, C., & Elmegreen, B.G. 1998, submitted to ApJ.

Nakai, N., Inoue, M. & Miyoshi, M. 1993, Nature, 361, 45

Phillips, A.C., Illingworth, G.D., MacKenty, J.W. & Franx, M., 1996, AJ, 111, 1566

Patsis, P.A., Contopoulos, G., and Grosbol, P. 1991, AA, 243, 373.

Persic, M., and Salucci, P. 1991, ApJ, 368, L60.

Prendergast, K. H. 1983, in: Internal Kinematics and Dynamics of Galaxies, ed. Athanassoula, E. (Reidel Pub.), 215

Roberts, W.W. 1969, ApJ, 158, 123

Roberts, W.W., Shu, F. 1972, ApJ, 12, 49

Rubin, V.C., Burstein, D., Ford, W.K. & Thonnard, A. 1985, ApJ, 289, 81

Rubin, V.C. & Ford, W.K., Jr. 1983, ApJ, 271, 556

Sakamoto, K., Okumura, S., Minezaki, T., Kobayashi, Y., & Wada, K. 1995, AJ, 110, 2075

Sandage, A. 1961, The Hubble Atlas of Galaxies, Carnegie Institute of Washington, Washington D.C.

Sandage, A., and Bedke, J. 1988, Atlas of Galaxies, (Washington D.C., US GPO).

Sandage, A., and Tammann, G.A., 1981, A Revised Shapley Ames Catalog of Bright Galaxies, Carnegie Institute of Washington.

Schmidt, M. 1985, in IAU Symposium 106, The Milky Way Galaxy, ed. H. van Woerden, Dordrecht: Reidel, 203

Schweizer, F. 1980, ApJS, 31, 313

Sellwood, J.A. & Lin, D.N.C. 1989, MNRAS, 240, 991

Sellwood, J.A. & Kahn, F.D. 1991, MNRAS, 250, 278

Shu, F.N., Milione, V., and Roberts, W.W. 1973, ApJ, 183, 819.

Strom, S.E., Jensen, E.B., and Strom, K.M. 1976, ApJ, 206, L11.

Strong, A.W. et al. 1988, A&A, 207 1

Struck, C. 1997, ApJS, 113, 269

Tagger, M., Sygnet, J.F., Athanassoula, E., and Pellat, R. 1987, ApJ, 318, L43.

Thomasson, M., Elmegreen, B.G., Donner, K.J., and Sundelius, B. 1990, ApJ, 356, L9.

Thornley, M.D., & Mundy, L.G. 1997, ApJ, 490, 682

Toomre, A. 1964, ApJ, 139, 1217

Toomre, A. 1969, ApJ, 158, 899

Toomre, A. & Toomre J. 1972, ApJ, 178, 623

Toomre, A. 1981, in The Structure and Evolution of Normal Galaxies, ed. S.M. Fall and D. Lynden-Bell, (Cambridge: Cambridge Univ. Press), p. 111.

Tully, R.B. 1974, ApJ Suppl., 27, 449.

van den Bergh, S. 1960, ApJ, 131, 215.

van der Hulst, J. M., Skillman, E. D., Smith, P. R., Bothun, G. D., Mc Gaugh, S. S. & de Block, W. J. G. 1993, AJ, 106, 548

Vandervoort, P. O. 1970, ApJ, 161, 67

Vila, M.B., Pedlar, A., Davies, R.D., Hummel, E. & Axon, D.J. 1990, MNRAS, 242, 379

Visser, H.C.D. 1980, AA, 88. 149.

Wevers, B.M.H.R. 1984, PhD Dissertation, Groningen.

Yuan, C. 1984, ApJ, 281, 600

Yuan, C. & Cheng, Y. 1991, ApJ, 376, 104

Yuan, C. & Kuo, C-L. 1997, ApJ, 484, 750

Zang, T.A., 1976, Ph.D. thesis, M.I.T.

---

This manuscript was prepared with the AAS LaTeX macros v4.0.

# IMAGE EVALUATION
# TEST TARGET (QA-3)

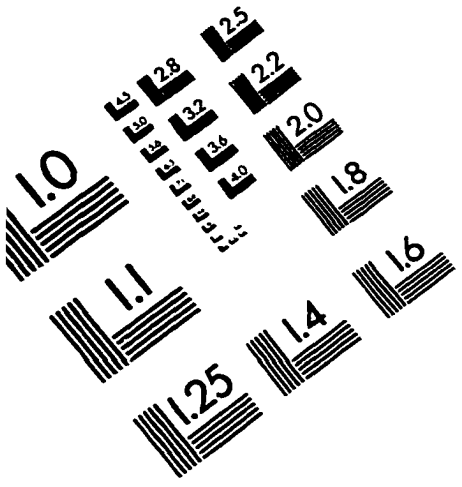


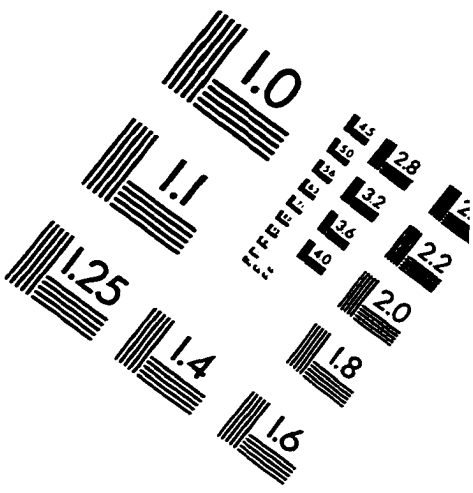


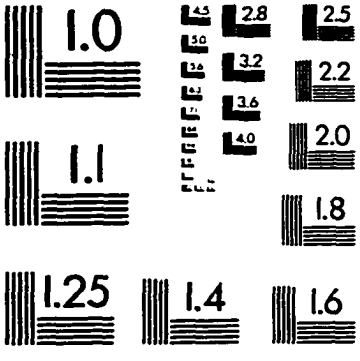


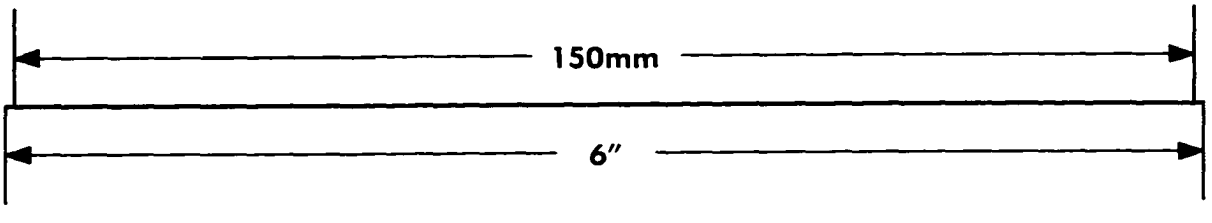


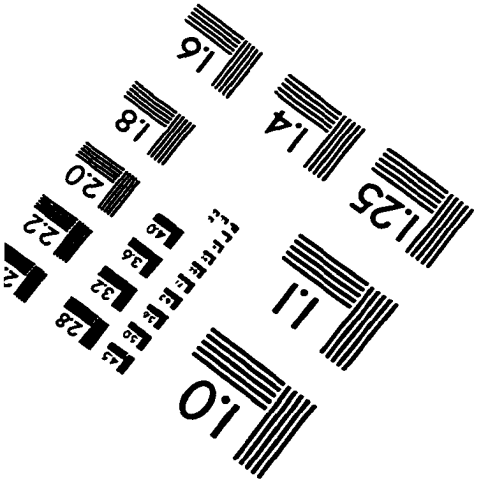


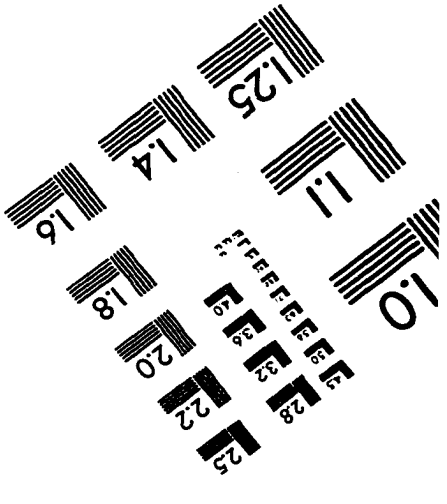


APPLIED IMAGE, Inc
1653 East Main Street
Rochester, NY 14609 USA
Phone: 716/482-0300
Fax: 716/288-5989